



**3D Seismic Survey Design: Coil Shooting, Multi-Component (3C) Receivers with Gulf  
of Mexico and Caribbean Case Histories**

---

A Dissertation Presented to  
the Faculty of the Department of Earth and Atmospheric Sciences  
University of Houston

---

In Partial Fulfillment  
of the Requirements for the Degree  
Doctor of Philosophy

---

By  
Eray Kocel  
May 2015

**3D Seismic Survey Design: Coil Shooting, Multi-Component (3C) Receivers with Gulf  
of Mexico and Caribbean Case Histories**

---

Eray Kocel

APPROVED:

---

Dr. Robert R. Stewart, Chairman

---

Dr. Paul Mann

---

Dr. William Sager

---

Dr. Edip Baysal

---

Dean, College of Natural Sciences and Mathematics

## Acknowledgements

There is a long list of individuals and organizations whose support made this dissertation possible. First and foremost, I am grateful to my advisor Dr. Robert R. Stewart for providing me with the opportunity to be a part of the Allied Geophysical Laboratories (AGL). Apart from his expertise in geoscience, I gained a great deal of invaluable life experience from him. I thank Dr. Mann, and Dr. Baysal, for their knowledge and insight throughout this long, enduring process. Thanks to the faculty at the Department of Earth and Atmospheric Sciences for their admirable teaching expertise. I also would like to thank the Allied Geophysical Laboratories and Department of Earth and Atmospheric Sciences at University of Houston for the financial support.

I thank my colleagues and friends from both the department and the AGL (especially Li Chang, Joan Blanco, Anoop William, Long Huang, Jiannan Wang, Yue Du, Soumya Roy, and Naila Dowla) for their assistance in both acquiring and analyzing the data. Their friendly atmosphere at the office made things easier. I would like to thank Nick Moldoveanu, Francois Daube, and Eugene Gridnev for their support throughout my internship and providing me the permission to use some of the data presented in this dissertation. I would also like to extend my gratitude to Schlumberger (especially Nerissa Goodman) for technical and software support for Omega, Petrel, Omni, and Vista software. We acknowledge WesternGeco for the permission to present some of the results on chapter



2. We also would like to express our gratitude to the Comesa and Pemex for their useful discussions related with the multicomponent survey design on Chapter 3.

We thank SEG's Geoscientists Without Borders program for supporting the Haiti project and Global Geophysical in Houston for kindly donating their land node recording system used in Haiti studies during 2013. We thank the Haiti Bureau of Mines and its employees (Nicole Dieudonne, Sophia Ulysse) and Mr. Alexander von Lignau for helping to coordinate the Léogâne surveys in 2012 and 2013. Special thanks to Dr. Nikolay Dyaur (UH) who greatly helped with the laboratory measurements and Mr. Anoop William (UH) for equipment logistics and data management. The radar image in Chapter 4 was kindly provided by Eric Fielding. We thank Eric Calais and Roby Douilly for providing the earthquake aftershock data presented in Chapter 4.

I also want to express my appreciation for Monica Garib, who stood by my side and helped me during the long months of researching. She motivated me constantly and happily read and edited my dissertation.

Finally, thanks to my biggest supporters - my parents, Aydan and Ercan Kocel. I would not be here writing this thesis without their patience, unconditional love, and support.

**3D Seismic Survey Design: Coil Shooting, Multi-Component (3C) Receivers with Gulf  
of Mexico and Caribbean Case Histories**

-----

An Abstract of a Dissertation Presented to

the Faculty of the Department of Earth and Atmospheric Sciences

University of Houston

-----

In Partial Fulfillment

of the Requirements for the Degree

Doctor of Philosophy

-----

By

Eray Kocel

May 2015

## Abstract

The effectiveness of seismic imaging depends on numerous factors, beginning with how the data are acquired. The analyses presented in this theses show the importance of survey design, as individual parameters exert a strong influence over the resulting subsurface illumination. Survey design studies discussed here with different geological settings and geographical locations include: 1) Marine surveys with circular shooting for a subsalt target in the Gulf of Mexico, 2) Multicomponent land seismic survey designs for an unconventional resource, and 3) Integrated geophysical data analyses and survey design for a blind fault imaging at the 2010 Haiti earthquake epicentral area. In the case of marine surveys, the dual-coil design provides full-azimuthal coverage, whereas the Wide-azimuth surveys (WAZ) contain some acquisition footprints due to their straight-line geometry with limited-azimuthal coverage. Survey design optimization quantified the WAZ survey as having 20 % less illumination intensity than the dual-coil survey. For the multicomponent survey design, we analyzed the effects of  $V_P/V_S$  values (2, 4, and 6), target depth (800, 1,600, and 3,200 m) and orthogonal or slanted shot geometries. The updip shifting of the illumination area due to target layer inclination ( $5^\circ$ ,  $15^\circ$ , and  $30^\circ$ ) required longer offsets to fully capture the seismic data. Staggered (periodically shifted) receiver lines achieved smaller bin sizes (6.25 m vs 25 m) with a very little additional acquisition effort. We also consider a case history from Léogâne fan-delta in Haiti, where some of the worst shaking was located by the 2010 Haiti earthquake. This intense shaking of the fan-delta area was attributed to either activation of a blind thrust fault, ~4 km beneath the surface, or to a strike-slip motion along a shallow, ground-breaking fault. We acquired seismic, gravity,

and GPS data which were integrated with remote sensing studies. Our integrated results indicated disruptions of the near-surface material in the Léogâne region. Survey design studies suggested that multiple 2D seismic lines with 6 km offsets and optional marine surveys may be required to image the proposed blind fault. This thesis suggests novel seismic survey designs for a variety of subsurface geologies.

# Table of Contents

Acknowledgements.....	iii
Abstract .....	vi
Table of Contents .....	viii
List of Figures .....	xii
List of Tables .....	xxxi
List of Abbreviations .....	xxxiii
Chapter 1 - Introduction.....	1
1.1 Motivation and objective.....	1
1.2 Structure of the dissertation.....	3
Chapter 2 - 3D-Seismic Survey Design and Optimization: Coil vs WAZ Geometries .....	7
2.1 Introduction .....	7
2.2 Geology .....	9
2.3 Multi-vessel shooting and data conditioning .....	10
2.3.1 Dual-coil design.....	11
2.3.2 Wide-azimuth design (WAZ) .....	14
2.3.3 Data conditioning .....	16

2.4 Fold and azimuthal coverage comparison for a flat layer .....	18
2.4.1 Dual-coil survey .....	19
2.4.2 Wide-azimuth survey.....	22
2.4.3 Dual-coil vs WAZ geometry results .....	25
2.5 Illumination comparison of dual-coil and WAZ geometry for a subsalt prospect..	26
2.5.1 Subsurface geological model.....	26
2.5.2 3D ray tracing illumination results .....	29
2.6 Survey optimization .....	32
2.7 The wave-equation illumination.....	37
2.7.1 Wave-equation illumination results.....	39
2.8 Ray-based method versus the wave-equation-based method .....	42
2.9 Conclusions .....	43
2.10 Future Considerations .....	45
2.10.1 Ellipse design.....	45
2.10.2 Updated ellipse design.....	50
2.10.3 Controlled streamer feathering .....	53
 Chapter 3 - Multicomponent (3C-3D) Seismic Survey Design .....	 57
3.1 Introduction .....	57
3.2 Multicomponent data acquisition and converted-wave.....	59

3.3 Test surveys.....	61
3.3.1 Live receiver patch and shot sequence .....	85
3.3.2 Dipping target.....	88
3.3.3 Receiver-line stagger .....	89
3.3.4 Comparison of staggered and non-staggered receiver lines .....	90
3.3.5 Alternative design, slanted-shot lines with receiver-line stagger .....	92
3.4 Conclusions .....	96
 Chapter 4 - Near-Surface Geophysical Investigation of the 2010 Haiti Earthquake Epicentral Area: Léogâne, Haiti .....	 99
4.1 Introduction .....	99
4.2. Geological settings of Haiti and the 2010 Haiti earthquake epicentral area .....	102
4.3 Data and methods .....	107
4.3.1 Laboratory measurements.....	108
4.3.2 Seismic surveys .....	110
4.3.3 Gravity data .....	119
4.4 Interpretation and discussion.....	120
4.5 Conclusions .....	126
4.6 Seismic survey design for the future surveys.....	128

4.6.1 Land surveys - Surface seismic .....	128
4.6.2 Land surveys - Vertical seismic profiling.....	136
4.6.3 Marine Surveys.....	137
 Chapter 5 - Summary and Recommendations .....	 140
Appendix.....	146
References.....	148



## List of Figures

Figure 1.1. Satellite image (from Google earth) shows the locations for the survey sites presented in this thesis (yellow dots) and the geographical extension of the Eagle Ford formation over U.S. and Mexico (highlighted with red color).....	6
Figure 2.1. Dual-coil geometry layout. The red line represents sail lines for the receiver vessels, while blue lines represent the streamers connected to receiver vessels. The dashed grey line represents sail lines for the shot vessel. The shot sequence for the vessels are S1-S3-S2-S4. The long offsets were produced by sources shooting across the coil. Each vessel sails along a separate circle, these circle centers were offset in X direction by $dx$ (1,500 m) and in Y direction by $dy$ (1,000 m).....	11
Figure 2.2. Comparison of coil center distributions where white-colored circles represent the coil centers (139 coils in total). (a) Pseudorandom coil center grid. (b) Regular coil center grid.....	13
Figure 2.3. Schematic diagram of Wide-azimuth survey layout. Red line represents the streamers and green dot represents the air gun locations. Vessels are separated by approximately 1 km and each vessel marked by numbers according to the shot sequence.....	16

Figure 2.4. Single coil layout for the 2 x 4 configuration, red line and red dots represents the shot points and blue lines represent the streamers. (a) Before the shot decimation. (b) After the shot decimation by a factor of nine.....	17
Figure 2.5. WAZ survey layout, red dots represents the shot points. Dashed gray lines represents the sail lines. (a) Before the shot decimation. (b) After the shot decimation by a factor of five.....	18
Figure 2.6. Shot distribution of a dual-coil survey for an area of 2,050 km <sup>2</sup> . Red lines represent the shot points and blue lines represent two of the receiver spreads.....	19
Figure 2.7. Dual-coil survey fold coverage and bin azimuth/offset distributions. Bin size is 25 m x 25 m. (a) Spider diagram indicating the azimuthal coverage for within the bin for selected areas. (b) Rose plot to show the offset and azimuth distribution (FAZ). Red color represents the higher values, cool colors represents the lower values.....	20
Figure 2.8. Dual-coil survey fold coverage with bin azimuth/offset distributions, obtained by regular coil distribution (144 in total). Warmer colors represents higher fold values. (a) Coil distribution over 2,000 km <sup>2</sup> area. (b) Fold coverage map with a bin size of 25 m by 25 m.....	21

Figure 2.9. Shot distribution of WAZ survey for an area of 2,400 km<sup>2</sup>. Green and orange lines represents the shot points and blue lines represent the two receiver spreads.....23

Figure 2.10. The WAZ survey fold coverage and bin azimuth/offset distributions overlain with the dual-coil survey extensions (gray dashed line). Bin size is 25 m x 25 m. (a) Spider diagram indicating the azimuthal coverage for within the bin for selected areas. (b) Rose plot to show the offset and azimuth distribution (wide-azimuth) for the entire survey. Red color represents the higher values and cool colors represent the lower values.....24

Figure 2.11. Subsurface geological model with P-wave seismic velocities, in-line view. The red color represents higher P-wave velocities, cooler colors represents lower P-wave velocities. An extensive salt body with high P-wave velocities is shown.....27

Figure 2.12. Closer view of the subsurface geological model with the horizon of interest. (a) Layers are colored by their depth (except for the salt body). (b) The target area over the horizon of interest and anomalous structures highlighted by a black colored circle.....28

Figure 2.13. Comparison of illumination maps for a subsalt horizon by 3D ray tracing analyses and a closer view of a target area (145 km<sup>2</sup>) for the dual-coil survey (a and c), and

the WAZ survey (b and d). Warm colors represent higher hit counts (denser illumination), cooler colors represent lower hit counts (sparse coverage and lower illumination density).....30

Figure 2.14. (a) Closer view of the horizon of interest, colored by the depth (warm colors represent shallower depths). (b) The associated illumination factor distribution. The illumination factor is up scaled by 10,000 during the calculations.....33

Figure 2.15. Survey design optimization results for dual-coil geometry (a and c) and WAZ geometry (b and d). Purple colored circles and lines represent the most contributing coils and sail lines. Red colored circles and lines represent the least contributing coils and sail lines. Relative to the Coil survey, the WAZ geometry had 20 % less illumination intensity.....35

Figure 2.16. The distribution of source and receiver grid with selected target area over subsalt horizon. The subsurface model is colored by the depth (warm colors represent shallower depths). (a) Actual shot points over the target area. (b) Receiver grid at the surface.....39

Figure 2.17. Target horizon and calculated illumination energy comparison. (a) The color map on the horizon represents the hit count distribution obtained from 3D ray-tracing studies. (b) The color map on the horizon represents the illumination amplitude obtained

from wave-equation illumination (surface area map was obtained by interpolation). (c) Illumination amplitude obtained from wave-equation (circles) illumination overlain on top of the hit counts obtained from ray tracing studies.....40

Figure 2.18. (a) Energy distribution maps for the shot points at the most contributing coil. The warm colors represent the higher energies which corresponds to the most contributing shots on each coil (b) Energy distribution for two most contributing coils, overlain with the horizon of interest colored by the depth (warm colors represent shallower depths).....41

Figure 2.19. Ellipse geometry layout. (a) An ellipse with the dimensions of the axes. (b) Three adjacent ellipses used for the further analyses. (c) Vessel layout for the ellipse geometry. The red line represents the sail lines for the receiver vessels; the dashed grey line represents sail lines for the shot vessels. The shot sequence for the vessels are S1-S3-S2-S4. The long offsets were produced by sources shooting across the ellipses. Each vessel sails along a separate ellipse, these ellipse centers were offset in X direction by dx (1,000 m) and in Y direction by dy (1,500 m).....47

Figure 2.20. The coverage fold and bin azimuth/offset distribution for ellipse geometry. Bin size is 25 m x 25 m. (a) Spider diagram indicating the azimuthal coverage for within the bin for the selected areas. (b) Rose plot to show the azimuth/offset distribution for the

entire survey. Red colors represent the higher data values, cool colors represent the lower data values.....48

Figure 2.21. Comparison of a proposed dual-coil and ellipse geometry for the test survey. Circumference of both the coil and the ellipse geometry are fixed to the ~38 km. Red lines represent the sail lines for the dual-coil design; the dashed gray lines represent sail lines for the ellipse design. Four circles are needed to cover the test survey area whereas three ellipses would be enough for such a survey.....49

Figure 2.22. The coverage fold and bin azimuth/offset distributions for dual-coil geometry. Bin size is 25 m x 25 m. (a) Spider diagram indicating the azimuthal coverage within the bin for selected areas. (b) Rose plot to show the offset and azimuth distribution for the entire survey. Red colors represent the higher data values, and cool colors represents the lower data values.....50

Figure 2.23. Updated ellipse geometry layout. (a) An ellipse with dimensions of the axes. (b) Test survey that included two adjacent ellipses, separated in X direction by 1500 m. (c) Vessel layout for an individual ellipse. The blue lines represent sail lines for both source and receiver vessels. The shot sequence for the vessels were S1-S3-S2-S4.....52

Figure 2.24. The coverage fold and bin azimuth/offset distributions for the test survey with the updated ellipse geometry. Bin size is 25 m x 25 m. (a) Spider diagram indicating the azimuthal coverage within the bin for selected areas. (b) Rose plot to show the azimuth/offset distribution for the entire survey. Red colors represent the higher data values and cool colors represent the lower data values.....53

Figure 2.25. The effect of streamer feather. (a) No flare. (b) 5° streamer flare. (c) 15° streamer flare.....55

Figure 2.26. The effect of streamer flare angle over fold maps and rose diagrams for offset and azimuth distributions. (a) No flare. (b) 5° streamer flare. (c) 15° streamer flare.....56

Figure 3.1. Map of unconventional basins around the world for both current (red colored) and prospective (yellow colored) shale plays (modified from EIA, 2013).....57

Figure 3.2. Illustration of PP and PS waves. (a) Down going P-wave reflects as P-wave with symmetric ray path (PP-wave). (b) Down going P-wave reflects as S-wave with asymmetric ray path (PS-wave). The conversion point trajectory with respect to the depth is shown with the gray dashed line.....60

Figure 3.3. Multicomponent (3C-3D) test survey layout for 10.5 km<sup>2</sup> area with a bin size of 25 m by 25 m (gray line). Blue dots illustrate the receiver locations and red lines represent the shot points. Both shots and receiver lines are 150 m apart. The spacing for shot points and receiver locations is 50 m.....62

Figure 3.4. PS fold map comparison for various  $V_P/V_S$  values (for a horizontal layer at 1,600 m depth) with a bin size of 25 m by 25 m. Warm colors indicate higher folds. (a) PP fold map. (b) PS fold map for  $V_P/V_S=2$ . (c) PS fold map for  $V_P/V_S=4$ . (d) PS fold map for  $V_P/V_S=6$ . Larger area of coverage with less fold is observed with increasing  $V_P/V_S$ .....63

Figure 3.5. Fold map comparison for various target layer depths with a bin size of 25 m by 25 m and using a constant  $V_P/V_S$  value of 2. Warm colors indicate higher folds. (a) PP fold map for a horizontal layer at 800 m depth. (b) PS fold map for the horizontal layer at 800 m depth. (c) PS fold map for the horizontal layer at 1,600 m depth. (d) PS fold map for the horizontal layer at 3,200 m depth. The shifting of CCP away from the receivers, for greater depths, is controlled by the asymmetric raypath.....66

Figure 3.6. Alternative geometry layouts with PP and PS fold map comparison (warm colors indicate higher folds) for the 3D test surveys with a bin size of 25 m by 25 m. Blue lines illustrates the receiver grid and the red lines represent the shot points. All analyses



are completed using  $V_P/V_S=2$  and for a horizontal layer at 1,600 m depth. (a) North-south trending receivers are centered in a greater east-west trending shot lines. (b) East-west trending receivers are centered in a greater north-south trending shot lines. (c) North-south trending shots are centered in a greater east-west trending receiver lines (d) East-west trending shots are centered in a greater north-south trending receiver lines.....68

Figure 3.7. PP and PS fold map comparison for parallel geometry with a bin size of 25 m by 25m. Warm colors indicate higher folds. Blue lines illustrate the receiver grid and red lines represent the shot points. All analyses are completed for  $V_P/V_S=2$  and for a horizontal layer at 1,600 m depth. (a) Shots are centered on the receiver lines, parallel to the greater receiver grid. (b) Receivers are centered on the shot lines, parallel to the greater shot grid. (c) Shots are located between the receiver lines (75 m offset), and parallel to the receiver lines. (d) Receivers are located between shot lines (75 m offset), and parallel to the shot lines.....71

Figure 3.8. Fold map and offset and azimuth diagram comparison for PP and PS surveys between orthogonal and slanted geometries with a bin size of 25 m by 25 m. All analyses are completed for  $V_P/V_S=2$  and for a horizontal layer at 1,600 m depth. Blue lines illustrate the receiver grid and red lines represent the shot points. Warm colors indicate higher data values. (a) Orthogonal geometry. (b) Slanted geometry ( $45^\circ$  angle between shot and receiver lines). Both designs have the exact same number of receivers and a similar total

number of shots. Orthogonal geometry provides relatively irregular distribution of offsets and azimuthal coverage when compared to the slanted geometry.....73

Figure 3.9. 2D ray shooting experiment for PS-waves over 15° dipping plane, only the upgoing S-waves are shown for the display purposes. Shot point is illustrated with black colored star, orange lines represents the downdip rays and blue lines represents the updip rays. Subsurface coverage area is colored with red line. Downdip rays are concentrated over relatively smaller area whereas the updip rays are distributed over larger area. Therefore, higher folds are expected in the downdip and lower folds with bigger illumination area is expected in the updip.....75

Figure 3.10. Fold map comparison for PP and PS surveys, with a bin size of 25 m by 25m and a constant  $V_P/V_S$  of 2, between horizontal and dipping layers. Warm colors indicate higher folds. Blue lines at the surface illustrates the receiver grid and red lines represent the shot points. The black dot represents the center of shot grid. (a) PP and PS fold map for a horizontal layer at 1,600 m depth. (b) PP and PS fold map for 15° dipping layer with azimuth of 180°. (c) PP and PS fold map for 30° dipping layer with azimuth of 180°.....76

Figure 3.11. The effect of additional receiver lines for both PP and PS fold distribution over the dipping layer with a bin size of 25 m by 25 m. Warm colors indicate higher folds.

Blue lines at the surface illustrate the receiver grid and red lines represent the shot points. Total number of 6 receiver lines are added to original geometry. The black dot represents the center of shot grid. (a) PP and PS maps for the original geometry. (b) PP and PS maps for the extra receiver lines towards the updip direction. (c) PP and PS maps for the extra receiver lines towards the downdip. The shifting of the illumination area in updip is stronger for PS studies due to the asymmetric raypath. In terms of illumination, most benefit is obtained by adding the receiver lines in the updip as opposed to downdip.....78

Figure 3.12. The effect of the various bin size over the PP and PS fold maps, warm colors indicate higher fold values. (a) Orthogonal geometry using 25 m by 25 m bin size. (b) Orthogonal geometry using 12.5 m by 25 m bin size. (c) Orthogonal geometry with staggered receiver lines using 12.5 m by 25 m bin size. Original design does not support the smaller bin sizes and resulted in empty bins for PP survey and fold striping for the PS survey. The receiver-line stagger achieved smaller bin sizes without any major artifact on fold maps.....81

Figure 3.13. Two layer subsurface models for the calculation of surface recording time using PS rays, corresponding  $V_P$  and  $V_S$  values for the layers are annotated. Black lines in the subsurface models represents the reflected rays from the boundary, source rays were not displayed for display purposes. (a) Subsurface model with horizontal layer at 1,600 m depth and recorded reflections times (in seconds). (b) Subsurface model with 15° dipping

layer towards south and recorded reflections times (in seconds). (c) Subsurface model with 30° dipping layer towards south and recorded reflections times (in seconds).....83

Figure 3.14. Sketch of the 3C-3D seismic survey with some of the acquisition parameters. Blue square outlines the receiver grid (81 lines) and the red square outlines the shot grid (67 lines). The survey was completed with three zipper blocks.....85

Figure 3.15. The sketch of shot salvos with their effect on PS fold (warmer colors indicate higher values of fold) using bin size of 25 m by 25m. Blue dots indicate the receivers and red dots indicate the shot points. (a) One shot salvo. (b) Three shot salvo. (c) Five shot salvo. Higher salvo rolls introduced acquisition footprints over the fold maps.....87

Figure 3.16. PS fold map comparison between the horizontal layer and the dipping layer, warm colors indicate higher folds. (a) PS Fold map for horizontal layer at 1,600 m depth. (b) PS Fold map for 5° dipping layer towards Southwest. (c) 3D PS fold map for 5° dipping layer towards Southwest. Blue lines at the surface illustrate the receiver grid and red lines represent the shot lines.....88

Figure 3.17. Updated survey geometry with staggered receiver line pattern to obtain smaller bin sizes. Gray lines represent the individual bins (6.25 m by 25 m). Red dots represent the shot points and blue dots represent the receiver locations.....89

Figure 3.18. PS fold map comparison for different bin sizes, smaller bin size are achieved by the receiver-line stagger, warmer colors indicate higher fold values. (a) PS fold map for using bin size of 25 m by 25 m. (b) PS fold map using bin size of 6.25 m by 25 m. (c) PS fold map, for the offsets between 500 m to 2,500 m, using bin size of 25 m by 25 m. (d) PS fold map, for the offsets between 500 m to 2,500 m, using bin size of 6.25 m by 25 m.....91

Figure 3.19. Rose plot comparison for all the offsets using different bin sizes, smaller bin sizes are achieved by the receiver-line stagger. (a) 25 m by 25 m bin size. (b) 6.25 m by 25 m bin size.....92

Figure 3.20. Multicomponent survey layout with slanted-shot lines ( $45^\circ$ ), blue lines represent the receivers and the red lines represent the shots.....93

Figure 3.21. PS fold map and azimuth/offset distribution (shown as rose plot) comparison between orthogonal and slanted-shot line geometry. Both surveys has receiver-line stagger

to achieve 6.25 m by 25 m bin sizes. Warmer colors indicate higher data values. (a) PS fold and rose plot map for the orthogonal geometry. (b) PS fold and rose plot map for the slanted-shot line geometry. (c) PS fold and rose plot map for the orthogonal geometry between 500 m to 2,500 m offsets. (d) PS fold and rose plot map for the slanted-shot line geometry between 500 m to 2,500 m offsets.....94

Figure 4.1. (a) Location of the island of Hispaniola (inside the blue box) in the northern Caribbean. (b) Active, left-lateral strike-slip faults shown in red in the Hispaniola region separating the Gonâve microplate from the larger North America plate to the north and Caribbean plate to the south (modified from Calais et al., 2010). The dashed square indicates the location of the study area of the Léogâne fan-delta. The yellow star indicates the epicentral location of the 2010 earthquake from Douilly et al. (2013).....100

Figure 4.2. (a) Location of the Léogâne fan-delta, 30 km west of the capital city of Port-au-Prince. (b) Digital elevation map of the southwestern Léogâne fan-delta showing the locations of the seismic reflection lines described in this paper: Line A was collected in 2012 using a sledge hammer source; seismic data along Lines B, C, and D were collected in 2013 using the accelerated weight drop. Warm colors indicate higher elevations (about 180 m) and cooler colors indicate low elevations. Enriquillo Plantain Garden Fault Zone (EPGFZ) is drawn with black and white dashed line. Red dashed line represents the proposed geometry (Douilly et al., 2015) for the Léogâne fault .....105

Figure 4.3. (a) The deformation observation of the Léogâne area along with the interferogram and bathymetry map (shown as contour lines). White circles show the aftershock locations (Douilly et al., 2013). The black and white dashed line in the south represents Enriquillo Plantain Garden Fault Zone (EPGFZ) and interpreted folding axis is shown with red dashed line. (b) Satellite photograph of coral reef off the coast of the Léogâne fan-delta before the earthquake (from Google Earth, 2005). (c) Satellite photograph of uplifted coral reef after the earthquake (from Google Earth, 2010). Blue dots on the coastline show the amount of coral reef uplift (in meters) during the 2010 earthquake (Hayes et al., 2010).....106

Figure 4.4. (a) Ultrasonic transducers with the rock samples that were used in velocity measurements. Orientation of the axes for the velocity measurements is drawn in yellow. (b) Parts of sample A (limestone) used for density measurements. (c) Parts of sample B (sandstone) used for density measurements. (d) Parts of sample C (basalt) used for density measurements.....109

Figure 4.5. Representative seismic shot gathers (with AGC scaling) from vertical geophones. (a) Line A (4.5 kg hammer source). (b) Line B (40 kg accelerated weight drop). (c) Line C (tilted 40 kg accelerated weight drop). (d) Line D (40 kg accelerated weight drop). First arrival, surface-wave, and air-blast velocities are annotated. Dominant frequencies are approximately 50 Hz.....111

Figure 4.6. Comparison of true amplitude spectra for seismic line A (hammer line), and seismic line B (accelerated weight drop).....112

Figure 4.7. P-wave travelttime tomography results. (a) Line A: P-wave velocity section using an 80 m deep model. (b) Line B: P-wave velocity section using an 80 m deep model. The red color represents relatively higher P-wave velocities (2,250 m/s), and the green color represents slower P-wave velocities. Strata above the black dashed line are relatively slow and interpreted as seismically weaker layers.....113

Figure 4.8. The 2-D S-wave velocity profiles determined from surface-wave inversion. (a) Velocity profile for line A. (b) Velocity profile for line D. (c) Velocity profile for line B. Red colors represent velocities around 200 m/s. Dashed lines indicate a high-velocity structure over a low-velocity region. The shot location for the S-wave reflection gather (Figure 4.9) is shown with a flag.....115

Figure 4.9. Analyses of S-wave source and horizontal receiver shot gather from line C showing S-wave reflections. (a) Selected shot gather, reflected signals highlighted in yellow. (b) Velocity semblance for the dashed box area. Black boxes indicate the picked stacking velocities. (c) Dix interval velocities calculated from the stacking (as RMS) velocities. These are interpreted as pure shear velocities.....116



Figure 4.10. S-wave velocity profiles for Port-au-Prince (from Cox et al., 2011) and Léogâne (Surface-wave inversion results for the first 18 m combined with a shot gather from line C). Note that the Léogâne near-surface sediments have considerably lower velocities than the Port-au-Prince area near-surface sediments.....	117
Figure 4.11. Line A seismic reflection data. (a) P-wave stacking velocity section. (b) Time-migrated seismic section.....	118
Figure 4.12. Line B seismic reflection data. (a) P-wave stacking velocity section. (b) Time-migrated seismic section.....	118
Figure 4.13. (a) Time-migrated seismic section of line D. (b) P-wave stacking velocity section for line D (c) Time-migrated seismic section of line B. AGC is applied on both seismic sections for display purposes. Note the reasonable correlation of the two seismic images. The white dashed line represents an approximate 2° dip of the layers toward the south.....	119
Figure 4.14. Integration of observations of coseismic folding during the 2010 Haiti earthquake. (a) Uplift of coastal coral with the gravity data inset. Line A coverage is indicated. (b) Displacement inferred from radar interferometry results between along the coast of Léogâne with the coverage of the line A indicated. (c) Aftershock events (Douilly et al., 2015) in the vicinity of line A. (d) Aftershock events around the north-south paved	

highway ~3 km east of our lines with the proposed geometry for the Léogâne fault.....123

Figure 4.15. (a) Interpretive cross-section for the Léogâne fan and dashed blue line showing the proposed fault geometry for the Léogâne fault blind reverse fault (modified from Douilly et al., 2013). (b) Free-air corrected gravity results, B-B'. (c) Line A seismic section with overlain seismic velocities, A-A' .....125

Figure 4.16. Proposed geometry for future seismic surveys in the Léogâne area. The 2D lines are 6 km long and colored by PP fold. Warmer colors represent the higher fold values.....130

Figure 4.17. Proposed geometry for future seismic surveys in the Léogâne area. The 2D lines are 6 km long and colored by PS fold. Warmer colors represent the higher fold values.....131

Figure 4.18. 2D simple earth model that contains four layers with corresponding velocities and densities. The location and geometry of the proposed Léogâne fault is shown with the blue dashed line. ....132

Figure 4.19. (a) Reflection and refraction event for PP rays over the four layer simple earth model, source rays are not shown for display purposes. Shot location is marked with a red

flag. (b) Surface recording time, in seconds, for reflecting rays. (c) Surface recording time, in seconds, for refracting rays.....134

Figure 4.20. (a) Reflection and refraction event for P-P-S rays over the four layer simple earth model, source rays are not shown for display purposes. Shot location is marked with a red flag. (b) Surface recording time, in seconds, for reflecting rays. (c) Surface recording time, in seconds, for refracting rays.....135

Figure 4.21. (a) The VSP geometry; red lines at the surface indicate the shot locations and black line in the subsurface represent the receiver locations (the trajectory of the well). (b) Resulting PP fold map; warmer colors indicate the higher fold values. (c) The cross line view of the PP fold map.....137

Figure 4.22. Area of the proposed marine survey between Léogâne and Grand Goave; the 3D proposed geometry for the Léogâne fault (modified from Hayes et al., 2010; Douilly et al, 2015). Green lines represent sail lines, the black dashed line represents the extension of the EPGFZ and the red dashed line indicates the Léogâne fault.....139

## List of Tables

Table 1. Specifications of seismic lines that were acquired in the 2012 and 2013 surveys over the Léogâne fan delta. The locations of the seismic lines are annotated in Figure 4.2.....	107
--	-----

Table 2. Summary of ranges of P-wave and S-wave velocities from ultrasonic laboratory measurements and their calculated density values for the collected hand samples.....	110
--	-----

## **List of Abbreviations**

AVA: Amplitude versus angle

AVO: Amplitude versus offset

CCP: Common conversion-point

CMP: Common mid-point

EPGFZ: Enriquillo Plantain Garden fault zone

FAZ: Full-azimuth

GPS: Global positioning system

MASW: Multi channel analyses of surface-waves

NEHRP: National earthquake hazard reduction program

RMS: Root mean square velocity

$V_P$ : P-wave velocity

$V_S$ : S-wave velocity

$VS^{30}$ : Average S-wave velocity for the top 30 m

VSP: Vertical seismic profile

WAZ: Wide-azimuth

3C: Three-component

# **Chapter 1**

## **Introduction**

### **1.1 Motivation and objective**

The primary motivation of this dissertation is to show the importance of seismic survey design for seismic imaging while providing new acquisition geometries, as well as introducing target-based survey design and analyses.

The accuracy and efficiency of the proper illumination depends on many factors. Seismic imaging results may be less than adequate if the survey is located in an area characterized by complex overburden. In addition, conventional data acquisition and processing methods may not fully address the challenges posed by the subsurface geology and geophysical complexities. Hence, the integrated approach of survey design and modeling is one of the critical components for the success of seismic surveys.

To achieve these objectives, it is crucial to understand and determine the geophysical parameters that would control the resulting seismic images. In turn, this requires the designing a full scale seismic surveys for the various geometries from different geological settings and geographical regions. Advanced seismic surveys are generally acquired after

the selection of specific prospects over existing seismic data. However, the survey designing process usually does not consider the properties of the target area(s), but rather they are completed with some generalized assumptions. With the introduction of new methods, such as target-oriented survey design and analyses (Moldoveanu et al., 2013), we are closing the loop between survey design parameters and their contributions with the resulting images using ray-based methods. To overcome some of the simplifications of the ray-based methods, we employ wave-equation-based illumination analyses (Lapilli et al., 2010). This method has long existed (Xie et al., 2003); however, it recently became increasingly practical with advancements in computing technology. Additional proposals include new survey geometries of the marine data acquisition that would complement both WAZ and coil designs, but would be more suitable for spatially limited areas.

In the case of multicomponent studies, the converted-wave (P-to-S on reflection) survey design is more complex than the conventional P-wave seismic designs due to asymmetric raypaths. Many factors control the PS illumination, which otherwise would have a limited effect on PP studies. By providing a detailed review and analyses concerning the effects of geological and geophysical parameters for converted-wave imaging, we are attempting to establish a link between some of the conceptual theories and real world applications, as well as highlighting some of the pitfalls.

The success of the target-based survey design studies largely based on the accuracy of the subsurface models. Unfortunately, pre-existing data may not always be available and

therefore lack of subsurface models can limit the success of the survey design studies. An example for such conditions would be in the Léogâne fan, Haiti. A challenging task of data acquisition, data processing, and data integration was completed to generate a subsurface model. This model is later used for survey design analyses that would highlight some of the critical requirements for future surveys.

The majority of the analyses presented in this dissertation are accomplished using Omni, Vista, Omega and Petrel software. The subsurface model used in the marine studies was kindly provided by the WesternGeco. The geophysical data presented in Chapter 4 have been acquired, processed, and interpreted by our research team in Allied Geophysical Laboratories at the University of Houston.

## 1.2 Structure of the dissertation

The basic structure of the survey design studies discussed in this dissertation can be divided into three parts, i) comparing the illumination results of dual-coil and wide-azimuth (WAZ) surveys for complex geologies at the Gulf of Mexico (Chapter 2), ii) a detailed survey design guide for the multicomponent seismic exploration (Chapter 3), and iii) an integrated near-surface investigation to better understand the subsurface structure at the Léogâne fan, Haiti and designing future seismic surveys to obtain deeper images (Chapter 4). Figure 1.1 shows the different survey locations with an outline of a well-known example of an unconventional play, the Eagle Ford formation (over U.S. and Mexico).



The chapters presented in this thesis are structured to be independent from one another, using different cases and geographical regions. However, emphasis has been placed on the survey design studies within each chapter. We believe this particular approach enabled us to overlook the concerns relating to survey design rather than the discussion of a single problem, which has provided valuable insights for various real world applications.

Chapter 2 includes the designing of a full scale marine survey with multiple vessels using dual-coil and WAZ geometries. These geometries were initially tested for relatively simple seismic attributes (e.g., fold, azimuth/offset distributions, acquisition time, etc.) over a flat horizon. More detailed comparisons were completed using relatively advanced attributes (e.g., hit count maps) over complex geologies at great depths (~10.5 km). Target-oriented studies such as survey design optimization used to quantify the survey success for the illumination of a specific target, this method also provided critical information regarding the most contributing survey parts for the illumination of a target area. Another target-oriented method, wave-equation illumination, had the advantage of properly accounting for the wave nature of the propagation field in complex geological settings and provided both subsurface and surface maps with decreased modeling cost. In this chapter, we are also proposing new, alternative survey designs (e.g., adjacent ellipse design, perpendicular ellipse design, and controlled streamer flare) for certain conditions that might otherwise prohibit the deployment of currently used geometries.

Chapter 3 is related to an in-depth review of the multicomponent survey design for an unconventional play. Only a limited number of articles have been published that discuss multicomponent survey designs in detail, with illumination maps. We designed this chapter to be a survey design reference guide for future researchers who would like to invest more in converted-wave surveys. Various geometry options were tested for the illumination of relatively shallower subsurface targets. In addition to geometry, the effect of  $V_P/V_S$  values, target depth, target dip, and bin sizes have also been presented.

Chapter 4 discusses the integrated geophysical case study from the Léogâne fan, Haiti. This project was supported by the SEG's Geoscientists Without Borders group. Gravity, seismic, and GPS data were acquired during the 2012 and 2013 surveys. These data integrated with recent remote sensing studies and field observations to better understand the subsurface structure and generate a subsurface model. This model was also used for survey design purposes to highlight some of the acquisition requirements for future seismic surveys. To our knowledge, there has been no prior seismic-reflection studies in Haiti. In addition to examining the potential causes and effects of the earthquake in the Léogâne fan-delta area, this investigation provided some basic parameters that can be used as background information for the further research at this region.

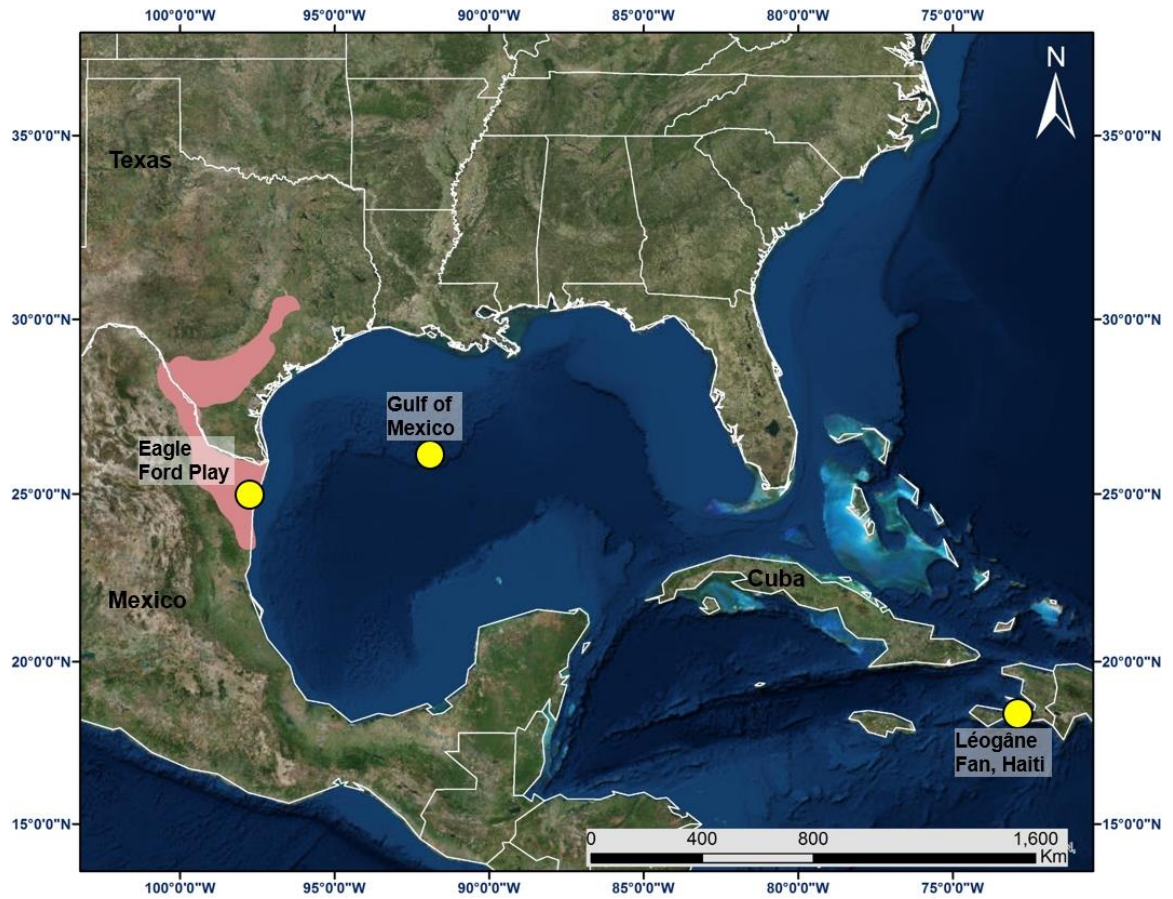


Figure 1.1. Satellite image (from Google earth) shows the locations for the survey sites presented in this thesis (yellow dots) and the geographical extension of the Eagle Ford formation over U.S. and Mexico (highlighted with red color).

## **Chapter 2**

### **3D-Seismic Survey Design and Optimization: Coil vs WAZ Geometries**

#### **2.1 Introduction**

In geologically complex areas, the limited-azimuthal coverage obtained by straight-line marine acquisition methods (i.e., narrow-azimuth geometry) can result in the target area being poorly illuminated (Diagon et al., 2011). These surveys are usually acquired by a limited number of vessels and have been used for a long time to image a variety of geologic circumstances. With increasing interest in subsalt and presalt prospects, newer acquisition geometries with extended offsets have been proposed. Wide-azimuth multi-streamer acquisition has been shown to deliver relatively improved illumination and resolution for subsalt exploration (Diagon et al., 2011). Extended offsets for Wide-azimuth (WAZ) surveys can result in enhanced target illumination, but with a significant increase in survey cost and acquisition time. Another drawback of the straight-line geometries is the amount of non-productive time involved, as a result of the extra time required to turn the vessel between the lines. It was noted from previous researches that “the typical turning time for each sail line is more than three hours, which adds up to several weeks for a large survey” (Buia et al., 2008).

Advantages of circular shooting geometries for marine acquisition were initially proposed by French (1984). However, it was only in 2009 that coil surveys with multiple vessels became feasible, due to improvement in acquisition techniques and processing power (Moldoveanu and Kapoor, 2009). Coil geometry is achieved by vessels sailing along individual, overlapping circles with extra-long offsets that are produced by sources shooting across the coil. At the completion of each circle, the vessels transit to the next circle. This pattern of acquisition assures continuous shooting, which minimizes the down time when compared to straight-line acquisition techniques (Wide-azimuth, rich-azimuth, narrow-azimuth, etc.). The amount of non-productive time for the straight-line geometries can be as high as 50 % of the total time required to complete the survey (Buia et al., 2008).

For a subsalt target in the Gulf of Mexico, a comparison between WAZ and coil surveys were undertaken to assess illumination. 3D ray tracing was carried out to generate target illumination maps. The target illumination maps were then evaluated using different attribute maps. The hit count maps were predominantly used for further analyses.

Illumination maps over the horizon of interest enabled us to determine the likely quality of imaging results. Considering the immense size of the marine surveys, it can be critical to quantify and prioritize the parts of the acquisition geometry that account most for the illumination of the horizon of interest. To understand the contribution from the subset of acquisition geometries (sail lines for WAZ survey and individual-coils for Coil survey), an

optimal survey design technique was introduced (Moldoveanu et al., 2013). This technique depended on ray-based illumination analyses.

Although ray-based illumination methods can provide satisfactory results, they may also suffer from accuracy in geologically complex regions (i.e., subsalt targets). Considering the existence of ultra-deep water and the presence of thick salt body, we introduced a wave-equation-based illumination method (Lapilli et al., 2010) to overcome these particular complexities. Wave-based methods can accurately model the seismic wave propagation in complex geology, providing more reliable results. This method enabled the generation of target-oriented illumination maps and shot weights, quantifying the contribution of the shots for selected acquisition geometry for imaging a given target.

## 2.2 Geology

The Gulf of Mexico is a passive margin which is well known to have thick sedimentary deposits, up to 18 km (Galloway, 2011). Historically, this margin experienced rifting episodes which were followed by crustal extension, salt emplacement, and mobilization (Worrall and Snelson, 1989; Salvador, 1991). The salt deposition was believed to emerge in the Middle to Late Jurassic after the stages of rifting (Salvador, 1991; Sawyer et al., 1991; Watkins et al., 1995). The thickness and wide distribution of the salt suggests that the salt deposition may be in effect throughout the Middle Jurassic and possibly into the

Late Jurassic (Salvador, 1991). As sediment accumulation occurred almost continuously throughout the history of the Gulf of Mexico, its weight caused the buried salt to mobilize and form allochthonous salt sheets that moved upward into the shallow subsurface. These horizontally extensive salt bodies created trapping mechanisms for oil and gas. It wasn't until the 1990's that the existence of subsalt and pre-salt sedimentary layers were discovered. As most of the "easy" oil was already discovered in this region, the imaging studies began focusing on these more challenging targets, such as subsalt plays.

### 2.3 Multi-vessel shooting and data conditioning

Designing a multi-vessel seismic survey requires consideration of many geophysical parameters such as: offset and azimuth distribution, fold coverage, dominant frequency, and sampling. In addition, various operational issues also need to be taken into account. It was necessary to determine the survey size, shape, line changes, run-in, run-out. These factors must be taken into account to make acquisition a viable proposition (Mandraux et al., 2013)

For this purpose, two acquisition scenarios were compared using the azimuth and offset distribution with fold coverage to evaluate their efficiencies in terms of the success of subsequent geophysical imaging.

### 2.3.1 Dual-coil design

In the dual-coil geometry, there were two receiver vessels and two source vessels. Each receiver vessel also included a single source array. Therefore, a total number of four gun arrays were used, hence called a 2 x 4 configuration. The shot sequence was completed sequentially, alternating between source vessel #1(receiver vessel #1), source vessel #3 (receiver vessel #2), source vessel #2 and source vessel #4, and each vessel generated a shot that was recorded in two spreads. The vessels moved with the same speed at the pre-plot sail circles. A layout for a dual-coil geometry setting can be seen in Figure 2.1.

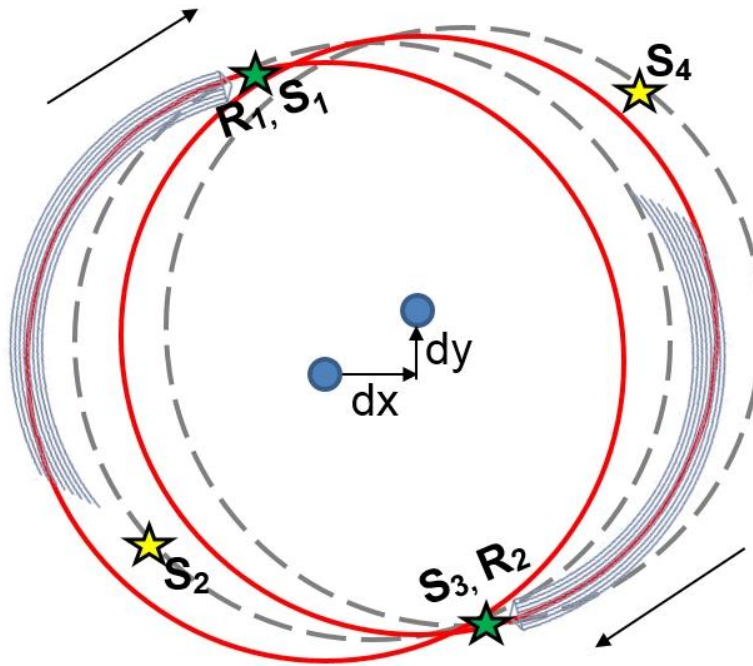


Figure 2.1. Dual-coil geometry layout. The red line represents sail lines for the receiver vessels, while blue lines represent the streamers connected to receiver vessels. The dashed grey line represents sail lines for the shot vessel. The shot sequence for the vessels are S1-S3-S2-S4. The long offsets were produced by sources shooting across the coil. Each vessel sails along a separate circle, these circle centers were offset in X direction by dx (1,500 m) and in Y direction by dy (1,000 m).



The long offsets were produced by sources shooting across the coil. Each vessel sailed along a separate circle, the circle centers were offset in X direction by  $dx$  (1,500 m) and in Y direction by  $dy$  (1,000 m). The difference between  $dx$  and  $dy$  was based on the survey objectives and helped to achieve greater lateral coverage. The separation of the vessels and the continuous rolling of the sail circles generated a non-regular shot distribution. The acquisition parameters were as follows:

- Number of sources: 4
- Number of streamers per vessel: 10
- Streamer separation: 120 m
- Streamer length: 10 km
- Receiver spacing: 25 m
- Shot interval for individual source: 100 m
- Circle diameter: 12 km

Unlike the non-productive time problems associated with the straight-line geometries (WAZ), dual-coil design reduces the acquisition time due to the efficiently obtained continuous acquisition (no line change). Previous studies have also shown that the dual-coil acquisition has the advantage of acquiring long offset and full-azimuth (FAZ) data without additional cost (Moldoveanu and Kapoor, 2009).

The continuous rolling of the overlapping circles generated an ease of non-regular shot distribution. Another design parameter that determines the shot and receiver distribution was the coil center distribution. The coil centers can be designed to be either regular or pseudo-random (Figure 2.2).

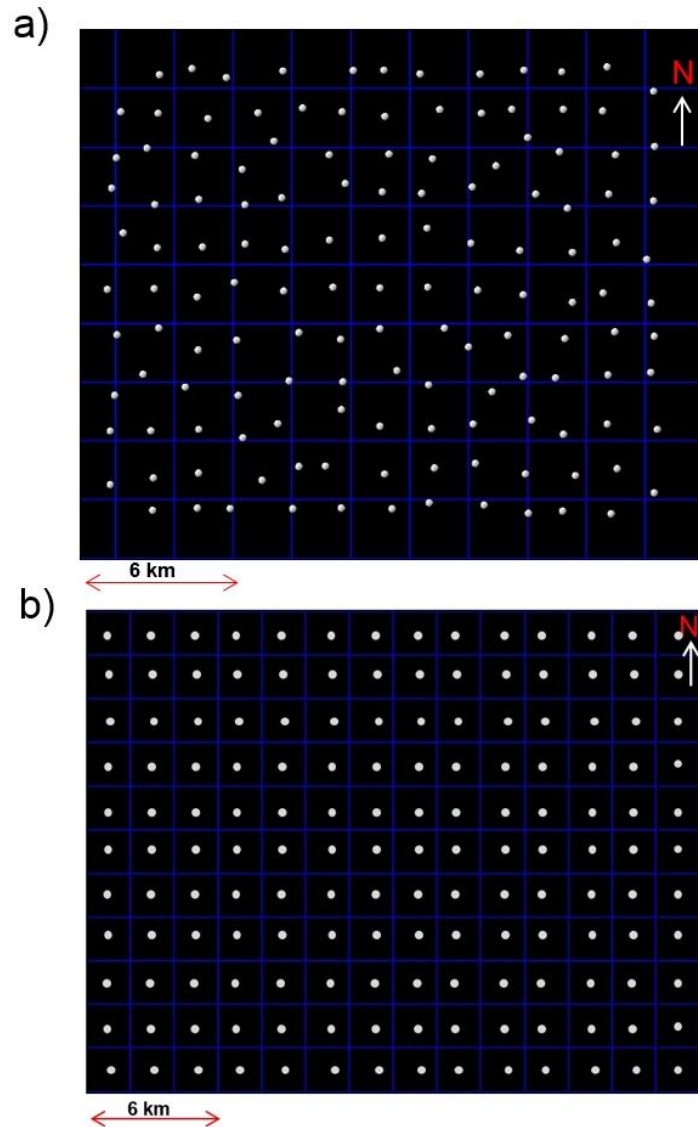


Figure 2.2. Comparison of coil center distributions where white-colored circles represent the coil centers. (a) Pseudorandom coil center grid (139 in total). (b) Regular coil center grid (144 in total).

In order to obtain the random distribution of coil centers, a randomization script was used. First, the survey area was divided into equal sized square grids. Then the following parameters were used to place the coil centers:

- (1) Total number of 139 coil centers.
- (2) A grid should contain at least a single coil center but it cannot contain more than three coil centers.
- (3) When the vessels completed the one full coil, they rolled in X direction with a minimum distance of  $dx$  and maximum distance of  $2dx$ , and in the Y direction with a minimum distance of  $dy$  and maximum distance of  $2dy$ .

### 2.3.2 Wide-azimuth design (WAZ)

Wide-azimuth towed-streamer acquisition was acquired with an antiparallel geometry using multiple vessels. The acquisition design consisted of a four-vessel configuration – two multi-streamer (8.2 km long), single-source array and two additional source vessels (Figure 2.3). The shot sequence was completed sequentially, alternating between source vessel #1 (receiver vessel #1), source vessel #2, source vessel #3 and source vessel #4 (receiver vessel #2), and each vessel generated a shot that was recorded in two spreads. The acquisition path follows a straight line then turns a  $180^\circ$  to acquire data in the opposite direction. The acquisition parameters were as follows:

- Number of sources: 4
- Streamers per receiver vessel: 10
- Streamer separation: 115 m
- Streamer length: 8.2 km
- Receiver spacing: 25 m
- Sail line interval: 1 km
- Shot interval for individual source: 100 m

One drawback of multi-vessel WAZ acquisition was the limitation of the offsets. Even though obtaining ultra-long offsets (via streamers that are 10 km or longer) were a viable option, it would make a WAZ acquisition very expensive. In an attempt to keep the costs similar for both surveys we limited the streamer length to 8 km for the WAZ survey.

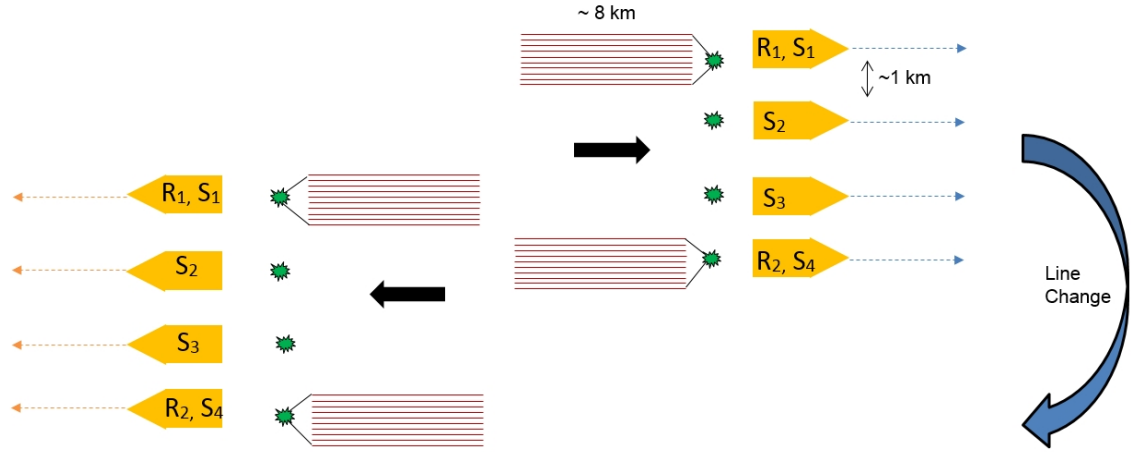


Figure 2.3. Schematic diagram of Wide-azimuth survey layout. Red line represents the streamers and green dot represents the air gun locations. Vessels are separated by approximately 1 km and each vessel marked by numbers according to the shot sequence.

### 2.3.3 Data conditioning

The designed coil survey contained more than 160,000 shots. Upon the initial analyses, ray tracing of a complete coil survey was estimated to take several weeks. To reduce the processing time, shot decimation by a factor of nine was applied in the coil survey.

In the case of WAZ survey, the total number of shots were determined as ~90,000. A shot decimation by a factor of five is also applied on the WAZ survey. This effort also facilitated equalizing the number of shots on both surveys to approximately 18,000 (Coil vs WAZ). Figure 2.4 and Figure 2.5 show the effects of shot decimation over both geometries, decreasing the number of shots reduced the ray tracing time significantly. The flip flop

nature of the shots was taken into account to assure evenly distributed shots were achieved as result of the decimation process.

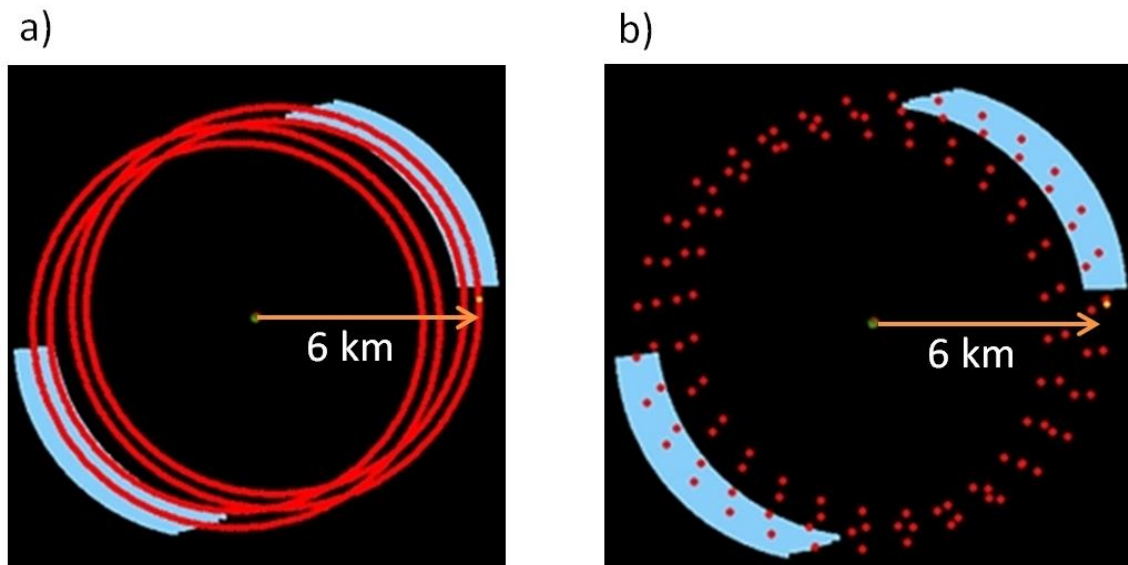


Figure 2.4. Single coil layout for the 2 x 4 configuration, red line and red dots represents the shot points and blue lines represent the streamers. (a) Before the shot decimation. (b) After the shot decimation by a factor of nine.

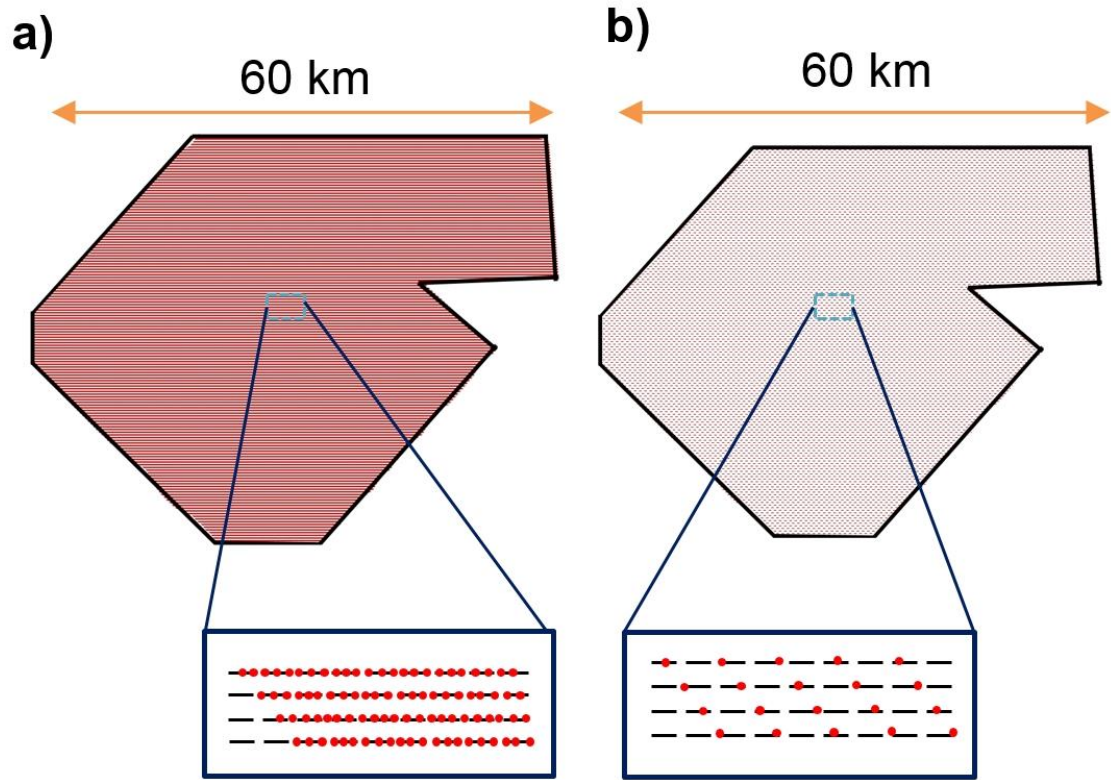


Figure 2.5. WAZ survey layout, red dots represents the shot points. Dashed gray lines represents the sail lines. (a) Before the shot decimation. (b) After the shot decimation by a factor of five.

## 2.4 Fold and azimuthal coverage comparison for a flat layer

Before proceeding to detailed illumination analyses under complex geologies for the given acquisition geometries, the survey designs were tested on a flat horizon lying at a 10.5 km depth. This initial step allowed us to conduct a fast quality control of the seismic surveys.

#### 2.4.1 Dual-coil survey

The overall shot distribution of a 2,050 km<sup>2</sup> area for the coil survey is shown in Figure 2.6. For display purposes, an individual-coil that contains four separate circles, one for each vessel, is displayed as a single coil. We observed a dense coverage of shots towards the central part of the survey.

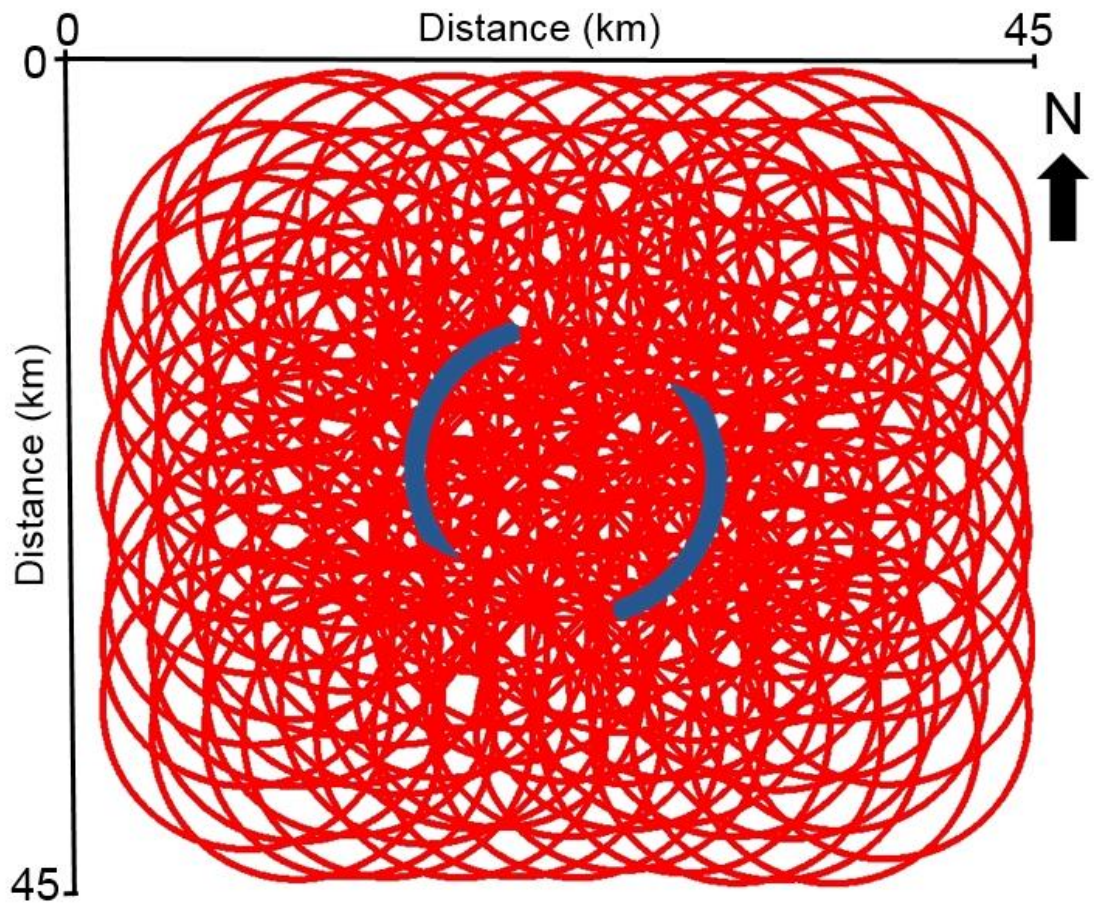


Figure 2.6. Shot distribution of a dual-coil survey for an area of 2,050 km<sup>2</sup>. Red lines represent the shot points and blue lines represent two of the receiver spreads.



Offset and azimuth distributions (rose diagram) for the entire survey area and for a small area are calculated and displayed in Figure 2.7. Overall high fold values and full-azimuthal coverage are observed for the majority of the survey. For the remainder of the coverage area, wide-azimuthal coverage (yellow and green colored bins) and some narrow-azimuthal coverage (blue colored bins) is achieved. As expected, the fold decreased towards the survey fringes. All the calculations were completed with a bin size of 25 m by 25 m.

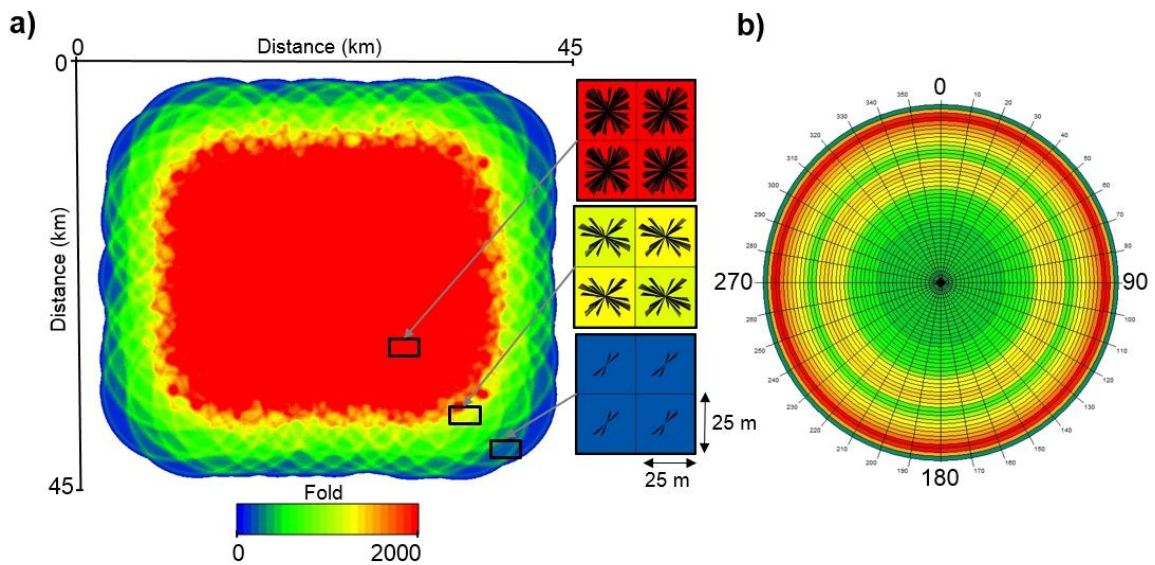


Figure 2.7. Dual-coil survey fold coverage and bin azimuth/offset distributions. Bin size is 25 m x 25 m. (a) Spider diagram indicating the azimuthal coverage for within the bin for selected areas. (b) Rose plot to show the offset and azimuth distribution (FAZ). Red color represents the higher values, cool colors represents the lower values.

As previously discussed, some studies have shown that randomizing the shot points and coil centers can help to minimize the acquisition footprint over illumination maps (Moldoveanu, 2010). If the circle center distribution is not random, we expect to see a repeating pattern on coverage fold distribution. To test this idea, we have generated fold and azimuth/offset distribution maps for the regularly distributed (as seen in Figure 2.2b) coil centers. Figure 2.8 shows that the regular coil distribution caused a repeating pattern on the fold coverage. Similar effects was also seen on the azimuth/offset distribution for the selected bins (Figure 2.8b).

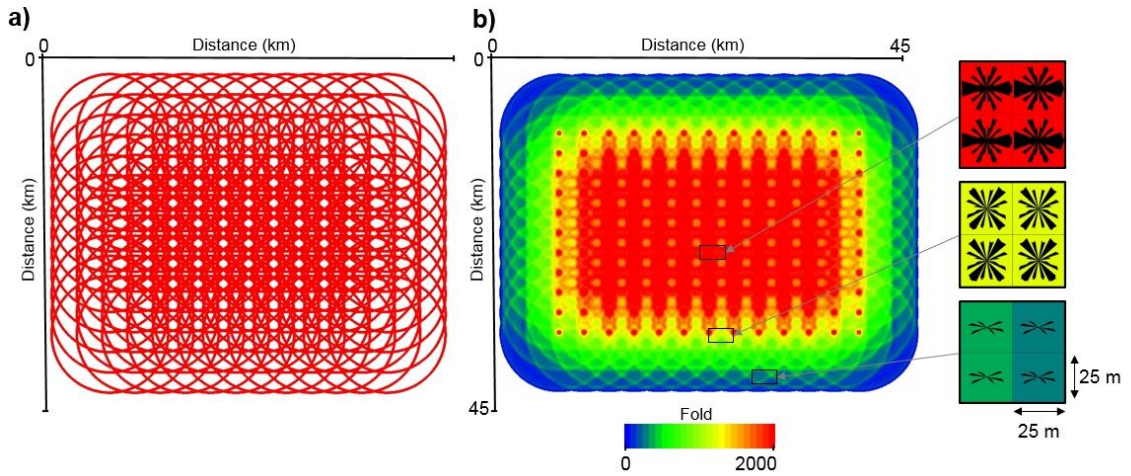


Figure 2.8. Dual-coil survey fold coverage with bin azimuth/offset distributions, obtained by regular coil distribution (144 in total). Warmer colors represents higher fold values. (a) Coil distribution over 2,000 km<sup>2</sup> area. (b) Fold coverage map with a bin size of 25 m by 25 m.

Based on the results of the dual-coil design:

- Long offsets ~ 10 km were achieved.
- High density data coverage was observed over most of the survey area, which resulted in overall high fold distribution and full-azimuthal coverage.
- Some irregularities in the fold distribution, due to acquisition geometry, were observed.

#### 2.4.2 Wide-azimuth survey

Due to straight line geometry, the WAZ surveys require careful planning of the acquisition. To optimize the turn in and out that were required for the streamer vessels, and to minimize the downtime, the shape of the survey area was revised. The overall shot distribution of a 2,400 km<sup>2</sup> area for the WAZ survey is shown in Figure 2.9.

The offset and azimuth distributions (rose diagram) for the entire survey and for a small area are calculated and displayed in Figure 2.10. All the calculations were completed with a bin size of 25 m by 25 m. Relative to the dual-coil fold coverage results, lower fold coverage with east–west extending lines, as a result of straight line geometry, resulted in acquisition footprints. The rose diagram indicated an approximate coverage of 120 degrees for the azimuth distribution.

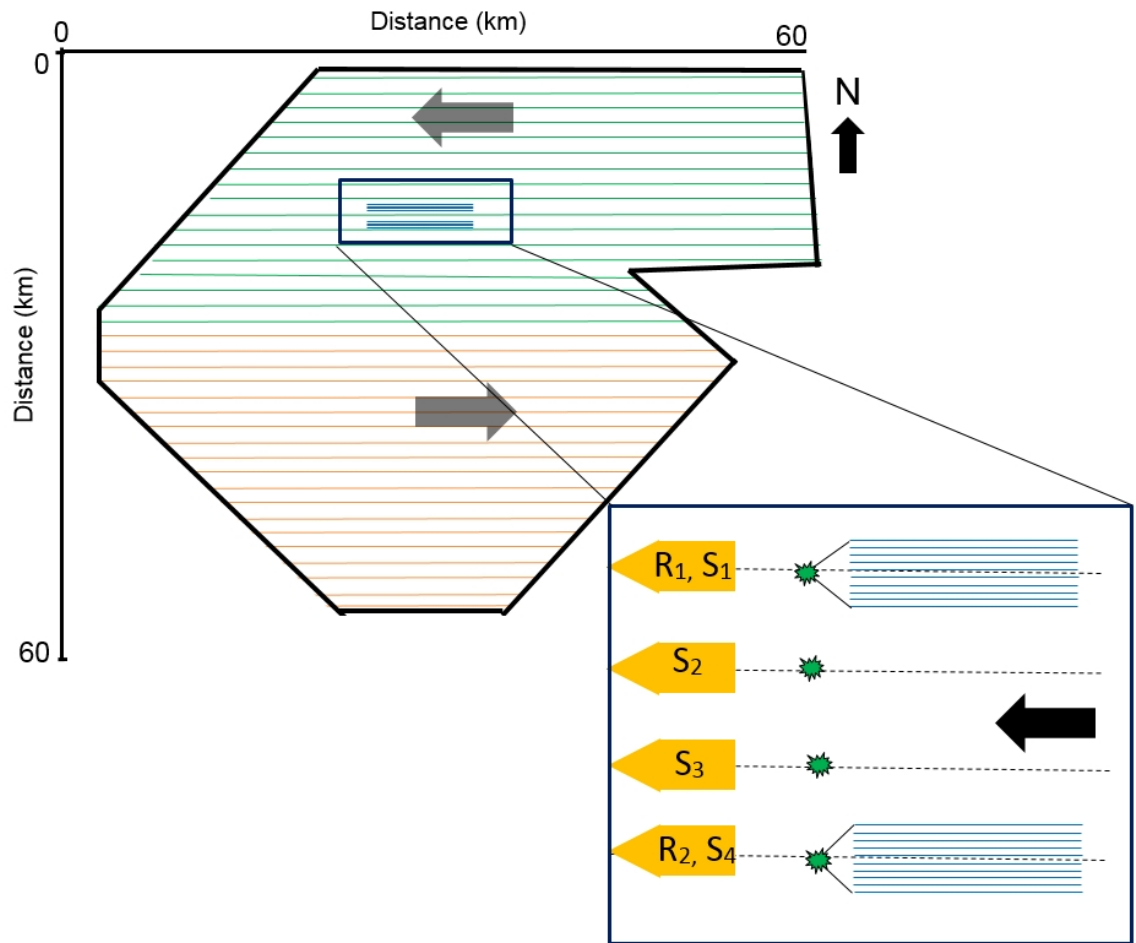


Figure 2.9. Shot distribution of WAZ survey for an area of 2,400 km<sup>2</sup>. Green and orange lines represents the shot points and blue lines represent the two receiver spreads.

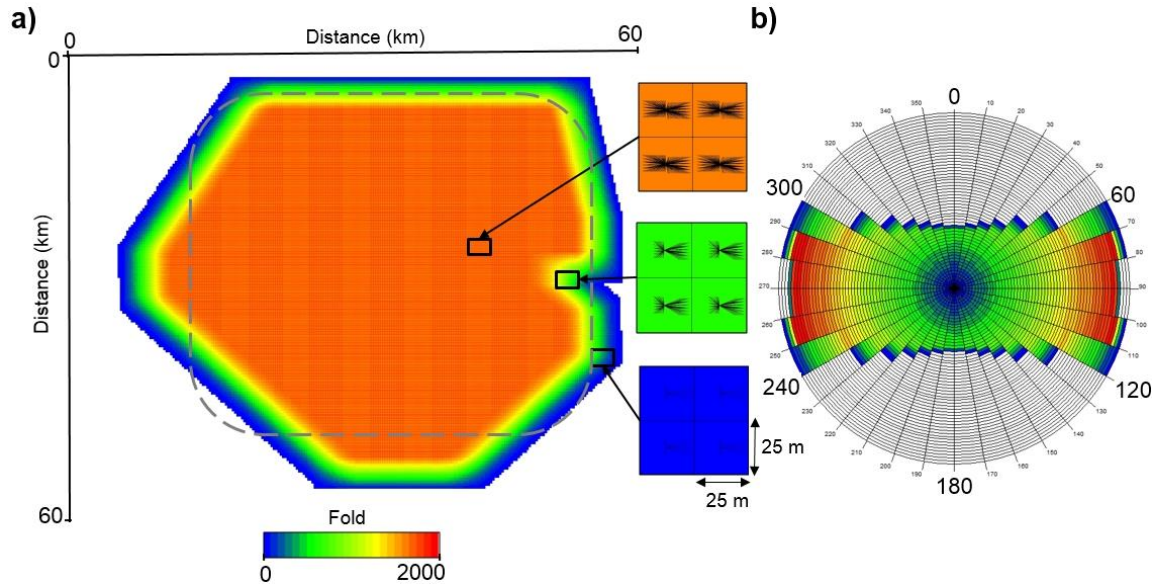


Figure 2.10. The WAZ survey fold coverage and bin azimuth/offset distributions overlain with the dual-coil survey extensions (gray dashed line). Bin size is 25 m x 25 m. (a) Spider diagram indicating the azimuthal coverage for within the bin for selected areas. (b) Rose plot to show the offset and azimuth distribution (wide-azimuth) for the entire survey. Red color represents the higher values and cool colors represent the lower values.

### 2.4.3 Dual-coil vs WAZ geometry results

Dual-coil design provided approximately twice as many shots, in comparison with the WAZ design. Even though the shot numbers were balanced by the shot decimation, the coil survey delivered better subsurface coverage. The summaries are as follows:

- (1) The acquisition time for a dual-coil survey at this scale should take approximately 60 to 65 days. In case of the WAZ survey, the acquisition time was estimated as 90 to 100 days.
- (2) Dual-coil design provided FAZ data at the central part, which covers ~ 65 % of the total survey area, the remaining parts of the survey contained mostly wide-azimuthal coverage.
- (3) The WAZ survey provided coverage on a slightly bigger area due to the geometry requirements of straight vessel sail lines. Eighty percent of the survey contained wide-azimuthal coverage and the rest of the survey contained narrow azimuth data.
- (4) Dual-coil geometry provided higher fold coverage whereas the WAZ results provided lesser fold on a bigger area.
- (5) Dual-coil design yielded some minor irregularities in the fold distribution whereas the WAZ survey contained east-west acquisition footprints due to the straight-line geometry.

## 2.5 Illumination comparison of dual-coil and WAZ geometry for a subsalt prospect

In this section, we will compare the two geometries in terms of their illumination quality for a subsalt horizon. These calculations were completed over a subsurface geological model that was generated by using the existing seismic data in the northern Gulf of Mexico with an average 1.5 km of water depth.

### 2.5.1 Subsurface geological model

The subsurface geology model was obtained using pre-existing surveys over the northern Gulf of Mexico (Moldoveanu and Kapoor, 2009). The model was populated using Petrel software and it contained six layers: water, water bottom, salt body and three subsalt sedimentary horizons. Appropriate velocity and density for each layer was provided by available well logs and velocity analyses from existing studies (Moldoveanu and Kapoor, 2009; Brice, 2011). The resultant P-wave seismic velocity cross section is shown in Figure 2.11. To reduce calculation times, constant seismic velocities for the water layer and salt body were used (1.5 km/s and 4.5 km/s respectively). The extensive salt body (highlighted with a red color) with high P-wave velocities is also shown in Figure 2.11.

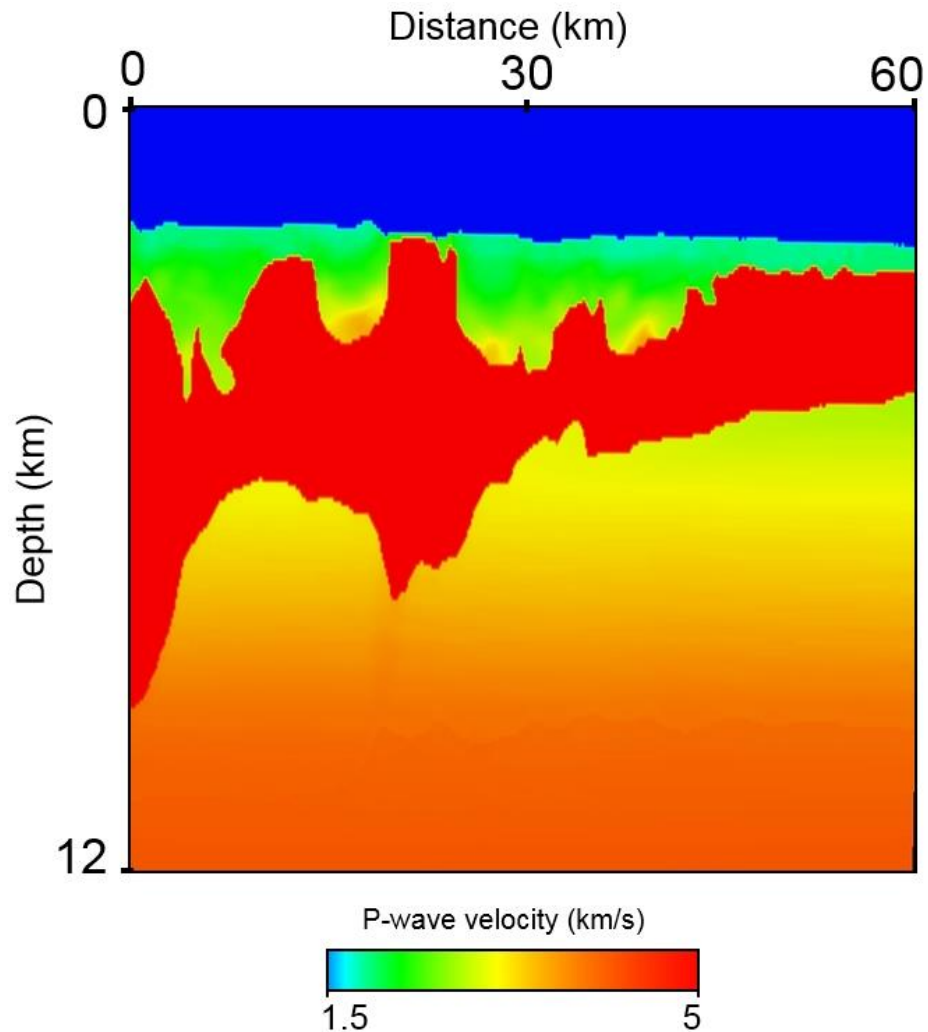


Figure 2.11. Subsurface geological model with P-wave seismic velocities, in-line view. The red color represents higher P-wave velocities, cooler colors represents lower P-wave velocities. An extensive salt body with high P-wave velocities is shown.

The deepest subsalt horizon in the model was selected for further illumination analyses (Figure 2.12). Figure 2.12b shows the horizon of interest that contains two adjacent anomalous structures, which covers approximately 145 km<sup>2</sup> of area, most of the illumination analyses were focused over this particular area.



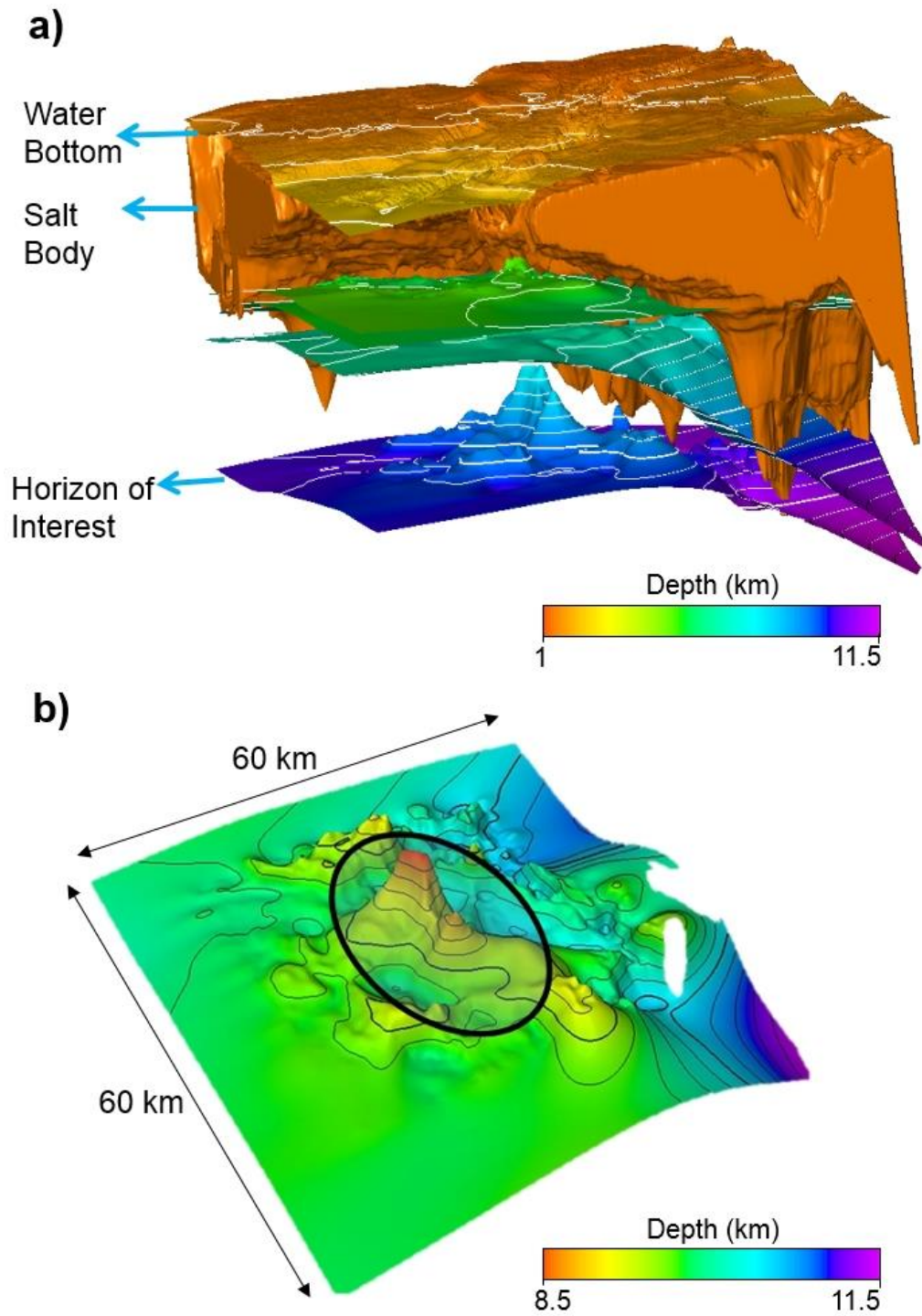


Figure 2.12. Closer view of the subsurface geological model with the horizon of interest. (a) Layers are colored by their depth (except for the salt body). (b) The target area over the horizon of interest and anomalous structures highlighted by a black colored circle.

### 2.5.2 3D ray tracing illumination results

The initial fold and azimuth/offset coverage analyses that were completed over a flat horizon indicated a better geophysical illumination is to be expected from a coil survey when compared to the WAZ survey.

3D ray tracing helped us to evaluate the illumination at the target level using a complex geological model. Target illumination was evaluated using different attributes map. We were mainly interested with hit count maps, as they can easily illustrate the differences in terms of illumination quality. Figure 2.13 shows the calculated hit count maps for dual-coil and WAZ surveys.

The hit count map (Figure 2.13b and 2.13d) for the WAZ geometry shows that most of the steep portions of the target reservoir were not illuminated. The coil survey provided a better coverage (Figure 2.13a and 2.13c) with less illumination holes, whereas the WAZ survey contained illumination holes over the target horizon. It was indicated from the 3D ray tracing studies that full-azimuth and long offsets were required to illuminate such a target.

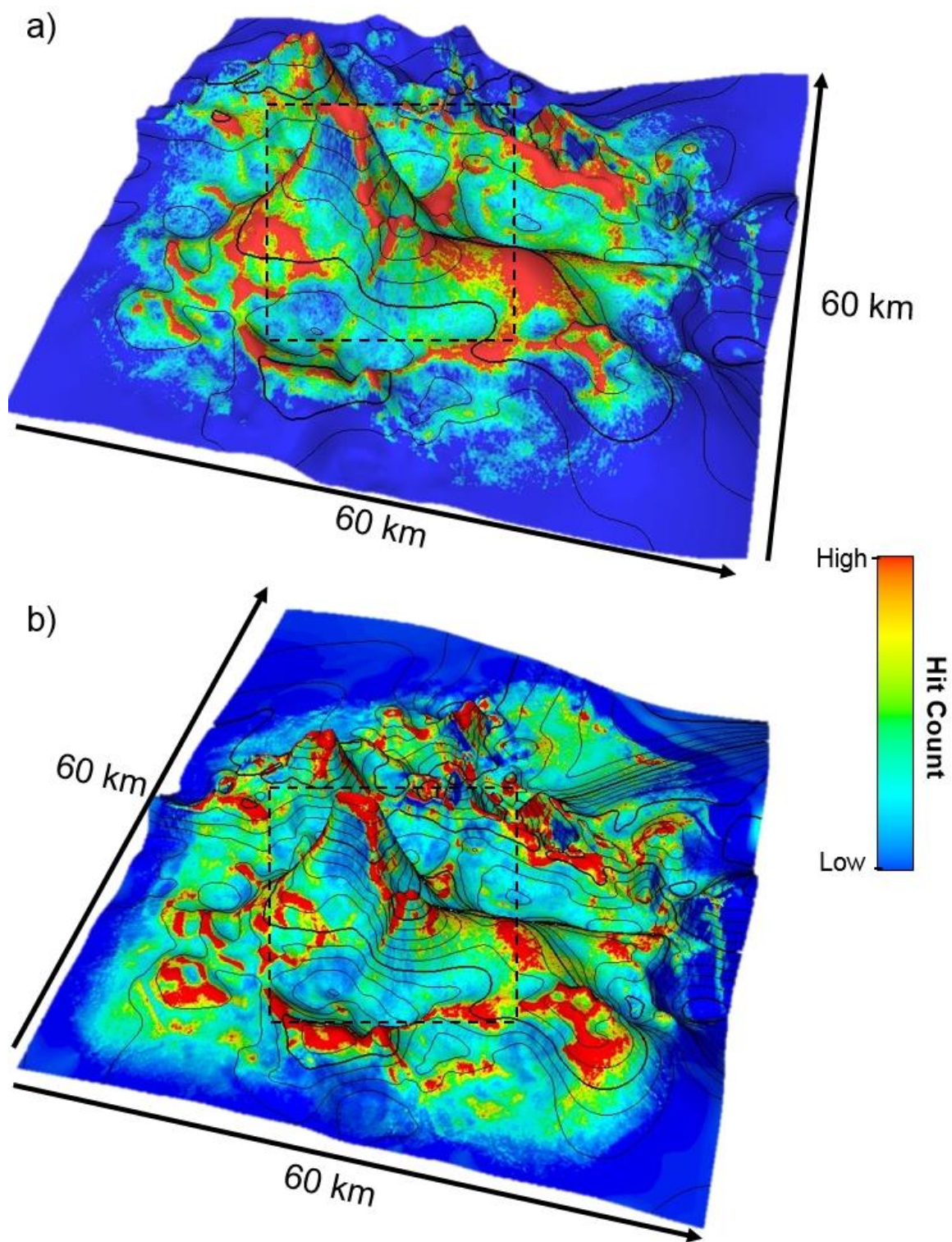
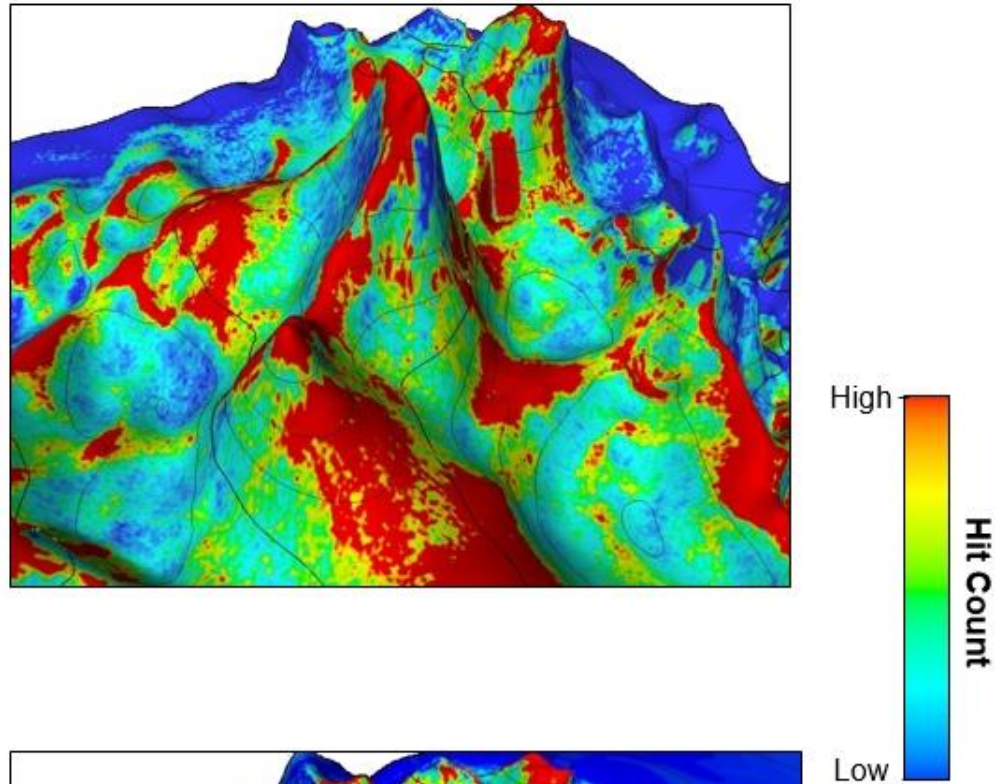


Figure 2.13.



c)



d)

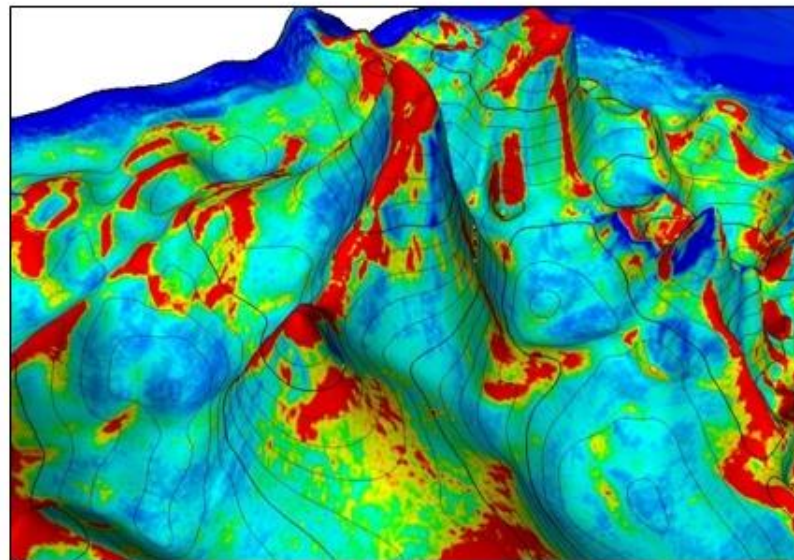


Figure 2.13. cont. Comparison of illumination maps for a subsalt horizon by 3D ray tracing analyses and a closer view of a target area (black dashed box, 145 km<sup>2</sup>) for the dual-coil survey (a and c), and the WAZ survey (b and d). Warm colors represent higher hit counts (denser illumination), cooler colors represent lower hit counts (sparse coverage and lower illumination density).

## 2.6 Survey optimization

Survey design optimization quantifies and maximizes the forecasted information in data; it can optimally maximize model-parameter resolution for imaging purposes (Moldoveanu et al., 2013; Coles, et al., 2014).

The optimal survey design algorithm finds the measurements that are likely to increase the illumination intensity over the selected target area. This method can also be useful in planning the acquisition or data processing, by prioritizing the shots that would have the maximum contribution for the selected target area. This analysis was performed over the selected area within the horizon of interest. A fairly large target area was selected for further analysis, 16 km by 9.5 km (red colored area in Figure 2.14).

In simplified terms, the illumination factor is proportional to the distribution of the attributes (i.e., hit counts, amplitude, azimuthal coverage, frequency, etc.), as a result of ray tracing over the target area. If the illumination intensity is high over certain points of the target, the illumination factor would be high (and vice versa). At first, we have assigned the illumination factor to the lowest possible value, zero (0), for the selected target area. This illumination factor was then increased by the introduction of ray tracing results from each subset (individual-coils for Coil survey, sail lines for WAZ survey) of the geometry. The highest possible value for the illumination factor was set as one (1). By doing so, the contribution from each subset data was quantified. The overall change in the illumination

factor can also be used to evaluate the illumination intensity of the different types of geometries.

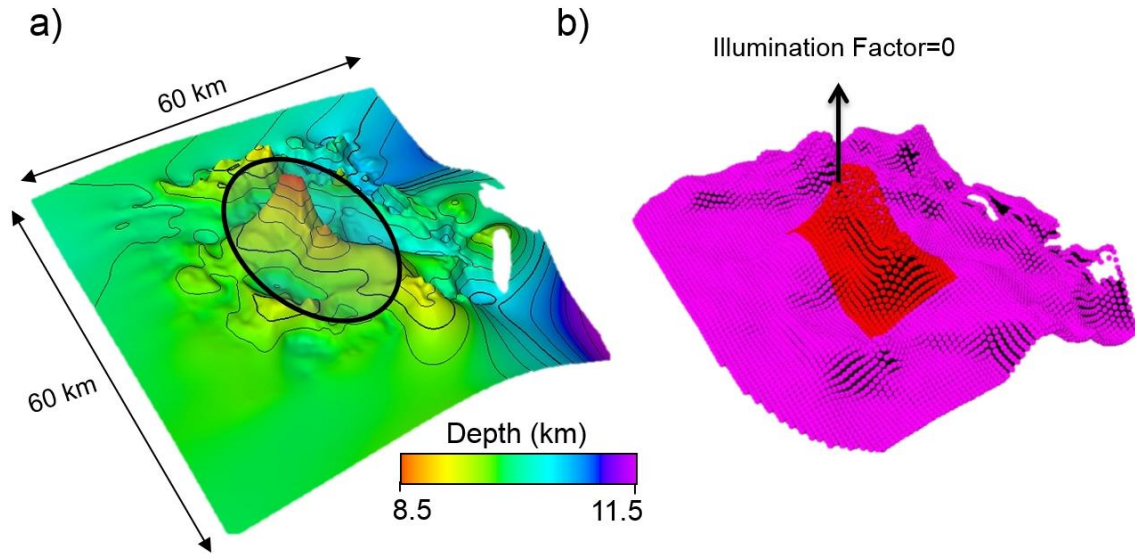


Figure 2.14. (a) Closer view of the horizon of interest, colored by the depth (warm colors represent shallower depths). (b) The associated illumination factor distribution. The illumination factor is up scaled by 10,000 during the calculations.

The data required to conduct optimized survey design were:

1. Ray tracing results from survey geometries, dual-coil and WAZ in this instance, over a horizon of interest.
2. Illumination factor associated with the reflection points over the target area at the horizon of interest.

The results of the analyses provided critical information:

1. After the introduction of all subset data for each geometry, the final illumination factor value over the target area can be compared to provide quantitative resolution analyses.
2. Prioritized contribution of subset data (individual-coil vs sail lines): This would help to identify the most and least contributing coils for coil survey, and also the most and least contributing sail lines for WAZ survey.

The coil survey acquired by overlapping 139 individual-coils (each coil carries four separate circles on which the vessels sail along). The WAZ survey was divided into 22 subset files (sail lines) that contained almost the same number of shots.

Figure 2.15 shows the most contributing coils and sail lines. For display purposes, coil centers are displayed rather than the full geometry. Figures 2.15c and 2.15d plots the change of illumination factor after the addition of each coil and the sail line. The total amount of change in the illumination factor enabled us to quantify the illumination intensity for both Coil and WAZ surveys for the selected target area.

In the case of dual-coil geometry, the assigned illumination factor had minimal change for almost 80 coils and increased by 85 % with the remaining 60 coils. In the case of the WAZ geometry, the illumination factor was greatly increased by 10 sail lines, but never scored

higher than 0.8 (approximately 20 % less than the dual-coil survey). Which indicates that certain portions of the selected target area will remain unresolved. These results agreed with our initial findings with the 3D ray tracing results that the WAZ survey resulted in illumination holes over the target area.

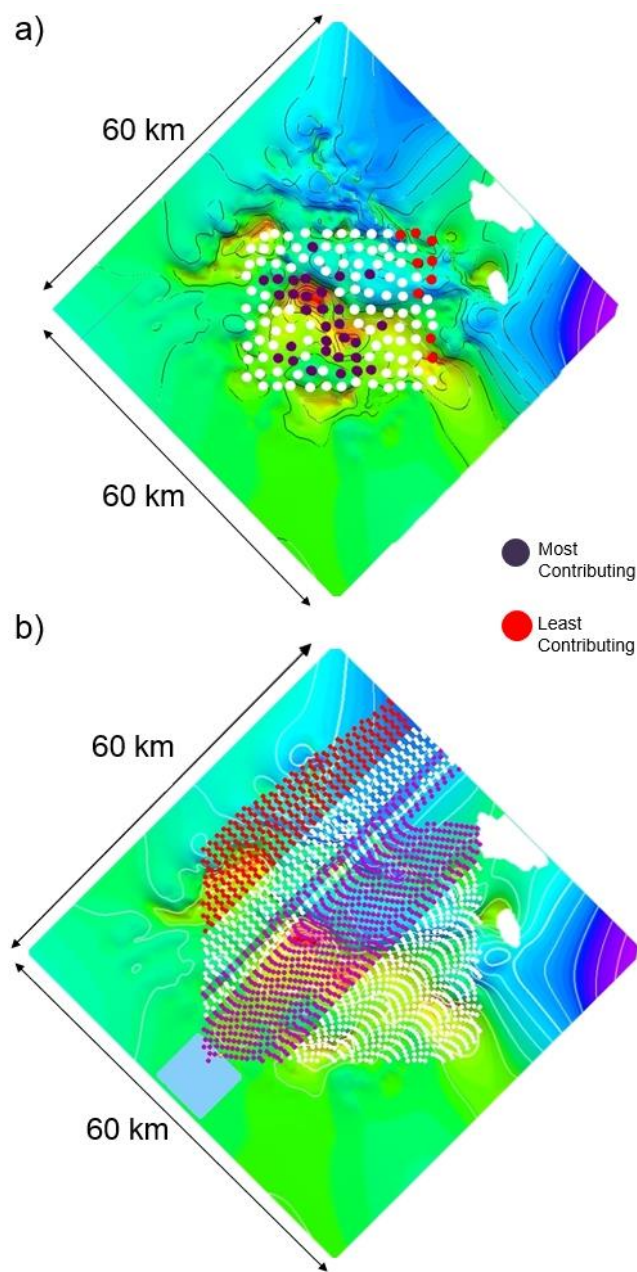


Figure 2.15.



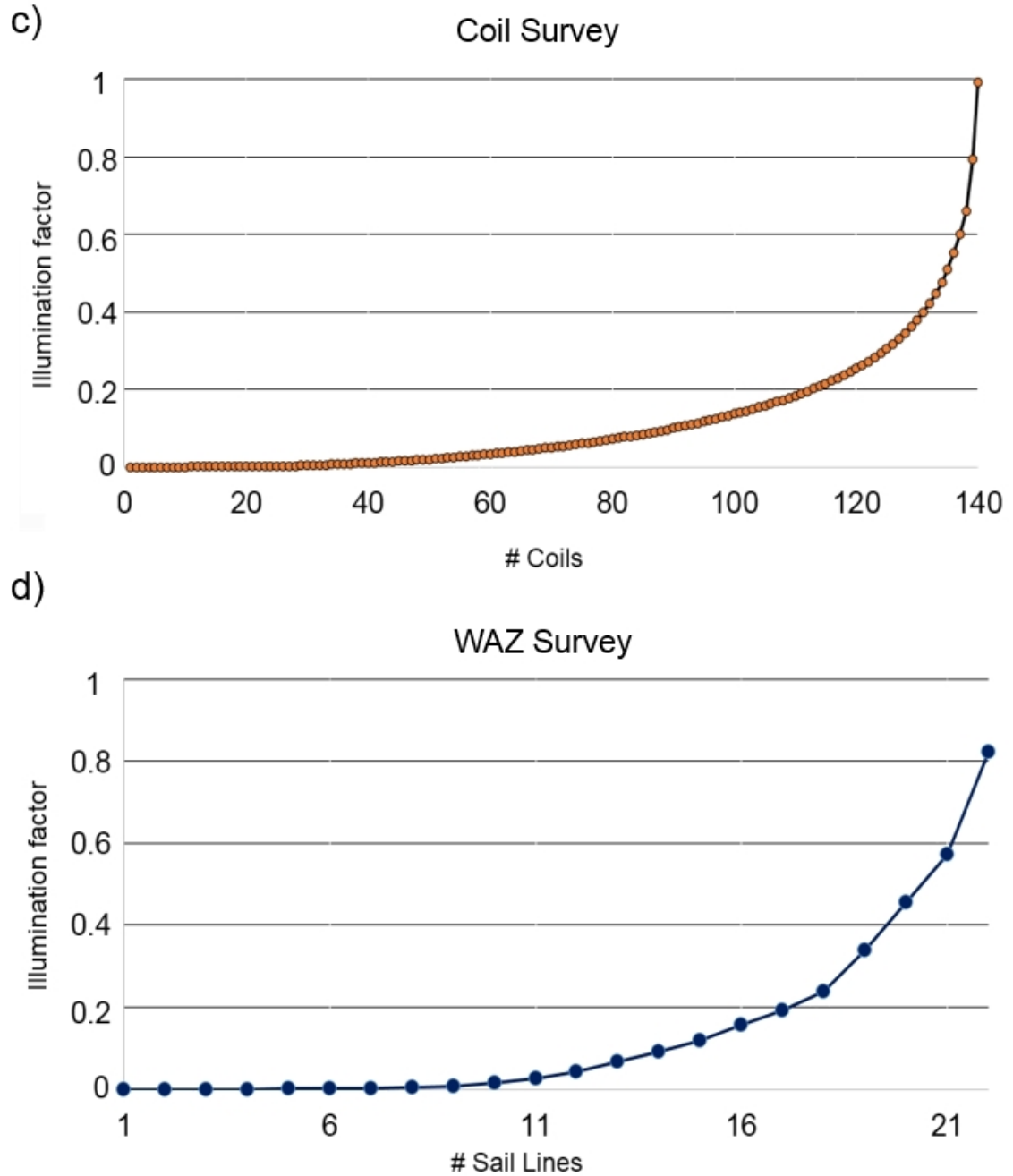


Figure 2.15.cont. Survey design optimization results for dual-coil geometry (a and c) and WAZ geometry (b and d). Purple colored circles and lines represent the most contributing coils and sail lines. Red colored circles and lines represent the least contributing coils and sail lines. Relative to the Coil survey, the WAZ geometry had 20 % less illumination intensity.

## 2.7 The wave-equation illumination

Both the coverage analyses over flat layer and the 3D ray-based illumination studies over the subsalt layer have shown the advantages of the dual-coil geometry over the WAZ survey. The last step was to conduct a target-oriented wave illumination study for dual-coil geometry over the horizon of interest. The wave-equation illumination results were then compared with 3D ray-based illumination studies.

Conventionally, an illumination study for seismic survey design involves ray-based methods, and although they are capable of capturing properties of simpler earth models, they can suffer accuracy in more complex regions. In the case of the Gulf of Mexico, due to the presence of multiple complexities (ultra-deep water, horizontally extending thick salt bodies, and rapid change of velocities, etc.), we introduced a target-oriented wave-equation illumination method (Lapilli et al., 2010). This method provided target-oriented illumination studies where wave propagation accurately models the wave field properties, and target-oriented illumination maps were constructed through the synthetic data. The target-oriented method presents a reduced modeling cost when compared to an illumination study where given acquisition geometries are fully modeled and migrated to obtain the imaged amplitudes at a selected target (Lapilli et al., 2010). The processing steps were completed mainly in the Omega software and the mapping stage was completed using the Petrel software.

The key component of this method was to place the shot points on the desired target area within the horizon of interest and propagate the shots to the surface grid. This propagation was one-way (from subsurface to surface); therefore the processing time and modeling cost was significantly reduced. Using the reciprocity of the propagation, energy maps were generated over the source grid to determine the reflection point energy (horizon amplitude maps). By filtering out the acquisition geometry, surface energy maps were also created. Therefore this method can be used to calculate shot weights describing the contribution of energy for imaging a given target.

Some of the key points related with the wave-equation illumination:

- It uses one-way (target horizon to surface) finite difference to perform two-way wave-equation illumination analysis.
- It allows for target horizon and surface amplitude maps to be filtered by acquisition geometry.
- Series of illumination maps can be generated at the reservoir level or the surface.
- It can be used to generate shot weights for a given geometry (Dual-coil geometry in this instance).

Figure 2.16 shows the preparation step for source and receiver layout. The receivers at the surface were placed with 50 m spacing in a 145 km<sup>2</sup> area, this selection of the target area was solely based on the prospect dimensions. Approximately 4,000 shot points with 100 m

spacing were placed over the target area; this selection was based on efforts to optimize the processing time. These shots were then propagated through the geological model to the almost square shaped surface receiver grid. Once the propagation was completed, both the energy distribution of the shots that were placed over the target area and the energy distribution of the receivers that were placed at the surface were obtained.

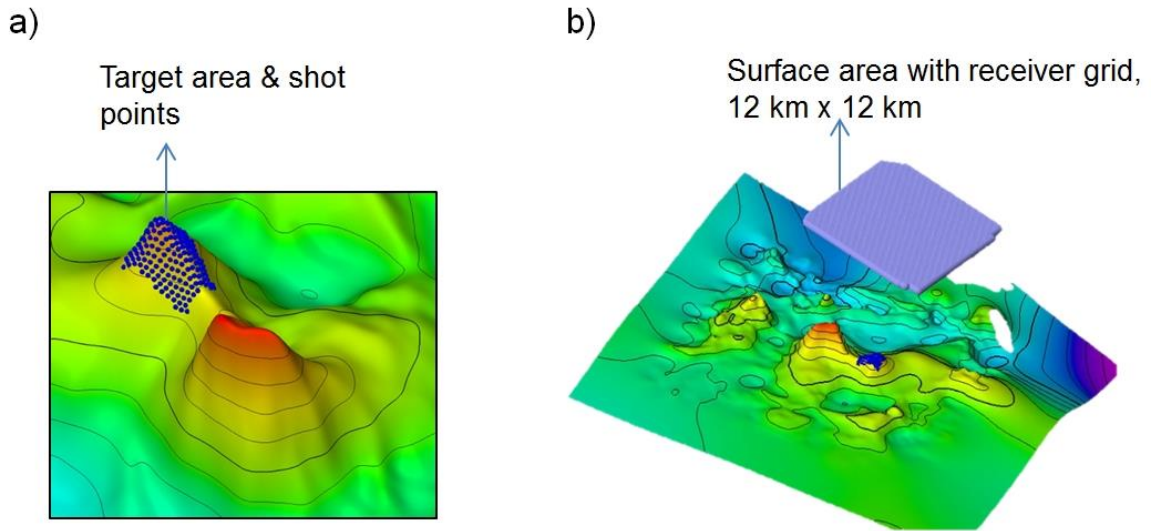


Figure 2.16. The distribution of source and receiver grid with selected target area over subsalt horizon. The subsurface model is colored by the depth (warm colors represent shallower depths). (a) Actual shot points over the target area. (b) Receiver grid at the surface.

### 2.7.1 Wave-equation illumination results

A wave-equation-based method was used for seismic illumination analyses. The illumination results obtained from this method enabled us to further optimize the survey design using more accurate subsurface physical-parameter retrieval.

3D ray tracing studies are still used as the primary evaluation method for the survey design studies. The ray tracing method is practical and economical however the results can be questionable for complex geologies. Wave-equation methods account for the complexity of the wave field. This method reduced the processing cost and time drastically by modeling only 4,000 shots.

Figure 2.17 compares the results obtained from ray tracing studies with the amplitude map from the wave-equation illumination studies. A certain correlation was found between two different studies where the low energy zones matches with the low hit counts; however the distribution of the high energies showed some significant differences over the target area.

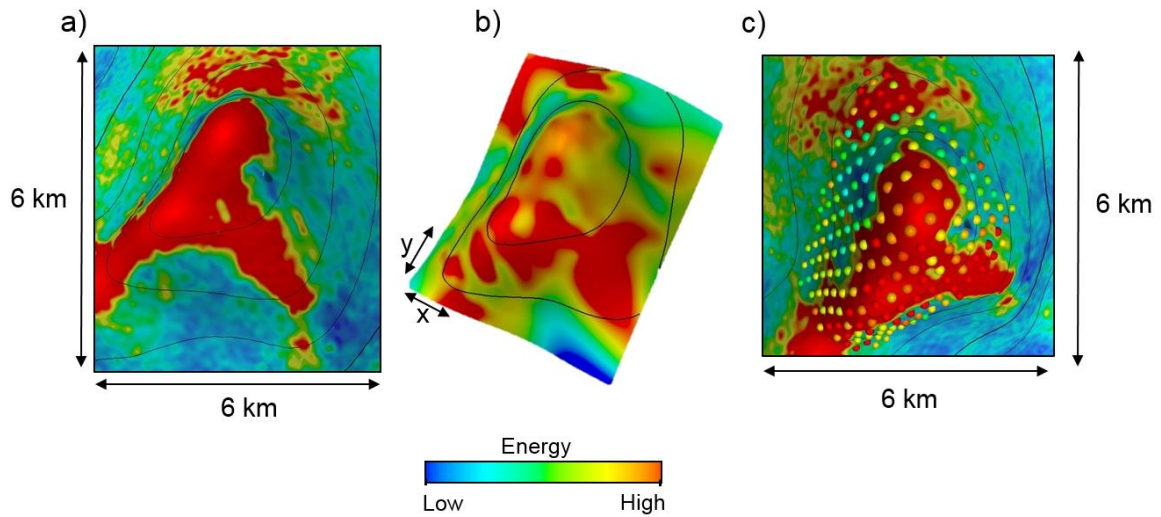


Figure 2.17. Target horizon and calculated illumination energy comparison. (a) The color map on the horizon represents the hit count distribution obtained from 3D ray-tracing studies. (b) The color map on the horizon represents the illumination amplitude obtained from wave-equation illumination (surface area map was obtained by interpolation). (c) Illumination amplitude obtained from wave-equation (circles) illumination overlain on top of the hit counts obtained from ray tracing studies.

We also observed that the amplitude distribution over the target area obtained from wave-equation to be in good agreement with the amplitudes obtained from the migration of the existing data (not shown here). The agreement in the amplitude maps, can open more possibilities for future applications of this method such as: AVO (amplitude versus offset) and AVA (amplitude versus angle).

Surface energy maps for the corresponding coil geometry are displayed in Figure 2.18. Warm colored areas represent the highest energy locations which should correspond to the most contributing shots for the illumination of the selected target area. For display purposes, only the energy distributions along the two most contributing coils are shown.

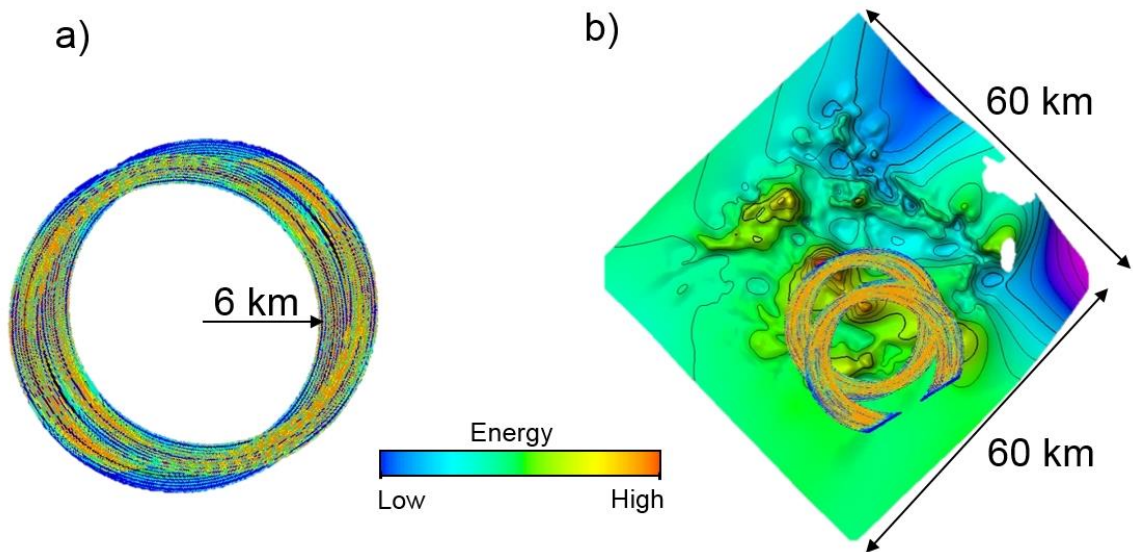


Figure 2.18. (a) Energy distribution maps for the shot points at the most contributing coil. The warm colors represent the higher energies which corresponds to the most contributing shots on each coil (b) Energy distribution for two most contributing coils, overlain with the horizon of interest colored by the depth (warm colors represent shallower depths).

## 2.8 Ray-based method versus the wave-equation-based method

Our detailed analyses for the illumination over the subsalt horizon for the ray-based and wave-equation-based methods indicated:

- Conventional ray-based studies can deliver efficient results for subsurface illumination, but one should always keep in mind the limitations of this method.
- The survey design optimization method can deliver useful results to further optimize the survey for the needs. This method also quantifies the success of the geometries in terms of the illumination of a selected target area.
- Wave-equation based method can provide more accurate illumination results for subsurface illumination. Compared to the existing finite difference alternatives, the wave-equation illumination cuts the processing time and cost significantly. This method also delivers a valuable information for the shot weights as surface maps.
- Wave-equation-based method results are heavily dependent on the accuracy of the subsurface model. This may not be a problem for areas where the various existing seismic data that compliments the subsurface models (such as Gulf of Mexico); however, it can be a potential problem for relatively new exploration areas.

Therefore, we conclude that the wave-equation illumination method provides a flexible and efficient tool to calculate target-oriented or volumetric illuminations for complex models.

## 2.9 Conclusions

This work presents an illumination and survey design comparison using dual-coil and WAZ marine acquisition geometry. The initial analyses were completed over flat horizon at 10.5 km depth and the dual-coil geometry provided higher fold distribution with full-azimuthal coverage. The WAZ survey provided coverage on a slightly bigger area due to the geometry requirements of straight vessel sail lines. In terms of the acquisition time, dual-coil geometry potentially reduced the time by 40 % when compared to the WAZ geometry. The illumination comparisons were completed with 3D ray tracing. Hit count maps showed the advantages of the coil geometry for the illumination of the subsalt horizon, the WAZ survey results included illumination holes that would result in poorly resolved images. A fairly new method, the survey optimization method was used to extract the contribution information. The most and the least contributing coils and sail lines were determined. This method also quantified the illumination success of the two geometries using the illumination factor. The WAZ survey resulted in lower illumination factor (lower intensity) for a target zone illumination, agreeing with the results from the 3D ray tracing study. Dual-coil survey was selected for further investigation by wave-based method, as the coil geometry provided better target illumination based on 3D ray-based studies. The wave-based illumination analysis technique had the advantage of properly accounting for the wave nature of the propagated field in complex geological settings. The modeling



necessary for the wave-equation illumination method involved only 4,000 modeled shots, this was a significant reduction in time and cost due to target-oriented nature of the wave-based methods. Illumination amplitudes from the wave-based methods were also compared with amplitude maps from existing studies and showed good correlation. This method also generated surface maps over 145 km<sup>2</sup> area to show the shot weights for the dual-coil geometry, which indicated both the most contributing coils and most contributing individual shot locations within each coil for the illumination of the selected subsalt target. This method can also be helpful in planning the acquisition or data processing, by prioritizing the shots that would have the maximum contribution for the target area.

## 2.10 Future Considerations

### 2.10.1 Ellipse design

An alternative survey design with ellipse geometry may complement the advantages of both the WAZ and dual-coil geometry. To our knowledge, there has been no commercial seismic marine survey containing ellipse geometry. Most of the marine surveys may not favor an ellipse design; however, this geometry may provide a direct benefit for certain conditions, such as:

- Survey design cases that require further far offset coverage.
- Limited survey area that prohibits:
  - WAZ design due to extra space requirement for line changes.
  - Coil design due to potential obstacles.

We designed an ellipse geometry to observe the effects over the fold and azimuth/offset distributions. In principle, the ellipse design should yield results between coil geometry and WAZ geometry. We attempted to keep most of the acquisition parameters similar to the dual-coil design. The acquisition parameters were as follows:

- Number of sources: 4
- Number of streamers per vessel: 10
- Streamer separation: 120 m
- Streamer length: 10 km
- Receiver spacing: 25 m
- Shot interval for individual source: 100 m
- Axis length: 7 km and 5 km

The selection of the axis length was based on the effort to keep the circumference for the ellipse geometry approximately the same as the dual-coil geometry. The circumference for both the dual-coil design and the ellipse design was ~37.9 km for a single circle or ellipse.

We completed analyses over a test survey which included three main ellipses (each included four ellipses for the vessels to sail separately). In the ellipse geometry, similar to the dual-coil acquisition, there were two receiver vessels and two source vessels. Each receiver vessel also included a single source array. Therefore, a total number of four gun arrays were used, hence called a 2 x 4 configuration. The shot sequence was completed sequentially, alternating between S1, S3, S2, and S4 with each vessel generating a shot that was recorded in two spreads. A layout for ellipse geometry is featured in Figure 2.19.

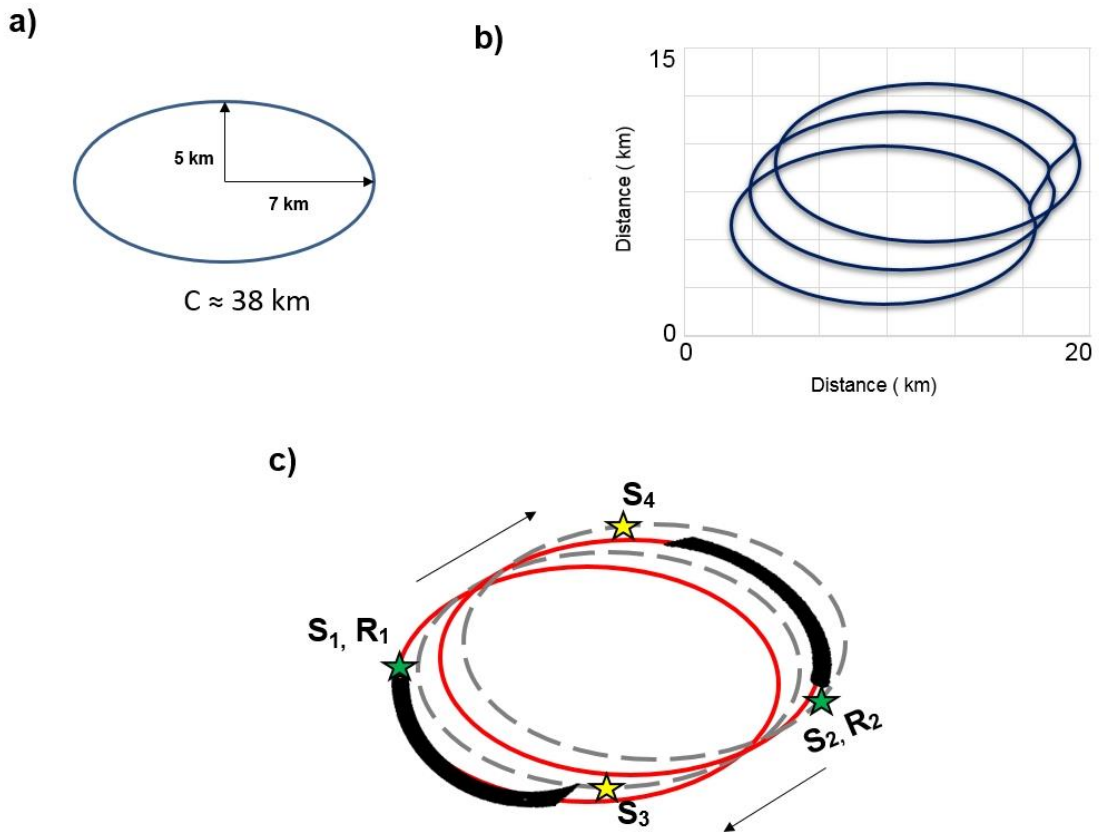


Figure 2.19. Ellipse geometry layout. (a) An ellipse with the dimensions of the axes. (b) Three adjacent ellipses used for the further analyses. (c) Vessel layout for the ellipse geometry. The red line represents the sail lines for the receiver vessels; the dashed grey line represents sail lines for the shot vessels. The shot sequence for the vessels are S1-S3-S2-S4. The long offsets were produced by sources shooting across the ellipses. Each vessel sails along a separate ellipse, these ellipse centers were offset in X direction by dx (1,000 m) and in Y direction by dy (1,500 m).

The ellipse design provided azimuthal coverage somewhere between wide-azimuth and full-azimuth; it appears to carry minor irregular distribution of the traces (Figure 2.20). The azimuthal coverage is dominant in the longer elongation axis. Overall high fold coverage

was observed for most of the survey and specifically for the far offsets. All the calculations were completed with a bin size of 25 m by 25 m.

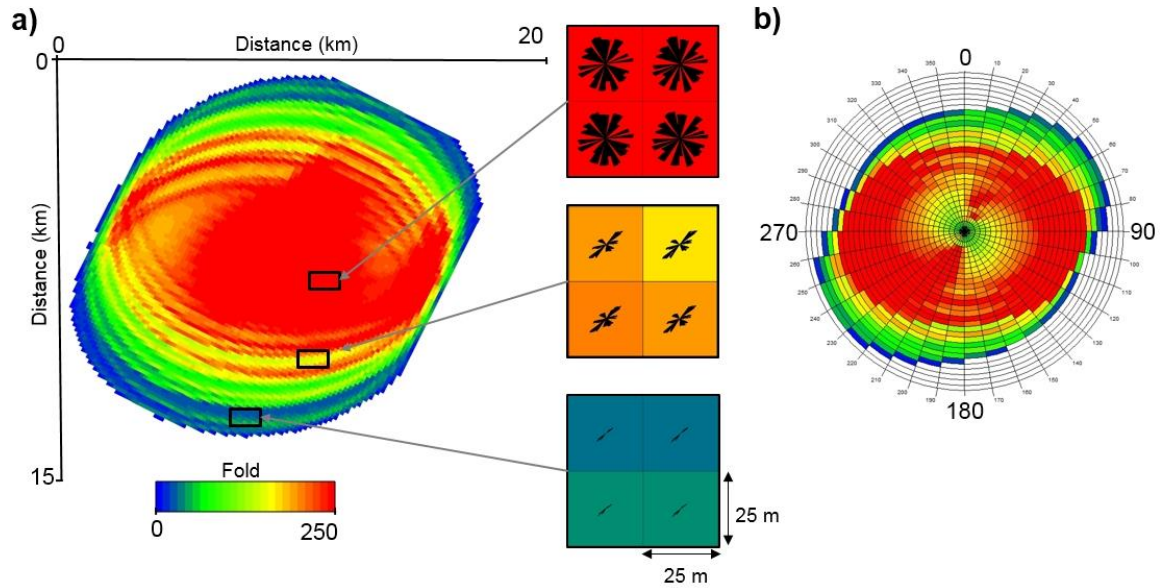


Figure 2.20. The coverage fold and bin azimuth/offset distributions for ellipse geometry. Bin size is 25 m x 25 m. (a) Spider diagram indicating the azimuthal coverage for within the bin for the selected areas. (b) Rose plot to show the azimuth/offset distribution for the entire survey. Red colors represent the higher data values, cool colors represent the lower data values.

Another potential benefit of the ellipse geometry was reduced acquisition time. Figure 2.21 compares the designed ellipse geometry with the required dual-coil geometry to cover the same area. In the case of ellipse geometry three ellipses were required; however, for the same coverage four circles would be needed for the dual-coil design.

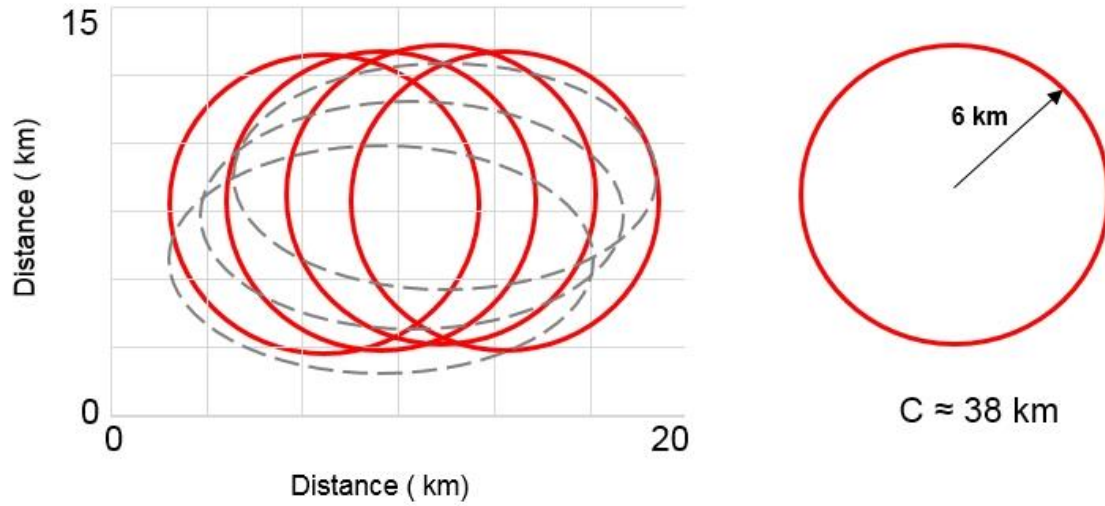


Figure 2.21. Comparison of a proposed dual-coil and ellipse geometry for the test survey. Circumference of both the coil and the ellipse geometry are fixed to the  $\sim 38$  km. Red lines represent the sail lines for the dual-coil design; the dashed gray lines represent sail lines for the ellipse design. Four circles are needed to cover the test survey area whereas three ellipses would be enough for such a survey.

To directly compare results from both geometries, we also completed fold, offset and azimuth analyses over the proposed dual-coil design (Figure 2.22). The full-azimuthal coverages were seen for both geometries at the central parts of the survey. For the remaining parts of the survey area dual-coil design mostly included wide-azimuthal coverage whereas the ellipse design contained mostly narrow-azimuthal coverage.

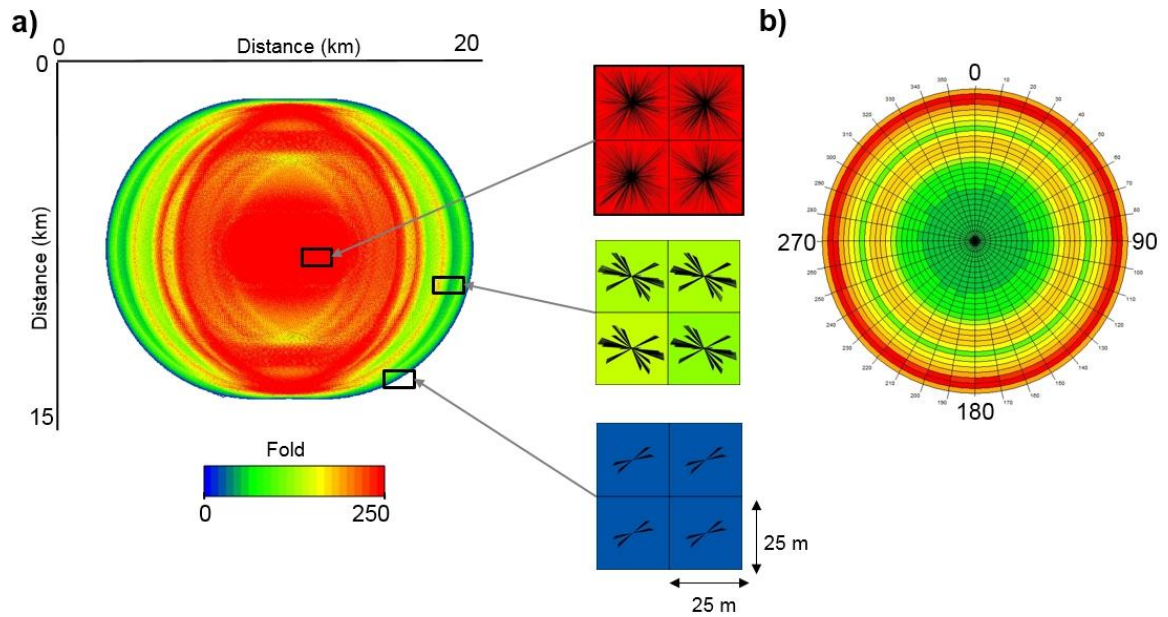


Figure 2.22. The coverage fold and bin azimuth/offset distributions for dual-coil geometry. Bin size is 25 m x 25 m. (a) Spider diagram indicating the azimuthal coverage within the bin for selected areas. (b) Rose plot to show the offset and azimuth distribution for the entire survey. Red colors represent the higher data values, and cool colors represents the lower data values.

### 2.10.2 Updated ellipse design

We are also proposing another alternative design, which updates the previously discussed ellipse geometry. The new geometry consisted of two ellipses that were perpendicular to each other. We tried to keep most of the acquisition parameters similar to the original ellipse design; however, the main difference was that the shot vessels were not using a different sail path. They were using the same sail path as the streamer vessels. This selection was made to simplify the design. The acquisition parameters were as follows:

- Number of sources: 4
- Number of streamers per vessel: 10
- Streamer separation: 120 m
- Streamer length: 10 km
- Receiver spacing: 25 m
- Shot interval for individual source: 100 m
- Axis length: 7 km and 5 km

The analyses over a test survey which included two adjacent ellipses (each included two perpendicular ellipses) were completed. In the ellipse geometry, similar to the dual-coil acquisition, there were two receiver vessels and two source vessels. Each receiver vessel also included a single source array. Therefore, a total number of four-gun arrays were used, hence called a 2 x 4 configuration. The shot sequence was completed sequentially, alternating between S1, S3, S2, and S4, with each vessel generating a shot that was recorded in two spreads. A layout for the perpendicular ellipse geometry test survey can be seen in Figure 2.23.



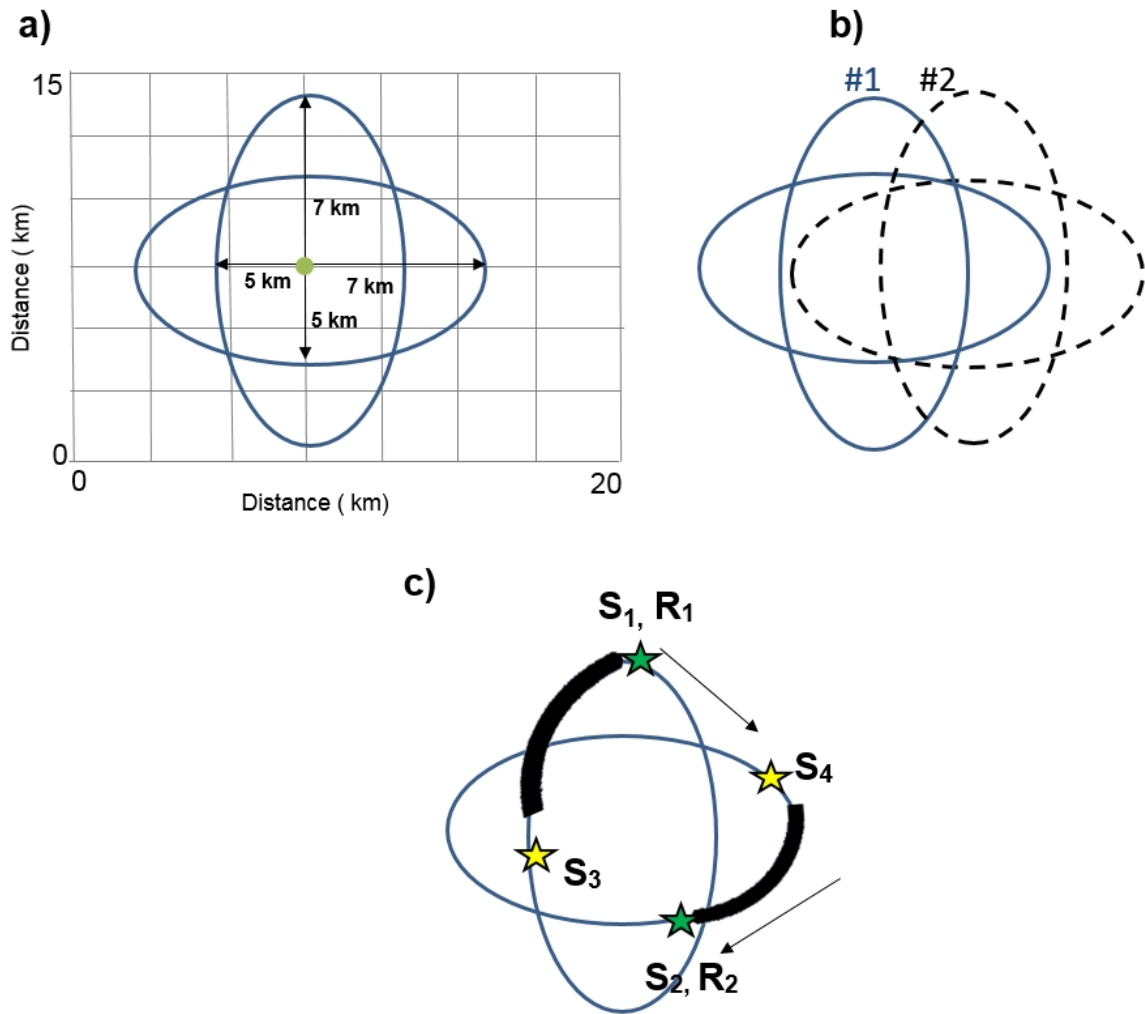


Figure 2.23. Updated ellipse geometry layout. (a) An ellipse with dimensions of the axes. (b) Test survey that included two adjacent ellipses, separated in X direction by 1500 m. (c) Vessel layout for an individual ellipse. The blue lines represent sail lines for both source and receiver vessels. The shot sequence for the vessels were S1-S3-S2-S4.

The updated ellipse design provided azimuthal coverage close to full-azimuth and carried some irregular distribution of the traces; however, overall high fold coverage was seen for most of the survey area. Nearly full-azimuthal coverage for majority of the survey area can be seen in Figure 2.24. However, the bin coverage abruptly dropped into a narrow-azimuth towards the survey fringes. The narrow-azimuthal coverage appeared to be only limited

towards the survey fringes in all directions. All calculations were completed with a bin size of 25 m by 25 m.

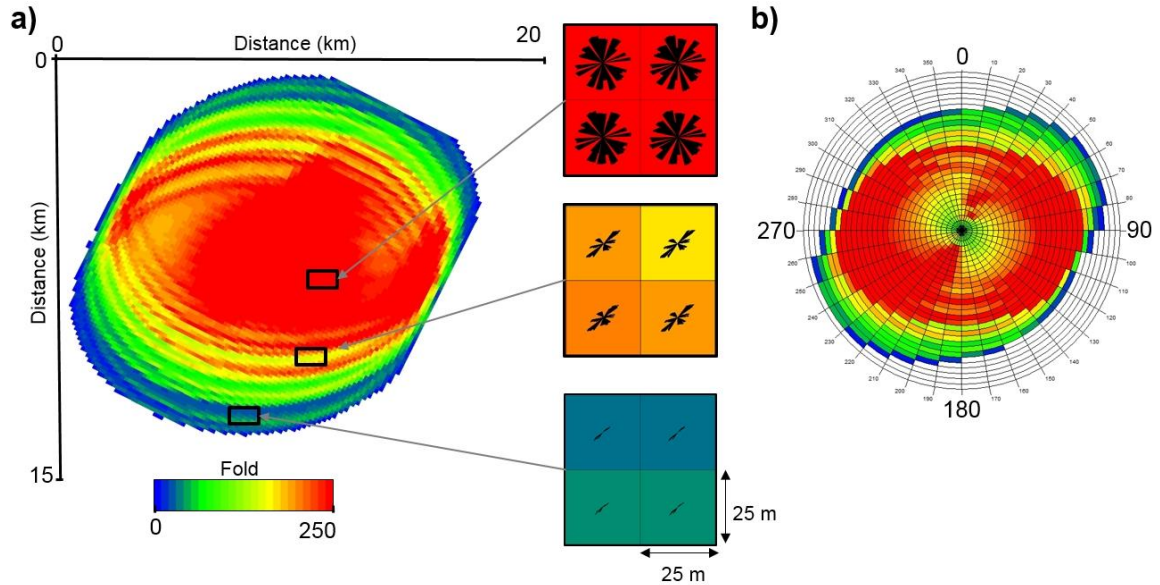


Figure 2.24. The coverage fold and bin azimuth/offset distributions for the test survey with the updated ellipse geometry. Bin size is 25 m x 25 m. (a) Spider diagram indicating the azimuthal coverage within the bin for selected areas. (b) Rose plot to show the azimuth/offset distribution for the entire survey. Red colors represent the higher data values and cool colors represent the lower data values.

### 2.10.3 Controlled streamer feathering

Thus far, seismic survey design for both dual-coil and WAZ geometries were based on vessels towing ~120 m separated streamers. The shifting of the receivers from their ideal location is known as the feathering. The random feathering, due to weather and sea conditions, can create some variability in the content of the azimuthal coverage that may potentially affect the conclusions drawn in our modeling study. In order to prevent the

feather due to external forces “birds” were introduced. These devices can independently steer (streamer flare) individual streamers so that their location can be better controlled.

Dual-coil survey results showed some minor geometry imprints at the survey fringes. These imprints appeared as circle shaped and carried some irregular trace distribution. We proposed controlled streamer flare to minimize some of these geometry imprints. Since these imprints occurred at the survey fringes, we selected 40 coils that were located on the outer edge of the survey area (out of 139 coils) for the streamer flare application. Figure 2.25 compares the regular design of streamers with the streamer flare of 5° and 15°.

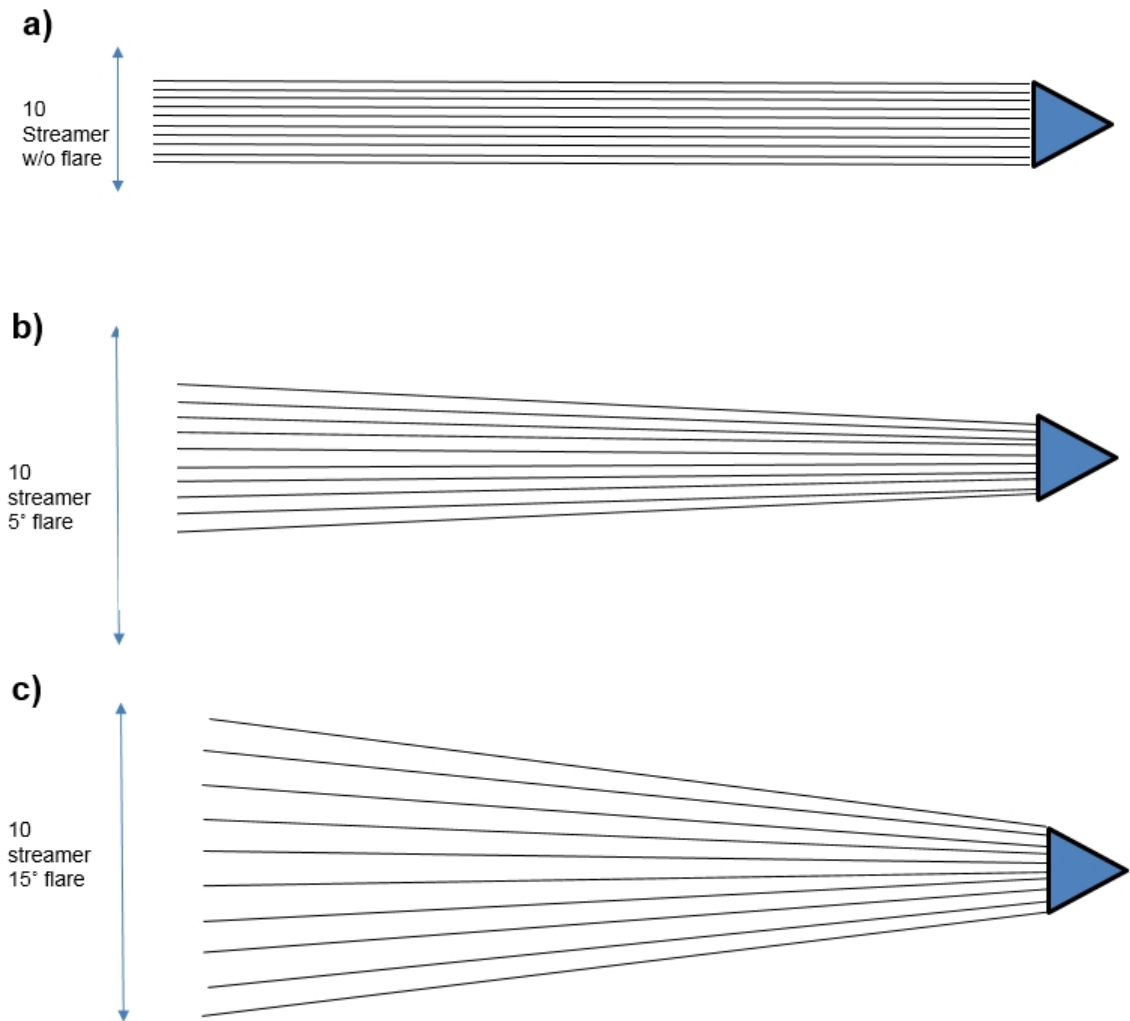


Figure 2.25. The effect of streamer feather. (a) No flare. (b) 5° streamer flare. (c) 15° streamer flare.

With the increasing flare angle the fold maps appears smoother (Figure 2.26) and almost free of geometry imprint (in the case of  $15^\circ$ ). In the case of azimuth/offset distribution, it appears that  $5^\circ$  flare provided the best results as it distributes the traces at the far offsets (instead of gathering them in a circular shape).

However, one should also consider the possible operational difficulties of such a flare angle (e.g., cable tension). The irregular separation of the traces at the survey fringes, introduced by the streamer flare, may also require further processing steps.

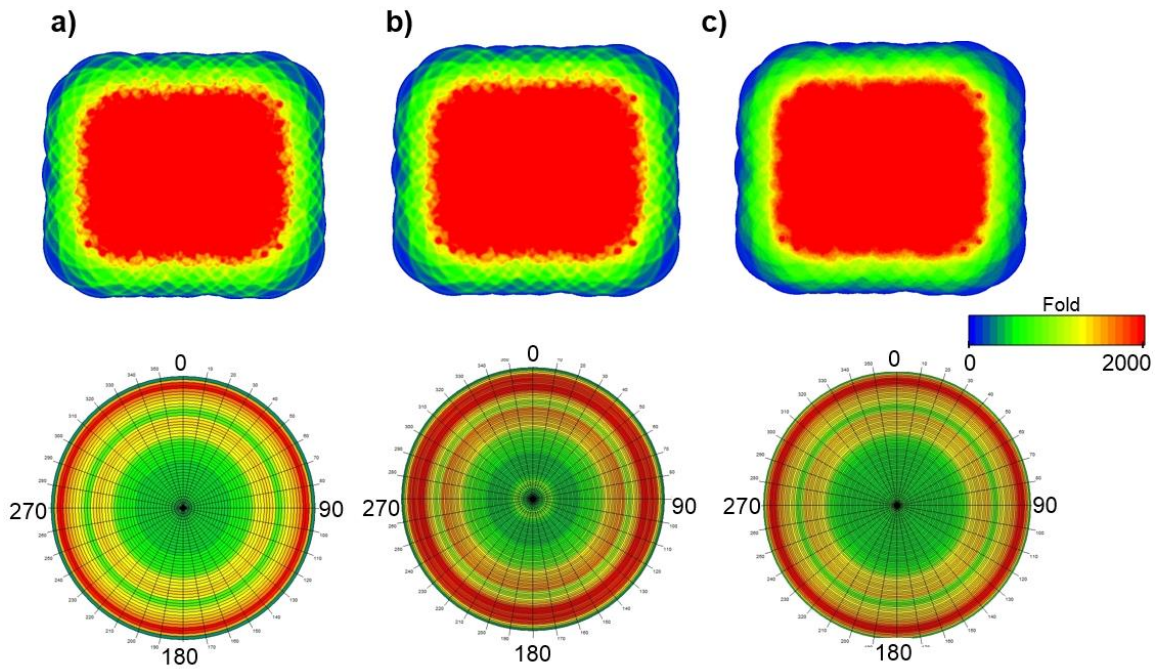


Figure 2.26. The effect of streamer flare angle over fold maps and rose diagrams for offset and azimuth distributions. (a) No flare. (b)  $5^\circ$  streamer flare. (c)  $15^\circ$  streamer flare.

## Chapter 3

### Multicomponent (3C-3D) Seismic Survey Design

#### 3.1 Introduction

The energy industry in North America has been revolutionized in the last 10 years by the development of resource reservoirs in and around shales. In the US, several million barrels of oil per day of new production have been added (EIA, 2013). Many basins around the world are also fortunate to have geology which is prospective for hydrocarbon production from shales (Figure 3.1).

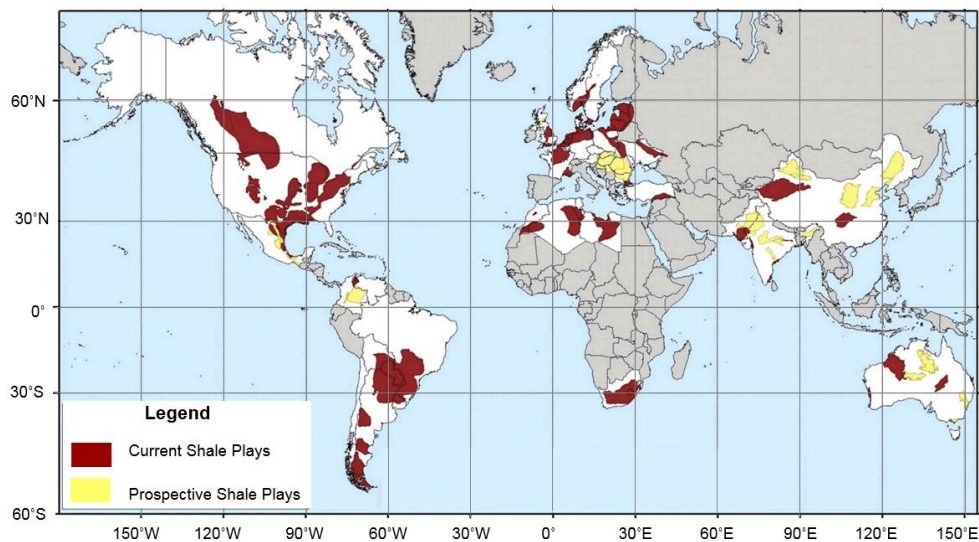


Figure 3.1. Map of unconventional basins around the world for both current (red colored) and prospective (yellow colored) shale plays (modified from EIA, 2013).

The application of multicomponent reflection seismology provides additional information about the subsurface which may be hidden from the conventional seismic surveys. In modern day applications, multicomponent seismic data are used to enhance the results of conventional P-wave data. Some of the other benefits, which can be inferred from multicomponent reflection surveys are (Stewart, 2009; Vermeer, 2012):

- Imaging inside and below shallow gas
- Fault, fracture, and crack identification with the orientation
- Better structural images with more detailed lithology discrimination
- Imaging the subsurface layers with low P-wave contrast and relatively higher converted-wave (PS) contrast

There are multiple aspects for the seismic survey design problems. It is important to understand the effect of survey design parameters in terms of seismic data resolution, offset, and azimuthal coverage while still considering the purpose of the survey. Another crucial factor to keep in mind is that the converted-wave reflection studies are typically chosen to overcome a specific problem observed on the P-wave data; therefore, multicomponent survey design studies should be customized to the specific purpose of that survey.

This particular multicomponent case study deals with the various aspects of survey design and its effect on seismic attribute distributions such as fold maps and azimuth/offset distributions. We mainly concentrated our efforts on orthogonal geometries, however alternative parallel and slant geometries are also discussed. Binning of the multicomponent data also differs from the conventional P-wave surveys, a staggered survey design was adopted to achieve smaller bin sizes without adding additional cost to the seismic survey. In-depth analyses of the binning issue with the multicomponent data can be seen in Cordsen and Lawton (1996). All the survey design and analyses were completed using the Schlumberger – Omni software.

### 3.2 Multicomponent data acquisition and converted-wave

In multicomponent seismic, the main events of interest (after P-waves) is the conversion of the P-wave energy to the S-wave upon reflection. Therefore, recording units at the surface, in the case of land surveys, are required to have multicomponent sensors (three-component) with different orientations to fully capture the reflecting wave-field (Stewart, 2009). At the source end, an ideal multicomponent survey might also include a 3C source. However, due to the additional time requirement for extra shots with 3C vibrator sources and the increase of the acquisition costs, 3C sources are not often used. In modern multicomponent seismic surveys, converted-waves achieved by using a vertical or explosive source generating P-waves, which convert into S-waves in the subsurface layers and recorded as PS-waves at the surface by 3C geophones (Stewart, 2009). These PS-waves have an asymmetric raypath. Figure 3.2 shows the asymmetric raypath and the conversion



point of these PS-waves. The shifting of the conversion point away from the actual mid-point (CMP) towards the receiver is strictly related with  $V_P > V_S$ .

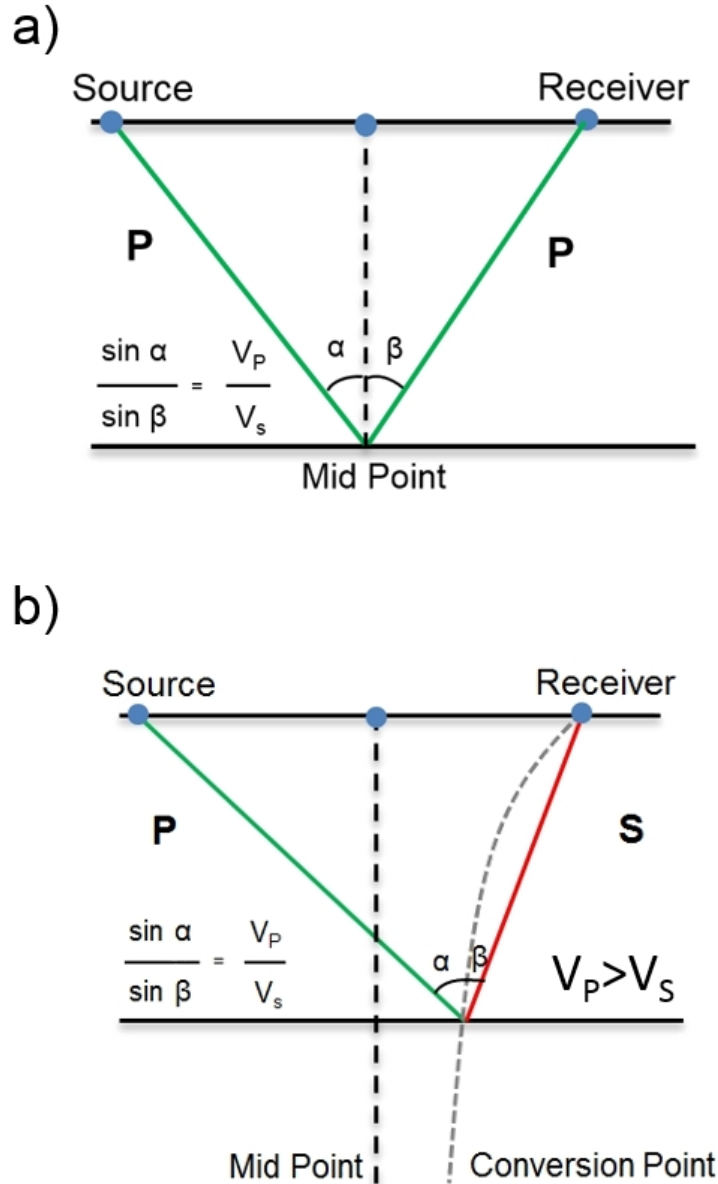


Figure 3.2. Illustration of PP and PS waves. (a) Down going P-wave reflects as P-wave with symmetric ray path (PP-wave). (b) Down going P-wave reflects as S-wave with asymmetric ray path (PS-wave). The conversion point trajectory with respect to the depth is shown with the gray dashed line.

The subsurface coverage from the conventional studies (PP) can be represented as the midpoint distribution between shot and receiver locations. In the case of multicomponent surveys, due to the asymmetric raypaths (PS), the midpoint concept will no longer be applicable (Stewart, 2009).

### 3.3 Test surveys

Only a limited number of articles have been published that discuss multicomponent survey designs in detail with illumination maps (Lawton and Cary, 2003; Stewart et al., 2003; Zuleta and Lawton, 2011). Before designing a full scale multicomponent survey, we created relatively smaller 3D test surveys. A layout for the orthogonal 3C-3D test survey can be seen in Figure 3.3. The 3C-3D survey consisted of 1,512 live receivers with 50 m spacing (24 lines) and 429 shot points with 50 m spacing (11 lines). Further analyses were completed with a bin size of 25 m by 25 m.

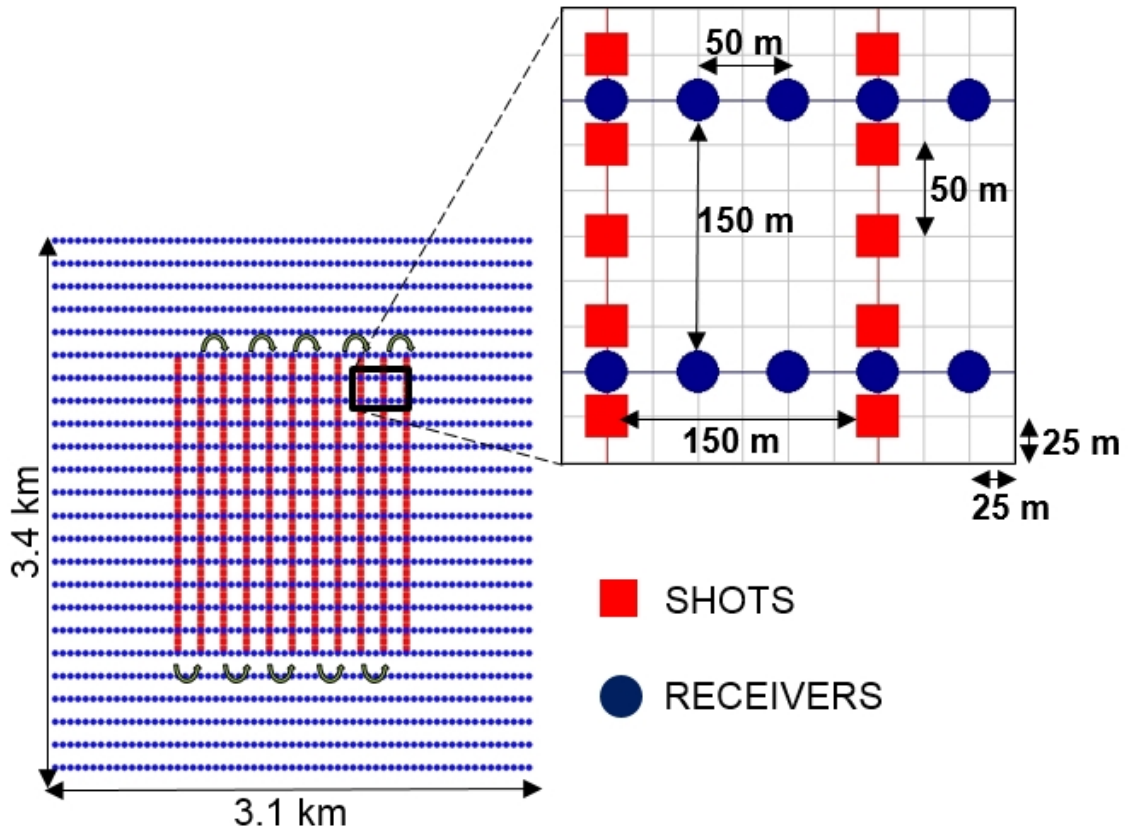


Figure 3.3. Multicomponent (3C-3D) test survey layout for 10.5 km<sup>2</sup> area with a bin size of 25 m by 25 m (gray line). Blue dots illustrate the receiver locations and red lines represent the shot points. Both shots and receiver lines are 150 m apart. The spacing for shot points and receiver locations is 50 m.

We first compared the effect of  $V_P/V_S$  values on the PS fold maps (Figure 3.4). For comparison purposes, the PP fold map is also included in the Figure 3.4. The asymmetric raypath is mainly controlled by the  $V_P/V_S$  values (Vermeer, 2012), higher values provided a broader fold coverage due to stronger shifting of the conversion point away from the survey center, towards the receiver grid. One of the pitfalls related with the fold distribution

is called fold striping, which is a strong variation of the fold from bin-to-bin (Liner, 2004). Fold striping is an undesired effect in seismic exploration (due to signal-to-noise variation).

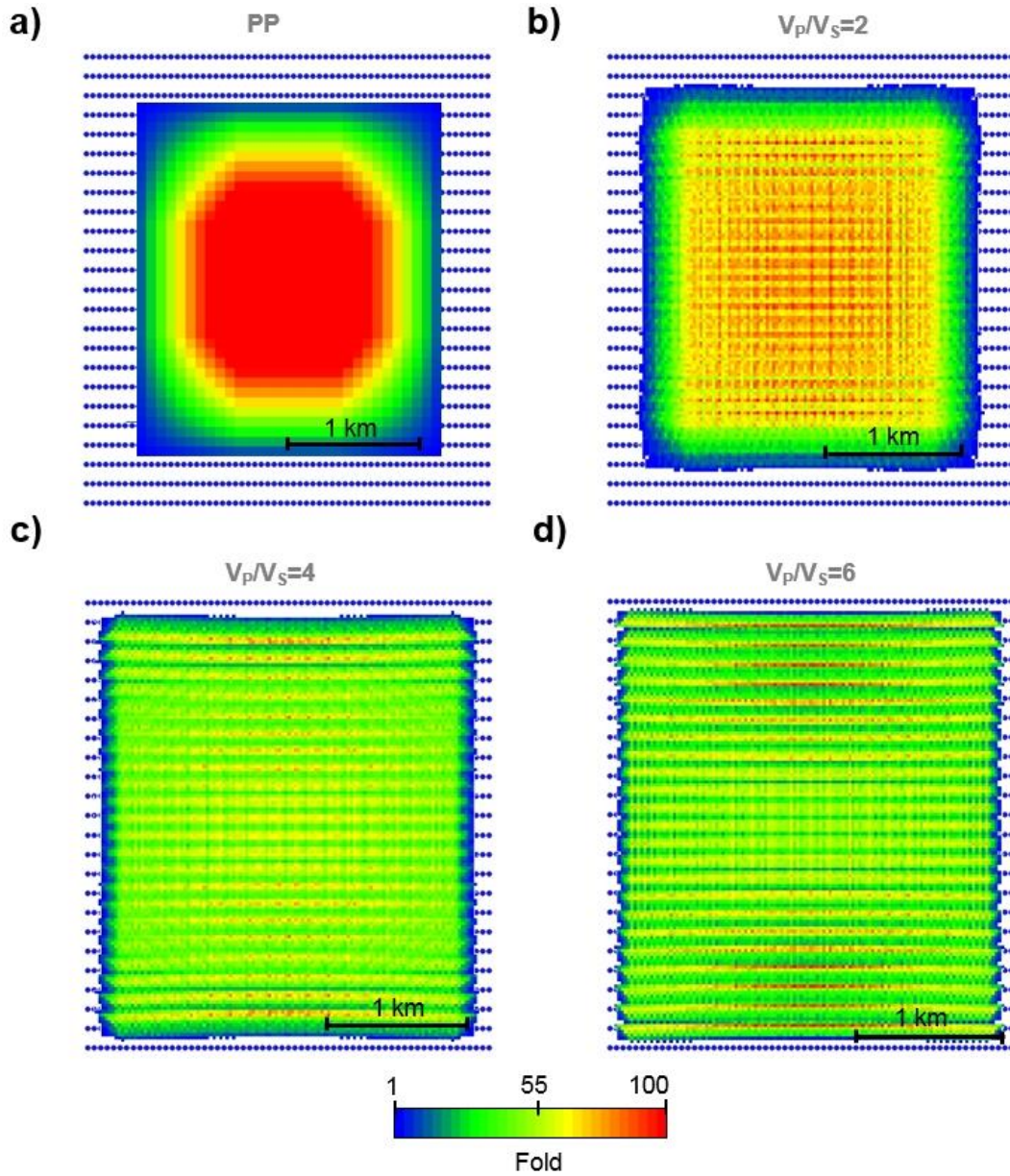


Figure 3.4. PS fold map comparison for various  $V_P/V_S$  values (for a horizontal layer at 1,600 m depth) with a bin size of 25 m by 25 m. Warm colors indicate higher folds. (a) PP fold map. (b) PS fold map for  $V_P/V_S=2$ . (c) PS fold map for  $V_P/V_S=4$ . (d) PS fold map for  $V_P/V_S=6$ . Larger area of coverage with less fold is observed with increasing  $V_P/V_S$ .

The PP studies revealed almost typical “bulls eye” fold map results with higher coverage concentrated at the center and lower fold coverage as the survey fringes. In the case of PS studies, it was evident from Figure 3.4 that relatively smaller  $V_P/V_S$  values helped to obtain smaller coverage area (compared to the PP study) with high fold. As the  $V_P/V_S$  values increased, even though the illumination area became larger, the resulting fold map had lower values. Increase in the  $V_P/V_S$  values also introduced some fold striping.

Reflector depth is another important factor for any seismic survey design study. Specific to multicomponent surveys, the target depth may require further optimization of the design. Figure 3.5 shows the variation of the PS fold coverage with respect to target depth (800 m, 1,600 m, and 3,200 m). For the shallower targets the illumination area was broader with a lower fold distribution. However, for deeper targets, the fold coverage became more concentrated towards the central part of the survey. This concentration was related to the arc shaped CCP trajectory, which carries the conversion point away from the receivers for the deeper target (As shown in the previous section, Figure 3.2).

Before attempting further analyses about multicomponent survey design, we investigated alternative geometries for the test survey. These test surveys contained either 1,512 live receivers with 429 shot points or 1,512 shot points with 429 live receivers for both orthogonal and parallel geometries. These additional tests should enable us to better understand the effects of various geometry related parameters over the illumination maps.

The layout and details of the geometries can be seen in Figures 3.6 and 3.7. All of the design evaluation efforts were based on a horizontal layer laying at 1,600 m depth.

We first compared the fold illumination of PP studies with PS studies using  $V_P/V_S=2$  (Figure 3.6). When dealing with seismic acquisition the layout of receivers and shot lines also plays an important role. A multicomponent survey can favor a specific layout depending on the purpose of the survey.

Our tests compared the effect of inline and crossline bearing for both the shot and receiver lines. Another important aspect of the survey is the selection of the shot and receiver grid; we also compared the results with using shots at the center of receiver grid and the receivers at the center of shot grid.



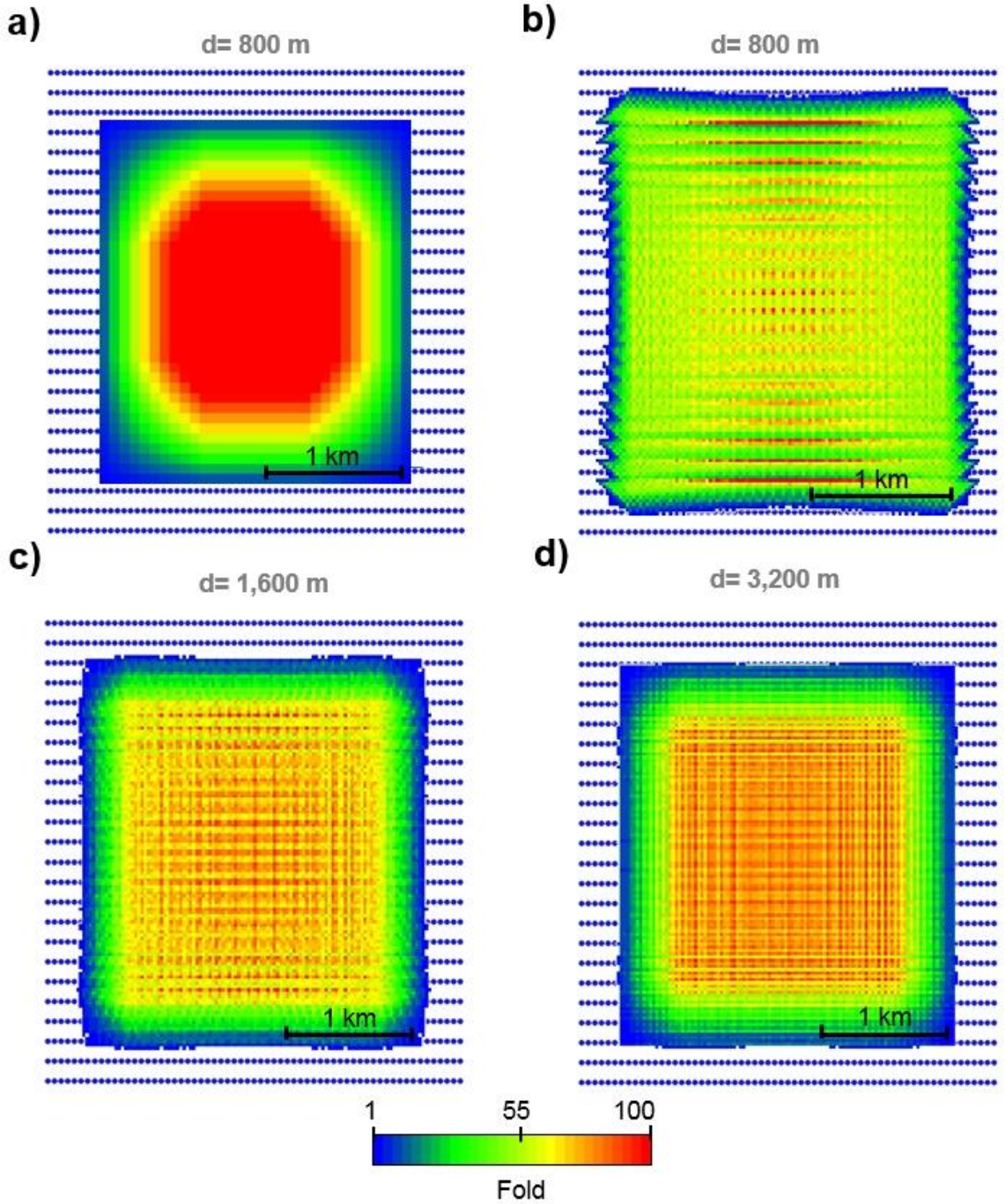


Figure 3.5. Fold map comparison for various target layer depths with a bin size of 25 m by 25 m and using a constant  $V_P/V_S$  value of 2. Warm colors indicate higher folds. (a) PP fold map for a horizontal layer at 800 m depth. (b) PS fold map for the horizontal layer at 800 m depth. (c) PS fold map for the horizontal layer at 1,600 m depth. (d) PS fold map for the horizontal layer at 3,200 m depth. The shifting of CCP away from the receivers, for greater depths, is controlled by the asymmetric raypath.

Primarily, the PP fold map provided the highest fold coverage towards the center and limited fold coverage at the survey fringes. In case of the PS fold map, greater coverage area and shifting of the conversion point towards the receiver line was observed. This shifting was observed as stripes, irregular distribution of the folds, in the fold maps. The shifting effect became nearly negligible when the receiver line was located in the center of a greater shot grid (Figure 3.6a and 3.6b). As the receiver line was centered (surrounded by shot lines), the shifting effect actually helped to achieve a relatively smoother distribution of the folds by pulling the conversion point towards the central part of the survey, where the receivers were located. However, when the shot line was located at the center of a greater receiver grid, the fold coverage area increased significantly (Figure 3.6c and 3.6d). The jump in the coverage area was related with shifting of the conversion point towards the receivers; therefore, having a larger number of receivers than shots can help to obtain PS images on a greater area. The comparison between Figures 3.6a and 3.6c shows that the acquisition geometry, for this specific test survey, had a small effect over the PP fold maps (the fold coverages look very similar). However, the acquisition geometry caused a big difference over the PS fold maps. Even though the PS fold map over Figure 3.6c appears to have some geometry imprints, it provides a coverage on a bigger area (~15 % larger area compared to the Figure 3.6a). The irregular distribution of the fold can cause some problems, although they can be minimized with proper seismic data processing and binning.



It was shown from previous studies that the number of channels used in seismic surveys nearly doubles every five years (Monk, 2014). In general, for land seismic data acquisition, a survey with more receivers than shots are generally preferred due to economic constraints and the geophysical outcome (Monk, 2014). Therefore Figures 3.6c and 3.6d may be the most beneficial layout.

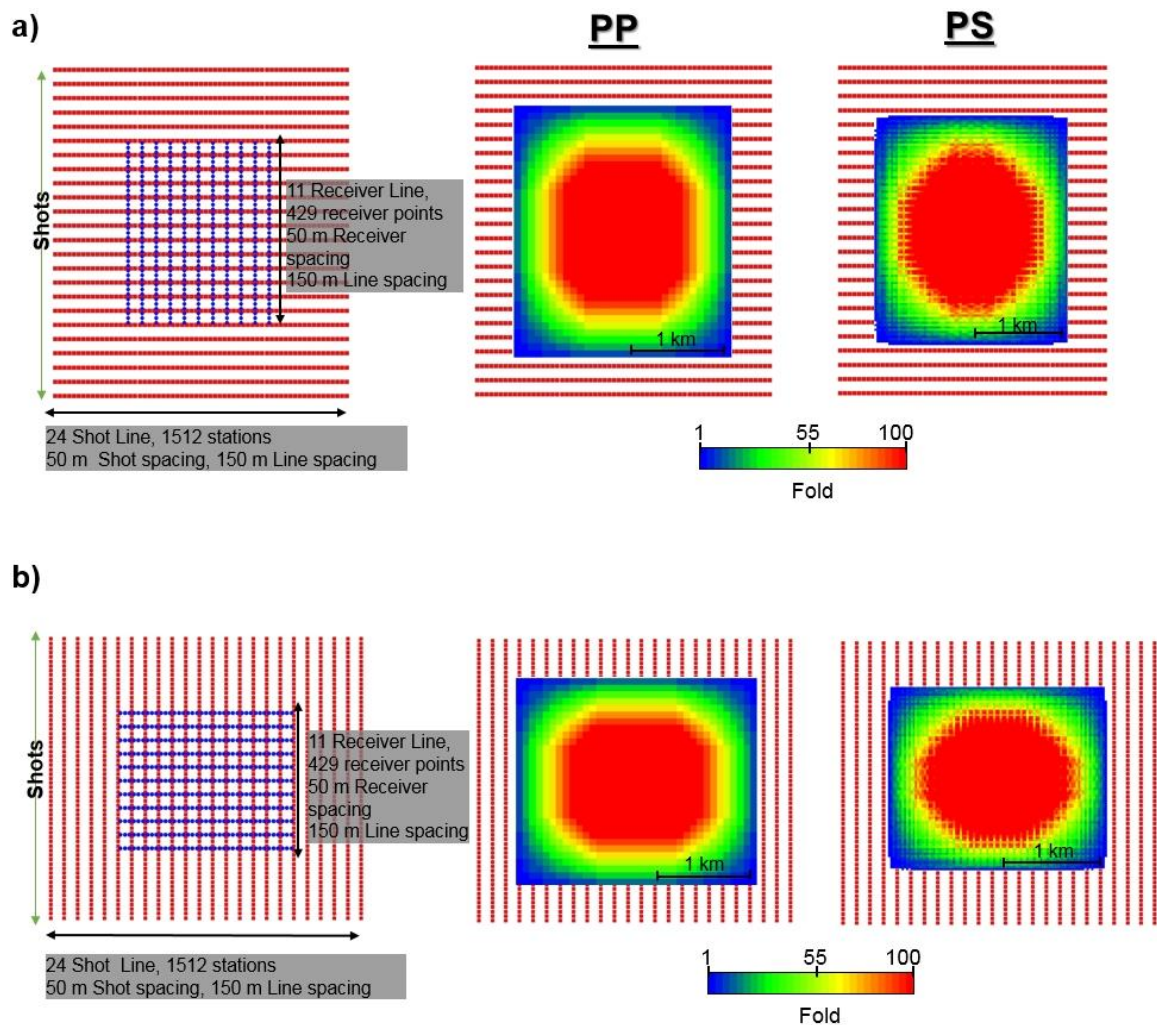


Figure 3.6.

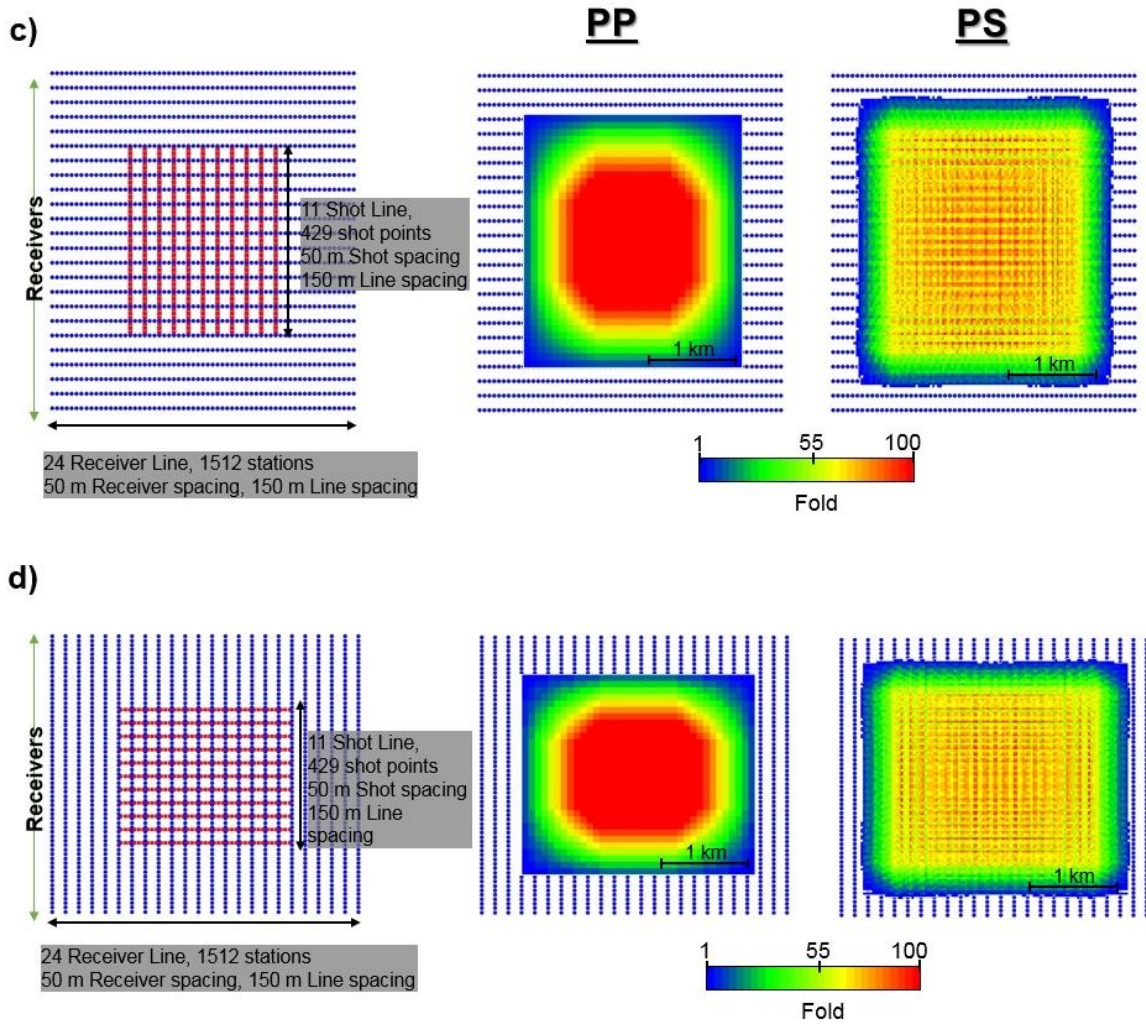


Figure 3.6.cont. Alternative geometry layouts with PP and PS fold map comparison (warm colors indicate higher folds) for the 3D test surveys with a bin size of 25 m by 25 m. Blue lines illustrates the receiver grid and the red lines represent the shot points. All analyses are completed using  $V_P/V_S=2$  and for a horizontal layer at 1,600 m depth. (a) North-south trending receivers are centered in a greater east-west trending shot lines. (b) East-west trending receivers are centered in a greater north-south trending shot lines. (c) North-south trending shots are centered in a greater east-west trending receiver lines (d) East-west trending shots are centered in a greater north-south trending receiver lines.

The selection of the inline and crossline bearing, for both receiver and shot lines, should be purely based on target orientation. Comparison between Figures 3a vs 3b, and 3c vs 3d have showed that they provided nearly identical results with only difference in coverage direction.

So far, the discussion was mainly based on orthogonal type geometry. However, there are other possible options such as parallel geometry (where the receiver and shot lines are parallel with respect to one another) or slanted geometry (where the receivers and shots are no longer  $90^\circ$  apart, but at say  $45^\circ$ ). We tested the effectiveness of these two geometries in Figures 3.7 and 3.8.

Our tests for the parallel geometry included two different scenarios: 1) placing shot lines on top of the receiver lines and vice versa (Figures 3.7a and 3.7b), 2) placing shot lines between the receiver lines and vice versa (Figures 3.7c and 3.7d). Both scenarios resulted in very similar fold maps. The PS fold maps obtained from parallel geometry, aside from some imprints, appeared to provide somewhat similar results as the orthogonal geometries. However, the PP fold maps from the parallel geometry contained empty bins, seen as white stripes, which would result in lack of seismic coverage. To overcome these limitations of the parallel geometry, the number of shot lines should be increased, and the line spacing between both shot and receiver lines should decrease. Such a setting could make the survey too expensive with little or no additional benefit (Vermeer, 2012).

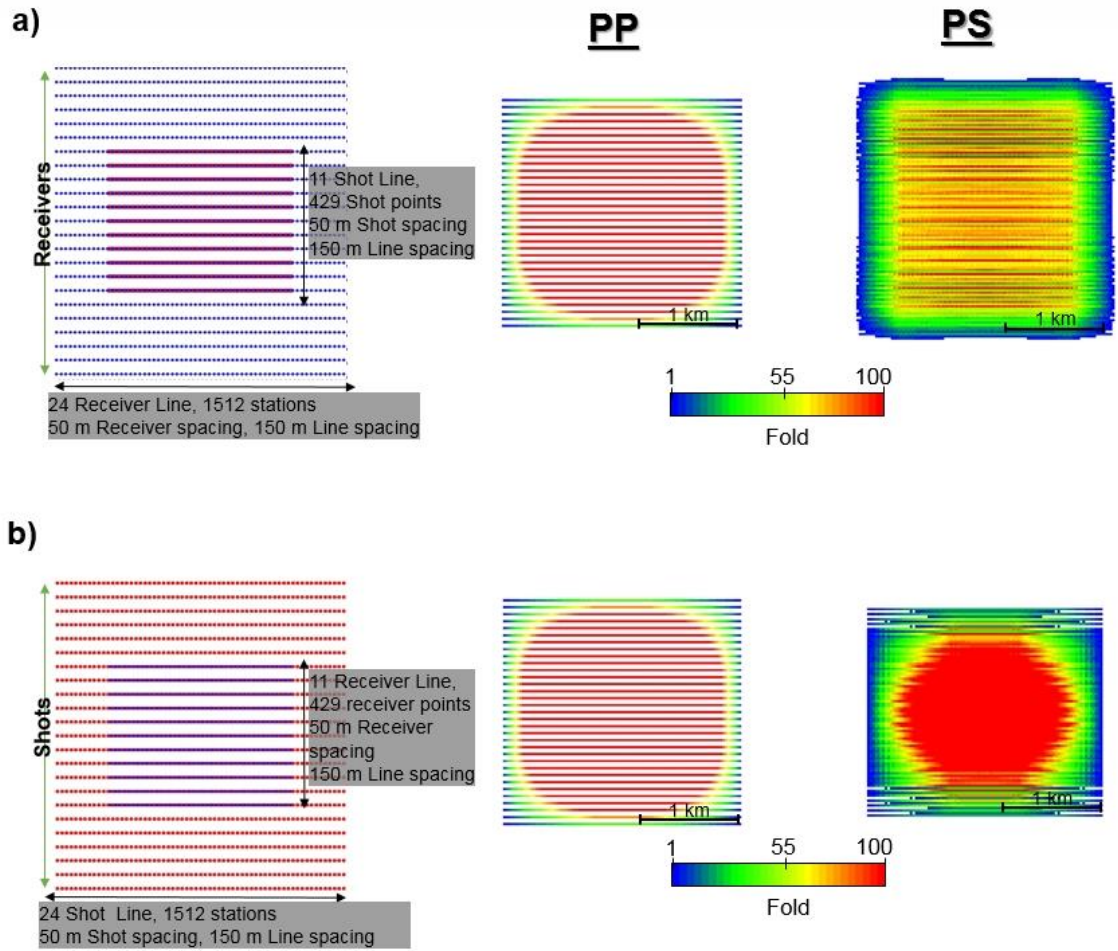


Figure 3.7.



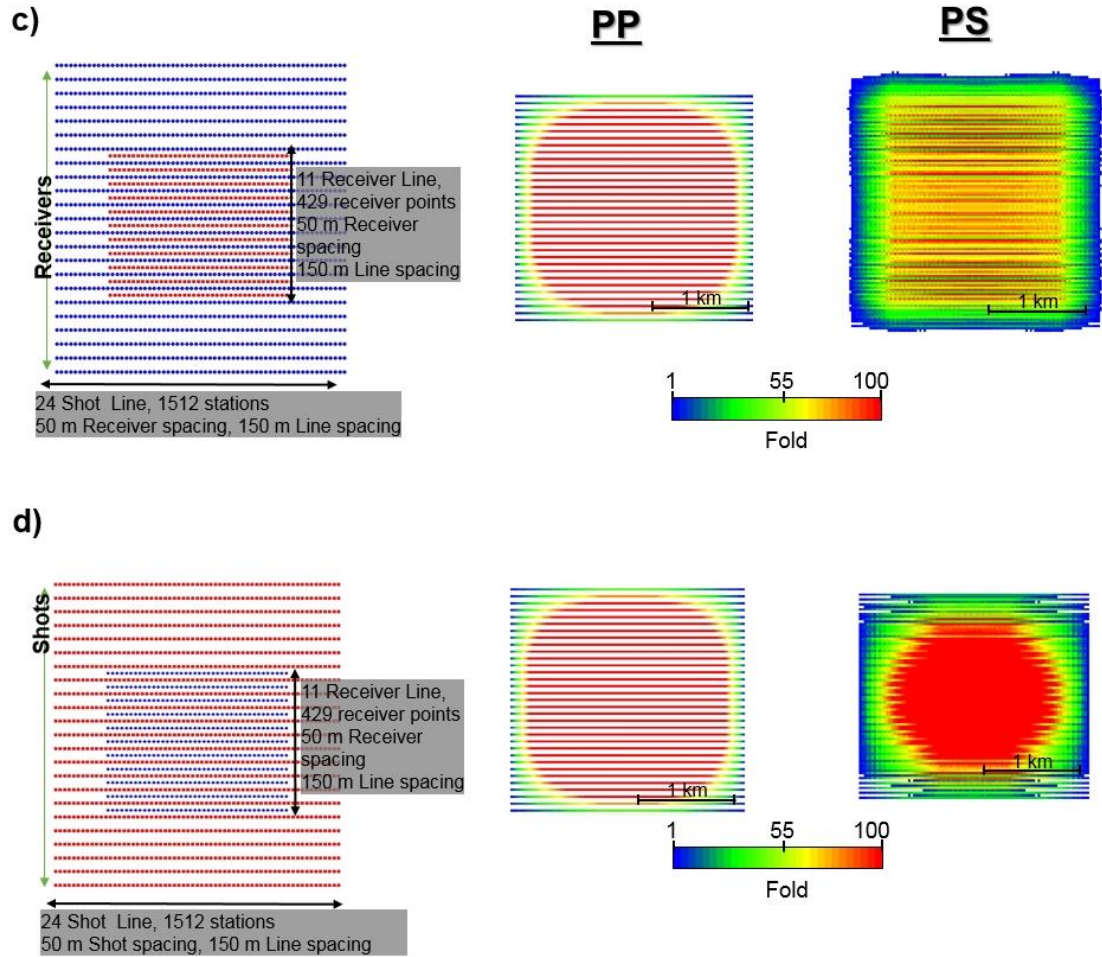


Figure 3.7.cont. PP and PS fold map comparison for parallel geometry with a bin size of 25 m by 25m. Warm colors indicate higher folds. Blue lines illustrate the receiver grid and red lines represent the shot points. All analyses are completed for  $V_P/V_S=2$  and for a horizontal layer at 1,600 m depth. (a) Shots are centered on the receiver lines, parallel to the greater receiver grid. (b) Receivers are centered on the shot lines, parallel to the greater shot grid. (c) Shots are located between the receiver lines (75 m offset), and parallel to the receiver lines. (d) Receivers are located between shot lines (75 m offset), and parallel to the shot lines.

In the case of slanted design (Figure 3.8), relative to the orthogonal design, there was a very limited difference in terms of PP fold and azimuth/offset distributions. However, some

improvements were seen for the PS case. The fold map appeared nearly free of stripes and the traces seemed to be better distributed. Due to re-orientation of the shot lines, the slanted geometry achieved slightly greater maximum offsets (2.3 km vs 2.6 km). The rose plots also indicated improved spatial continuity of offsets and azimuths for the slanted geometry, especially for the near and medium offsets. Most of the geometry related imprints appeared to be minimized for the slanted design.

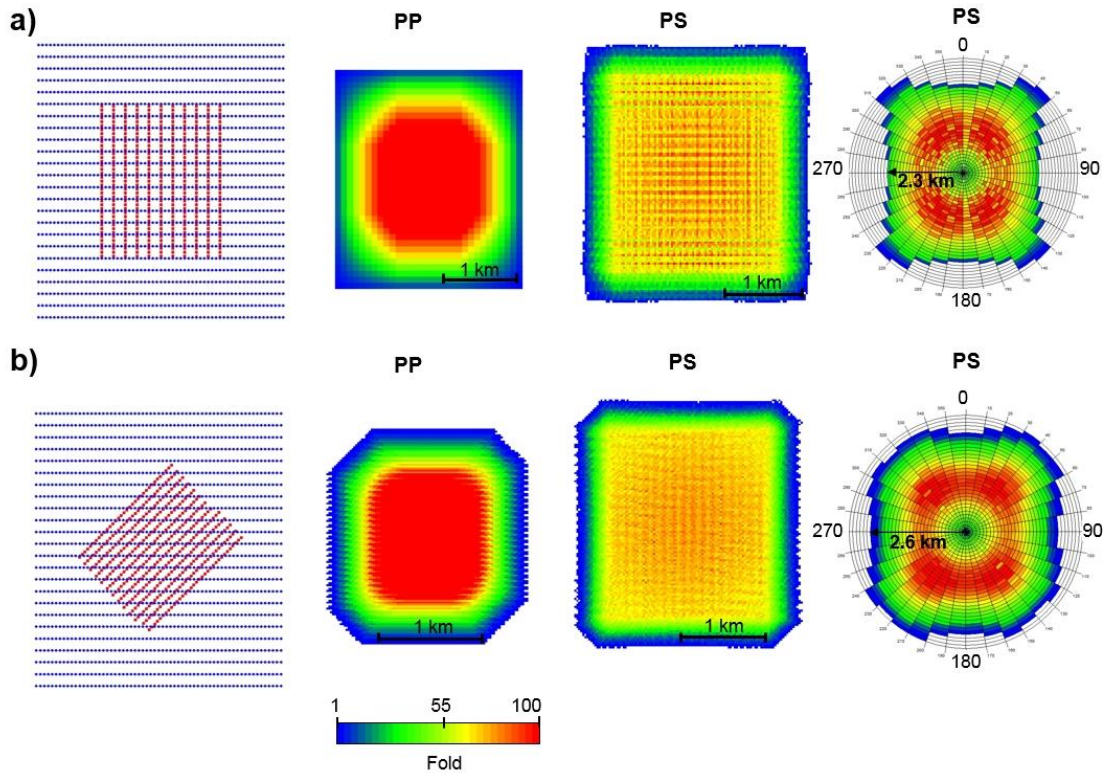


Figure 3.8. Fold map and offset and azimuth diagram comparison for PP and PS surveys between orthogonal and slanted geometries with a bin size of 25 m by 25 m. All analyses are completed for  $V_P/V_S=2$  and for a horizontal layer at 1,600 m depth. Blue lines illustrate the receiver grid and red lines represent the shot points. Warm colors indicate higher data values. (a) Orthogonal geometry. (b) Slanted geometry ( $45^\circ$  angle between shot and receiver lines). Both designs have the exact same number of receivers and a similar total number of shots. Orthogonal geometry provides relatively irregular distribution of offsets and azimuthal coverage when compared to the slanted geometry.

The next part of the analyses concerning the test survey was completed by comparing the effects of the dipping layer. The amount of inclination plays an important role for the subsurface illumination. To better understand the subsurface illumination over inclined surface, we generated a simple 2D geometry layout over a  $15^\circ$  dipping layer (Figure 3.9). The layout includes seventy receivers with 50 m spacing and the single shot point at the center of the receiver line. For a single shot, the upgoing S-waves can be seen in Figure 3.9 (blue and red lines). The unique results for the dipping layers arises from the shifting of the illumination area (Vermeer, 2012) in updip (for both PP and PS) and the concentration of the higher folds in downdip (only for the PS). The downdip rays were concentrated over a smaller subsurface area compared to the widely distributed rays in the updip. Therefore, concentration of high folds in downdip and increase in illumination area in updip is expected.

Figure 3.10 compares the effect of a  $15^\circ$  and  $30^\circ$  dip of the target layer for both the PP and PS studies. As it was suggested from a previous figure, even though the shifting caused bigger illumination area in updip, the high folds began to concentrate towards the downdip due to the asymmetric raypaths. Figure 3.10 shows that the shifting increases with the amount of inclination, indicating that both the illumination shifting and the higher fold concentration became stronger as the inclination increases for these moderate angles ( $15^\circ$  vs  $30^\circ$ ). A more detailed discussions can be seen in Tessmer and Behle (1988), Harrison (1990), and Tang et al. (2010).

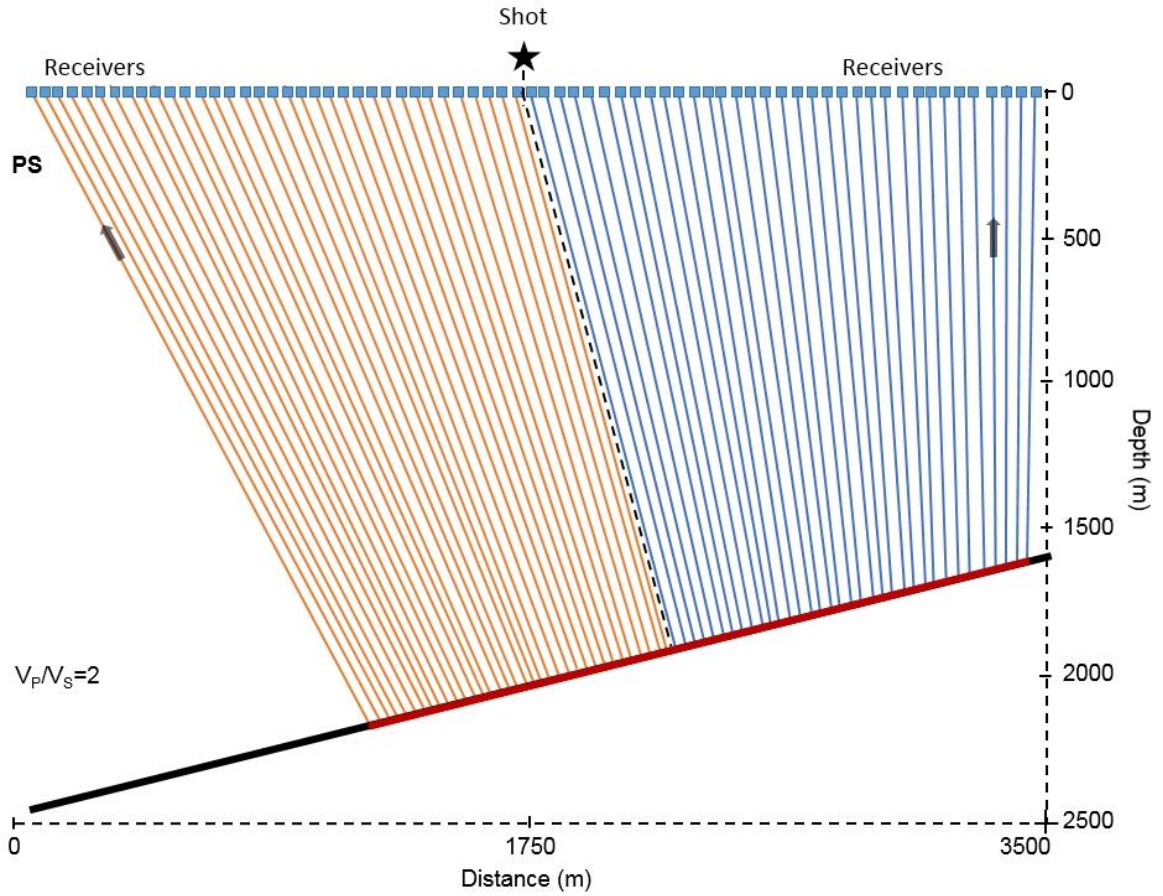


Figure 3.9 2D ray shooting experiment for PS-waves over  $15^\circ$  dipping plane, only the upgoing S-waves are shown for the display purposes. Shot point is illustrated with black colored star, orange lines represents the downdip rays and blue lines represents the updip rays. Subsurface coverage area is colored with red line. Downdip rays are concentrated over relatively smaller area whereas the updip rays are distributed over larger area. Therefore, higher folds are expected in the downdip and lower folds with bigger illumination area is expected in the updip.



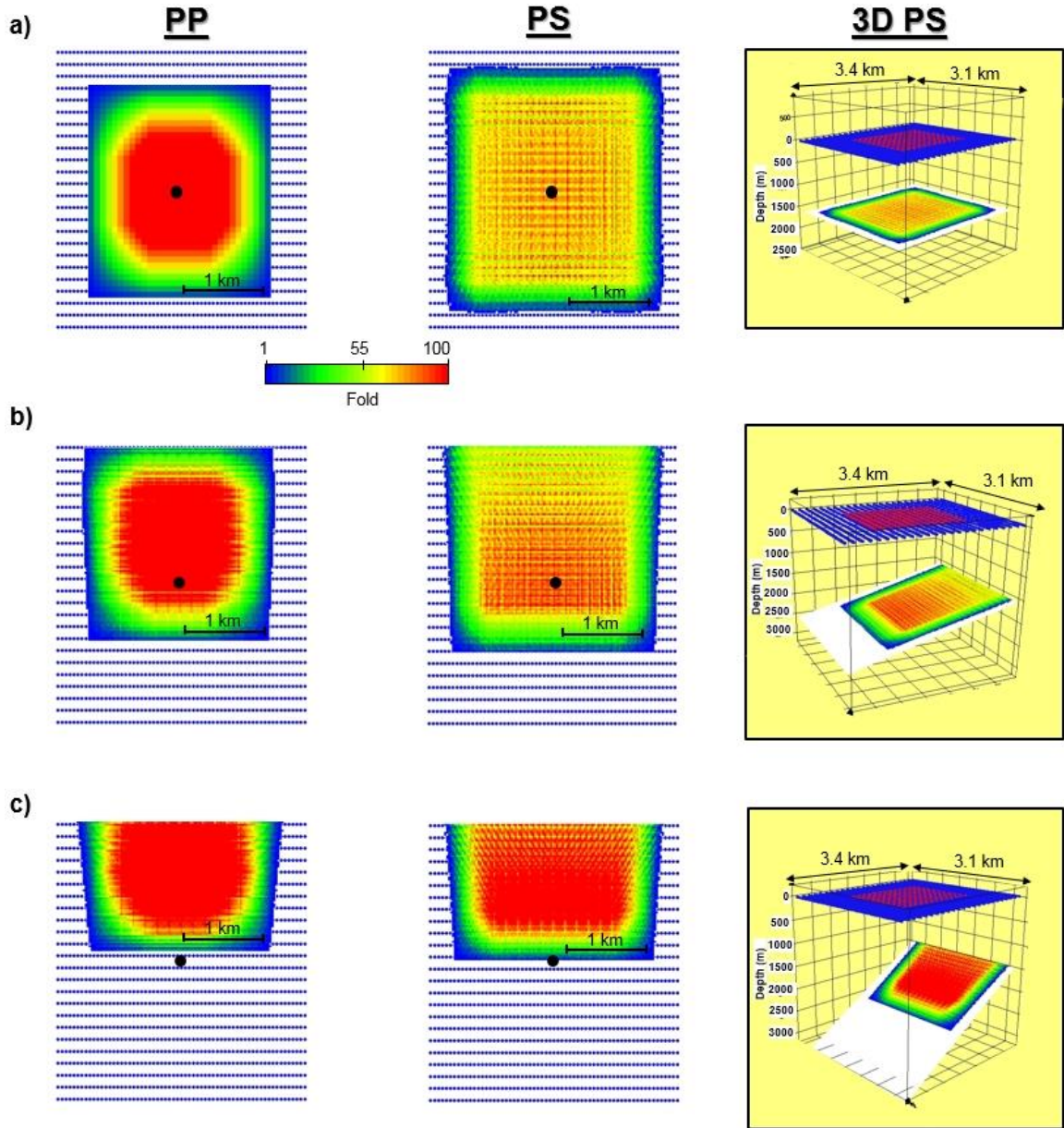


Figure 3.10. Fold map comparison for PP and PS surveys, with a bin size of 25 m by 25m and a constant  $V_P/V_S$  of 2, between horizontal and dipping layers. Warm colors indicate higher folds. Blue lines at the surface illustrates the receiver grid and red lines represent the shot points. The black dot represents the center of shot grid. (a) PP and PS fold map for a horizontal layer at 1,600 m depth. (b) PP and PS fold map for 15° dipping layer with azimuth of 180°. (c) PP and PS fold map for 30° dipping layer with azimuth of 180°.

The fold map for the PP-waves also showed shifting in the updip; however, the symmetric raypaths assisted in obtaining a smoother fold distribution without fold stripes. Increasing the number of receivers at the surface, should help to build larger illumination areas. To test this idea, we extended the number of receiver lines in both the direction of the dip (updip) and the opposite direction of the dip (downdip). The addition of six receiver lines enabled us to obtain a larger illumination area over the dipping layer (Figure 3.11). However, due to updip movement of the illumination area, the effect of these extra receiver lines were limited. Best results, in terms of the illumination area, were achieved when the additional receiver lines are placed in updip direction (Figure 3.11). Therefore, to achieve a proper PS illumination, over a dipping layer, the receiver grid should be extended in the updip direction.

The binning of the seismic data can be a critical aspect for any survey. We compare the results of a various bin size selections to optimize the seismic survey design. A more detailed discussion concerning binning can be obtained from Cordsen and Lawton (1996).

Binning can be summarized as the assignment of seismic traces to an appropriate location (Vermeer, 2012). In a typical orthogonal geometry, bin size should be half of the receiver station interval in the inline direction and half of the shot point interval in the crossline direction (Vermeer, 2012). As mentioned previously, the concept of a common midpoint

(CMP) can no longer be applied to multicomponent data due to asymmetric raypaths, which causes the shifting of the CCP's towards the receivers.

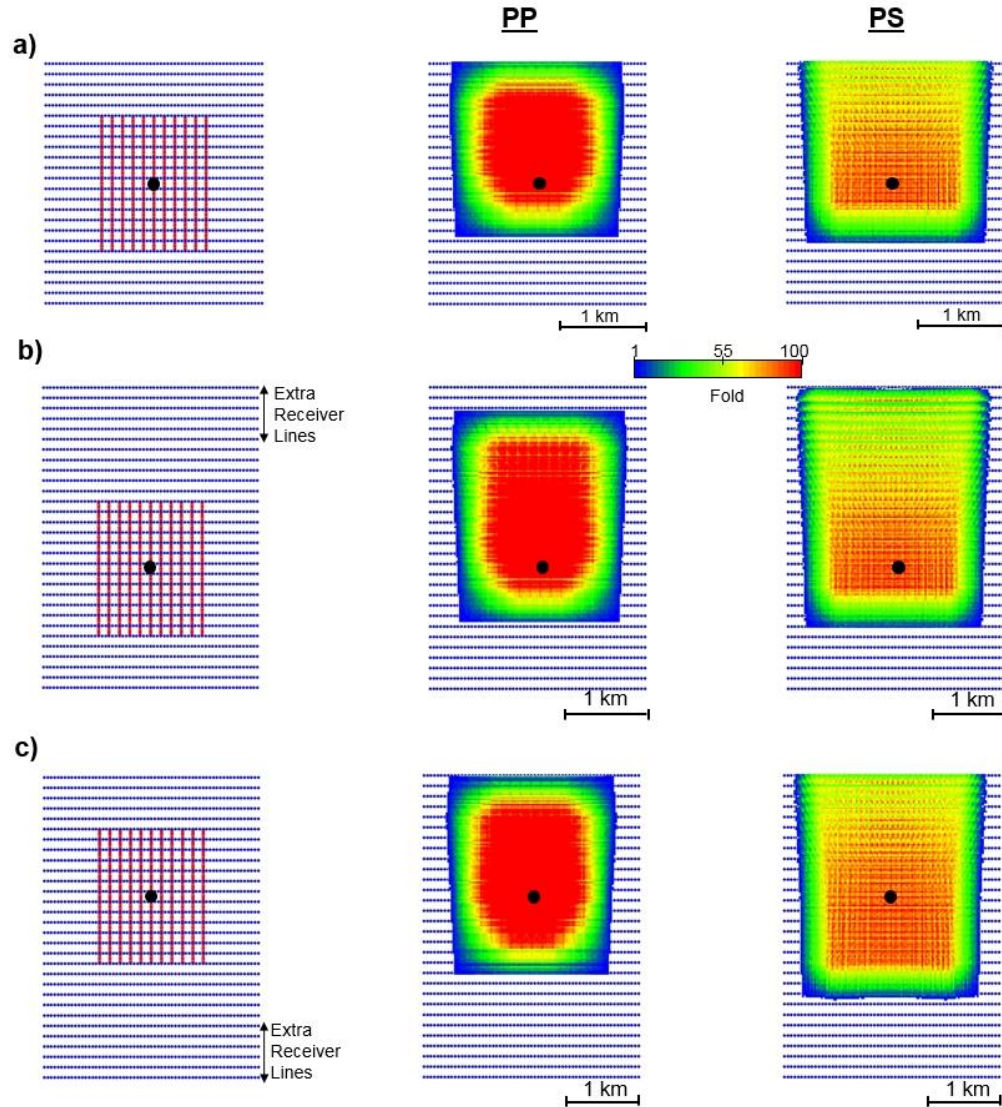


Figure 3.11. The effect of additional receiver lines for both PP and PS fold distribution over the dipping layer with a bin size of 25 m by 25 m. Warm colors indicate higher folds. Blue lines at the surface illustrate the receiver grid and red lines represent the shot points. Total number of 6 receiver lines are added to original geometry. The black dot represents the center of shot grid. (a) PP and PS maps for the original geometry. (b) PP and PS maps for the extra receiver lines towards the updip direction. (c) PP and PS maps for the extra receiver lines towards the downdip. The shifting of the illumination area in updip is stronger for PS studies due to the asymmetric raypath. In terms of illumination, most benefit is obtained by adding the receiver lines in the updip as opposed to downdip.

For this test survey, the ideal bin size would be 25 m by 25 m (inline vs crossline). In a standard seismic survey, all the traces should be clustered towards the central part of the bin, however this may not be the case in real world applications (Liner, 2004). Larger bin sizes help to achieve smoother fold maps, yet smaller bin sizes can actually increase the resolution of the seismic data by eliminating unnecessary averaging within a bin that carries many traces. Selection of right bin size for a specific imaging purposes is an important factor for the seismic survey design. However, one should also consider that the inappropriate selection of the bin sizes could result in irregular trace distribution, strong fold striping, which could cause further complications during seismic data processing and undesirable imaging artifacts.

For the test survey with orthogonal geometry both the PP and PS fold maps can be seen using bin size of 25 m by 25 m, in Figure 3.12a. Without further optimization in survey geometry, PP and PS fold maps were also obtained using the bin sizes of 12.5 m to 25 m (Figure 3.12b). The original survey geometry does not support the updated bin size selection, and the PP fold resulted in empty bins (no data). In the case PS fold, the data values decreased from 40's to 10's within the adjacent bins, which is known as fold striping.

Smaller bin sizes can be achievable by decreasing both receiver spacing and shot spacing, hence increasing the acquisition time and the cost of the survey. An alternative solution to lessen the bin sizes is known as the receiver-line stagger. We numbered the receiver lines as odd and even numbers. Odd numbered receiver lines were pulled towards further west by 12.5 m and the even numbered receiver lines were pushed towards the east by 12.5 m. The re-arrangement of the geometry enabled us to achieve 12.5 m bin size in the inline direction (Figure 3.12c). The PP and PS fold maps for the updated geometry (Figure 3.12c) shows an improvement when compared with Figure 3.12b. The staggering of the receiver lines enabled us to achieve smaller bin sizes without producing fold striping. The receiver-line stagger, compared to the decreased shot and receiver spacing, would require very small acquisition effort and therefore can be considered as a practical approach for obtaining smaller bin sizes.



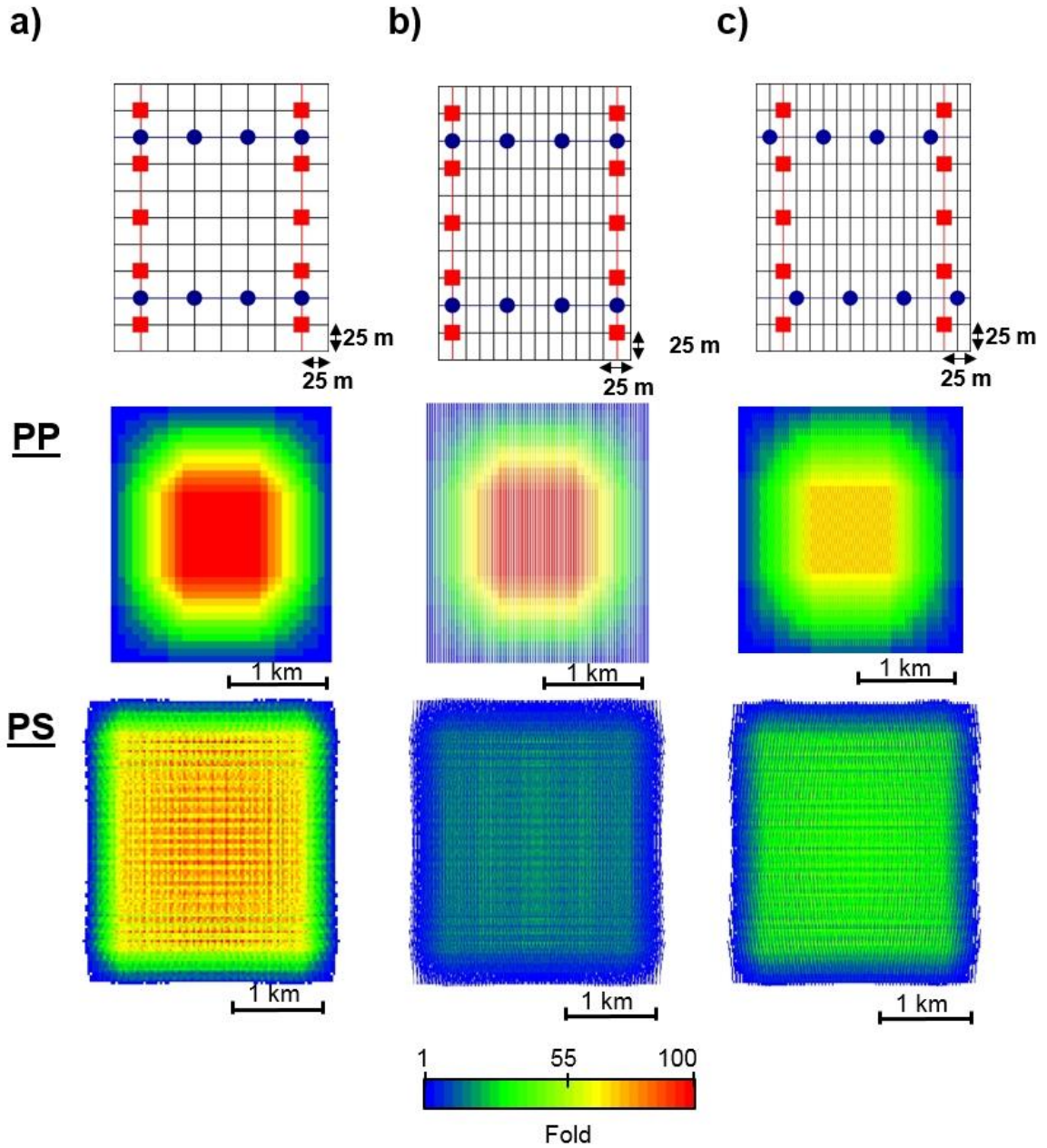


Figure 3.12. The effect of the various bin size over the PP and PS fold maps, warm colors indicate higher fold values. (a) Orthogonal geometry using 25 m by 25 m bin size. (b) Orthogonal geometry using 12.5 m by 25 m bin size. (c) Orthogonal geometry with staggered receiver lines using 12.5 m by 25 m bin size. Original design does not support the smaller bin sizes and resulted in empty bins for PP survey and fold striping for the PS survey. The receiver-line stagger achieved smaller bin sizes without any major artifact on fold maps.

Multicomponent surveys (PS) also differs from conventional PP surveys in terms of required recording time. The down going P-waves will be reflected as the S-waves and considering the rule of thumb that  $V_P > V_S$  (Sheriff, 2002), the PS-waves will travel slower than the PP-waves. To fully capture the converted-wave-field, the recording time should be increased. Liner (2004) generalizes the minimum required time for seismic surveys as:

$$T_{\max} \geq \frac{3.13 Z_{\max}}{V_{\text{avg.}}}$$

Additional discussions and generalized formulas related with the travel time of the converted-waves can be seen in Liner (2004).

We created a simple 2D earth model to observe the effects of the dipping layers on the surface recording time (Figure 3.13), using the seismic velocities annotated over the model, for a horizontal target layer at 1,600 m. We then compared our model results with the formula provided above for a given values of  $Z=1,600$  m and  $V_{\text{avg}}=2000$  m/s.

$$T_{\max} \geq \frac{3.13 \times 1600}{2000}$$

$$T_{\max} \geq 2.5$$

The results from both calculations indicated the requirement of at least two and a half seconds of seismic data.

We then introduced 15° and 30° dip respectively and the minimum record times were increased to four and five seconds respectively. These recording times were referred as minimum recording time, due to usage of straight rays during calculations (rather than curved rays).

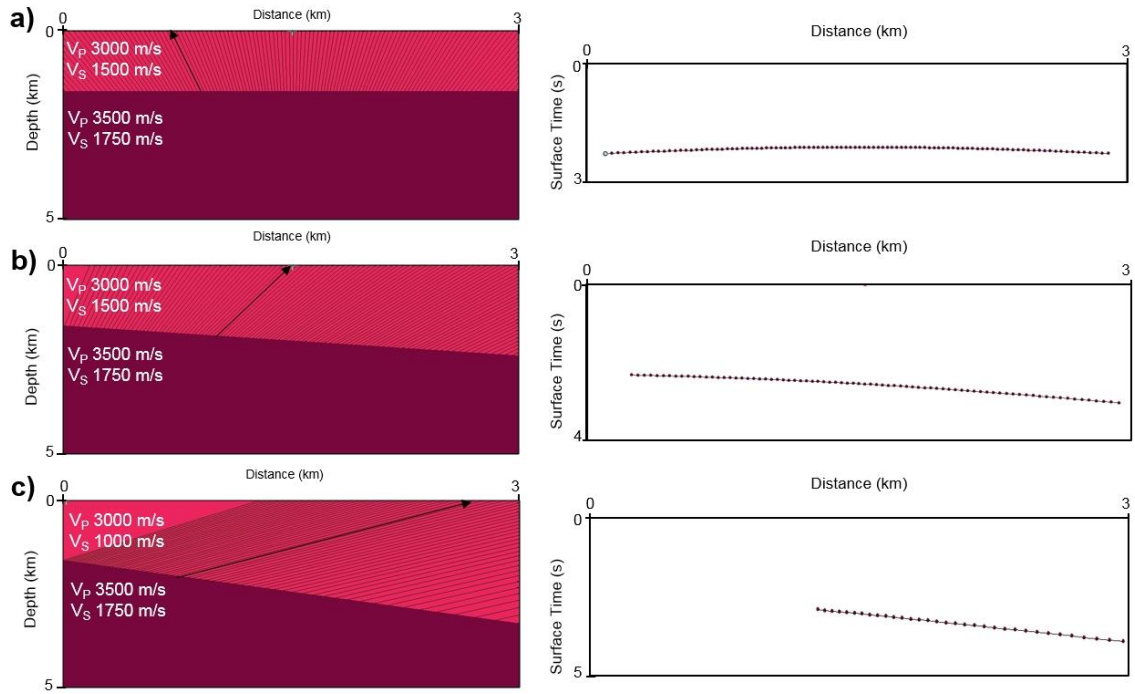


Figure 3.13. Two layer subsurface models for the calculation of surface recording time using PS rays, corresponding  $V_P$  and  $V_S$  values for the layers are annotated. Black lines in the subsurface models represents the reflected rays from the boundary, source rays were not displayed for display purposes. (a) Subsurface model with horizontal layer at 1,600 m depth and recorded reflections times (in seconds). (b) Subsurface model with 15° dipping layer towards south and recorded reflections times (in seconds). (c) Subsurface model with 30° dipping layer towards south and recorded reflections times (in seconds).



These analyses indicated the importance of survey design for the multicomponent surveys, as individual parameters had strong effect over the target illumination. The following section will discuss the details of an industrial-type, full scale multicomponent survey design for an unconventional play.

### 3.3 Full scale multicomponent (3C-3D) survey design

The 3D seismic survey covers an area of 900 km<sup>2</sup> (Figure 3.14). The survey will use an orthogonal recording geometry with dynamite and vibroseis sources and say DSU3 accelerometers as receivers. The multicomponent seismic survey, approximately 16 km by 16 km, is embedded in the much larger single-component sensor survey (a conventional 3D) which measured over 30 km by 30 km. In this section, we will only consider the 3C-3D seismic survey.

We used 13,400 shots (shot intervals of 50 m) in 67 shot lines (spaced at 150 m) undertaken in three zippers or blocks. The area of shot coverage was 9,950 m (NW) x 9,900 m (NE). The survey was completed in three zippers or shot blocks (south shooting, then back north, and lastly south – see Figure 3.14). The survey had 81 receiver lines (spaced at 200 m) with 318 receiver positions (spaced at 50 m). Therefore, the total number of 3C receiver positions was 25,758.

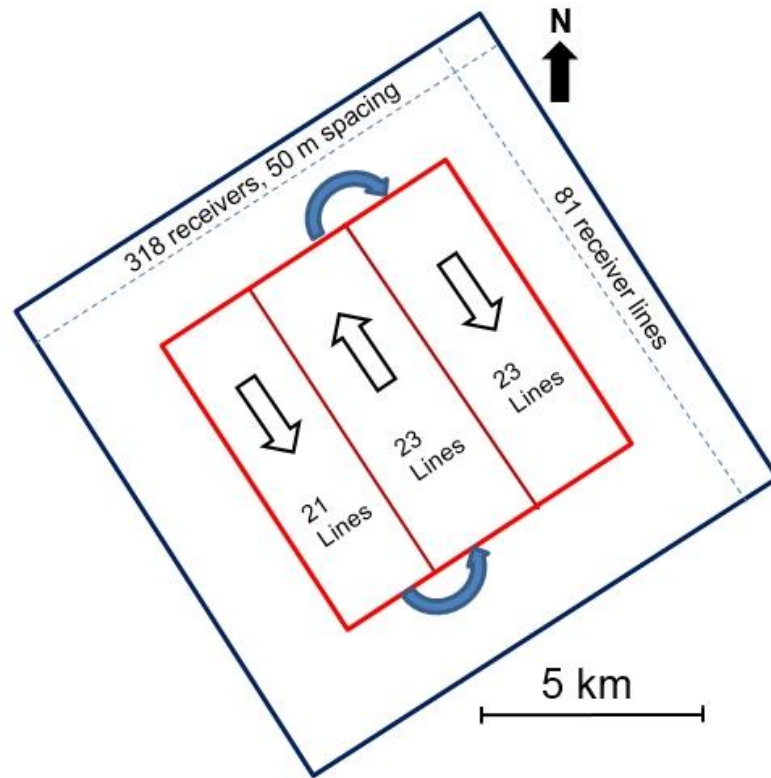


Figure 3.14. Sketch of the 3C-3D seismic survey with some of the acquisition parameters. Blue square outlines the receiver grid (81 lines) and the red square outlines the shot grid (67 lines). The survey was completed with three zipper blocks.

### 3.3.1 Live receiver patch and shot sequence

For each shot there was a patch of 3,840 (32 lines x 120 positions) 3C receivers live. The dimensions of the recording patch were 6,200 m (NW) by 5,950 (NE). There were either 252 shots (Zipper 1) or 276 shots (Zippers 2 and 3) recorded by each patch. Shooting proceeded by recording three shot salvos - where there were four shots between each receiver line. Then three receiver lines were rolled in the direction of shooting. The

selection of salvos and the live receivers were purely done to keep the cost of the survey limited.

The salvo shooting introduced some artifacts. In Figure 3.15, the effects of salvo shooting are compared. It was clear that the increased shot salvo caused somewhat strong, unwanted acquisition footprints. These footprints were directly related with the irregular distribution of the offsets, which eventually produced fold stripes in the resulting data. For this seismic acquisition, the compromise between data quality and decreased surveys costs (due to increased salvo rolls) was found to be reasonable, and the survey was completed using three shot salvos.

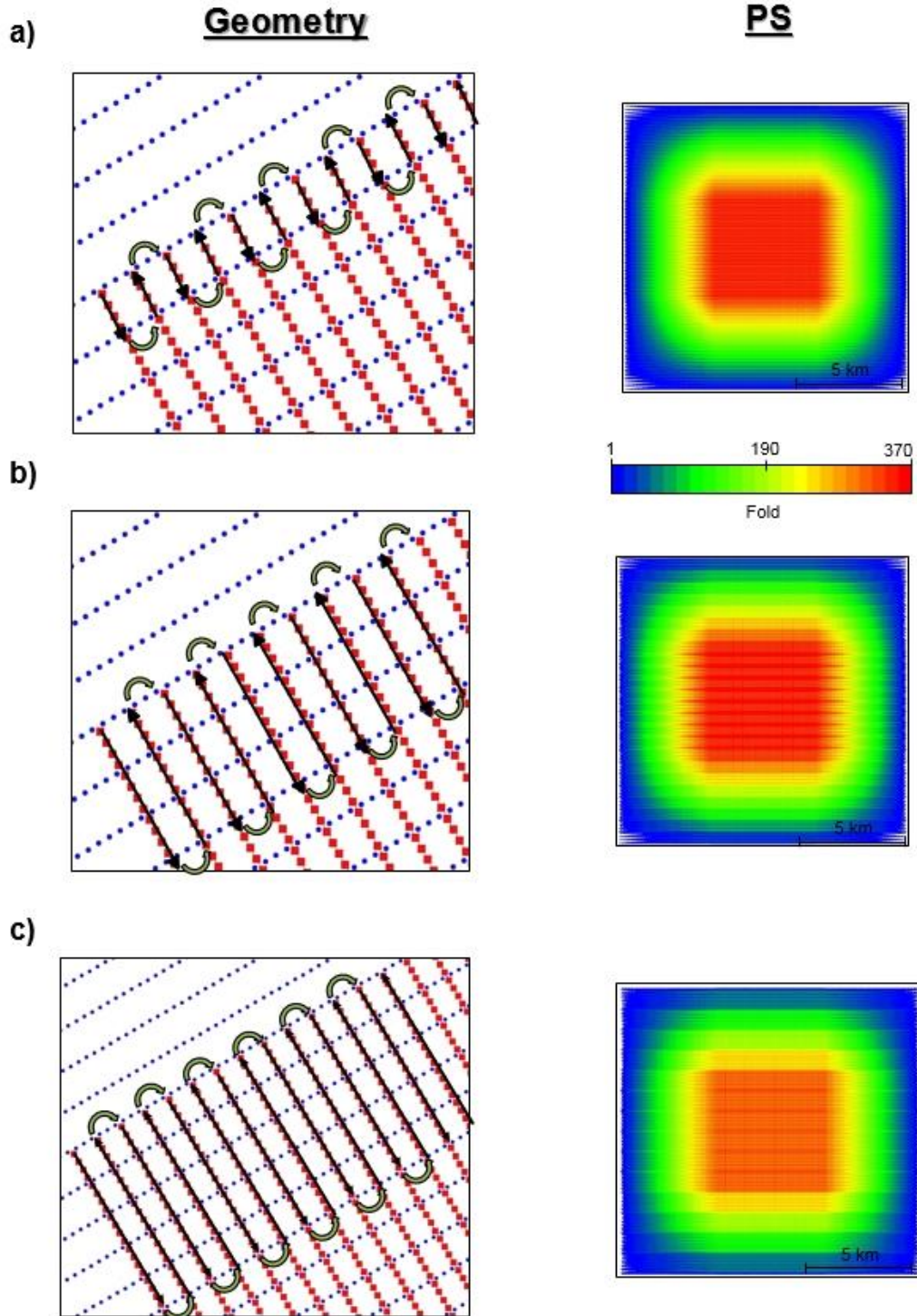


Figure 3.15. The sketch of shot salvos with their effect on PS fold (warmer colors indicate higher values of fold) using bin size of 25 m by 25m. Blue dots indicate the receivers and red dots indicate the shot points. (a) One shot salvo. (b) Three shot salvo. (c) Five shot salvo. Higher salvo rolls introduced acquisition footprints over the fold maps.

### 3.3.2 Dipping target

In this section, we will assume that the target layer is dipping with an approximate  $5^\circ$  towards the southwest. We do not expect to see any major changes in fold illumination caused by the dipping plane. The illumination comparison between the horizontal layer and the  $5^\circ$  dipping layer can be seen in Figure 3.16. The shifting of the CCP's towards the updip direction was limited due to a gentle dip (Figure 3.16). Another factor for the limited change of the fold illumination was the existence of long offsets. The geometry design consisted of a larger receiver grid which surrounds the centered shot lines, therefore capturing essentially all reflections from the dipping target layer. Overall, the fold map appeared very similar with a slight shifting in the updip direction. For the rest of the analyses, we used the target layer with  $5^\circ$  dip towards the southwest.

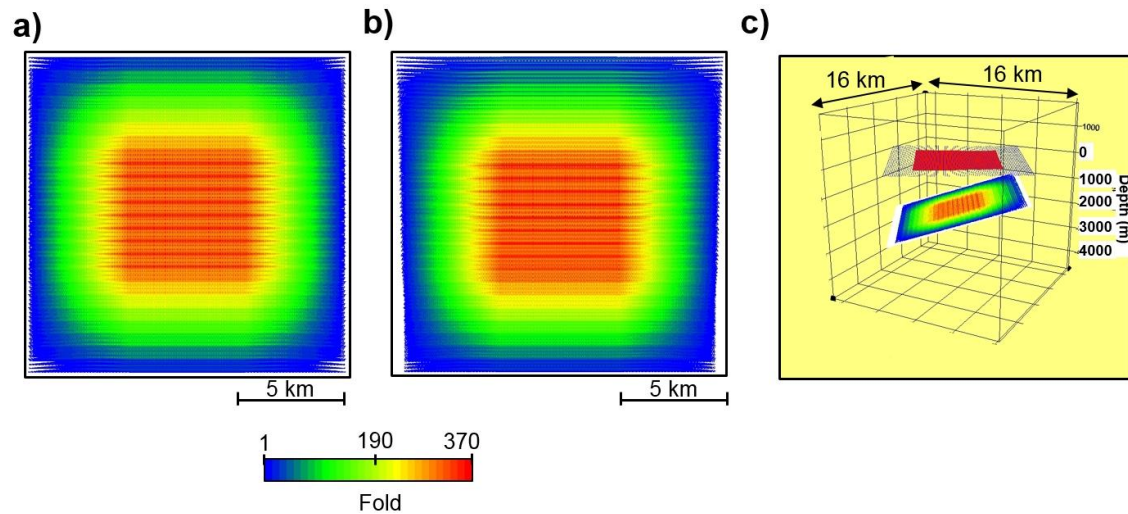


Figure 3.16. PS fold map comparison between the horizontal layer and the dipping layer, warm colors indicate higher folds. (a) PS Fold map for horizontal layer at 1,600 m depth. (b) PS Fold map for  $5^\circ$  dipping layer towards Southwest. (c) 3D PS fold map for  $5^\circ$  dipping layer towards Southwest. Blue lines at the surface illustrate the receiver grid and red lines represent the shot lines.

### 3.3.3 Receiver-line stagger

For this multicomponent survey, the ideal bin size would be 25 m by 25 m (inline vs crossline). An alternative solution to lessen the bin sizes was the receiver-line stagger (discussed in the previous section). We numbered the receiver lines as odd and even numbers. Odd numbered receiver lines were pulled towards further southwest by 12.5 m and the even numbered receiver lines were pushed towards the northeast by 6.25 m. The re-arrangement of the geometry enabled us to achieve 6.25 m bin size in the inline direction (Figure 3.17). One of the potential drawback of reduced bin sizes were the increase of the processing costs. Cutting the bin size to 6.25 m from 25 m increased the total number of prestack traces by four times.

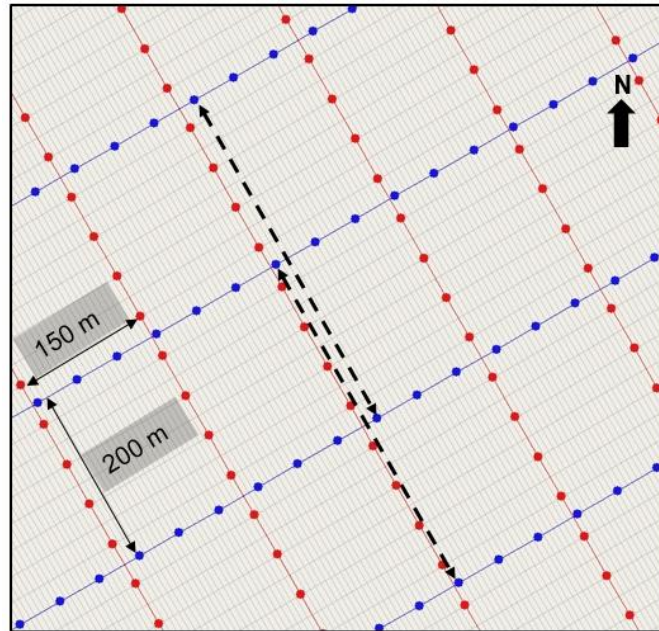


Figure 3.17. Updated survey geometry with staggered receiver line pattern to obtain smaller bin sizes. Gray lines represent the individual bins (6.25 m by 25 m). Red dots represent the shot points and blue dots represent the receiver locations.

### 3.3.4 Comparison of staggered and non-staggered receiver lines

The re-arrangement of the receiver lines enabled us to achieve 6.25 m by 25 m bin sizes without producing fold striping. The reduction of the bin size in the inline direction prevented the survey to reach higher fold values when compared to the original design with 25 m bin size (Figure 3.18). However, the fold illumination still delivered a modest amount of fold ( $\sim 90$ ) for most of the survey area. The acquisition imprint, generated by the shot salvos appeared to have minimal effects for the offsets between 500 m to 2,500 m (Figures 3.18c and 3.18d). Using the smaller bin sizes, we managed to obtain fold distribution free of fold striping over all of the offset ranges.

Another important aspect to evaluate the impact of the bin size over the entire survey, is the azimuth/offset plots. The effect of smaller bin sizes can be seen in Figure 3.19 as rose plots. Both designs yielded somewhat similar results. The trace distribution of the smaller bin size appears to be slightly irregular when compared to the larger bin sizes, however the difference was very minimal.



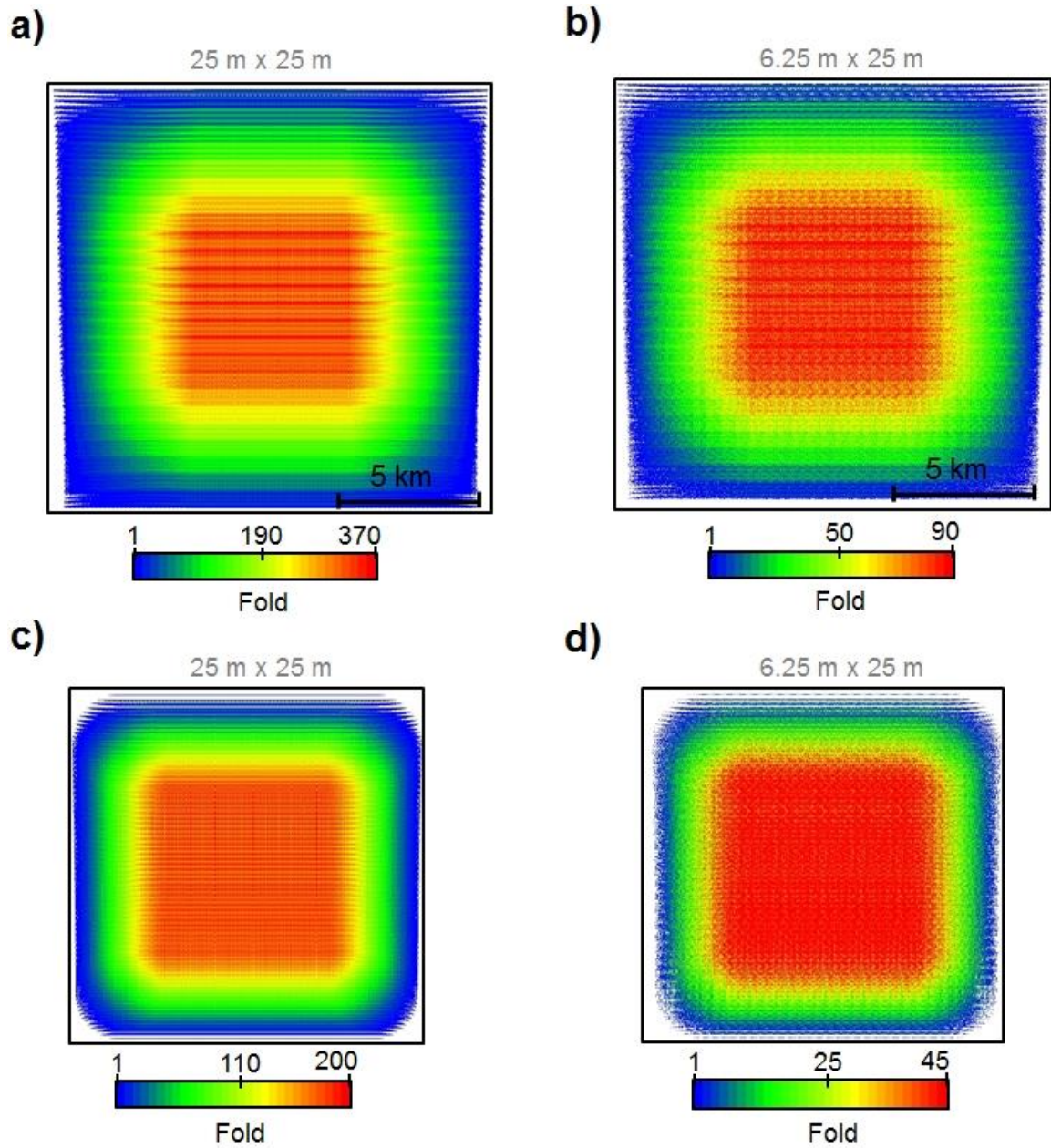


Figure 3.18. PS fold map comparison for different bin sizes, smaller bin size are achieved by the receiver-line stagger, warmer colors indicate higher fold values. (a) PS fold map for using bin size of 25 m by 25 m. (b) PS fold map using bin size of 6.25 m by 25 m. (c) PS fold map, for the offsets between 500 m to 2,500 m, using bin size of 25 m by 25 m. (d) PS fold map, for the offsets between 500 m to 2,500 m, using bin size of 6.25 m by 25 m.



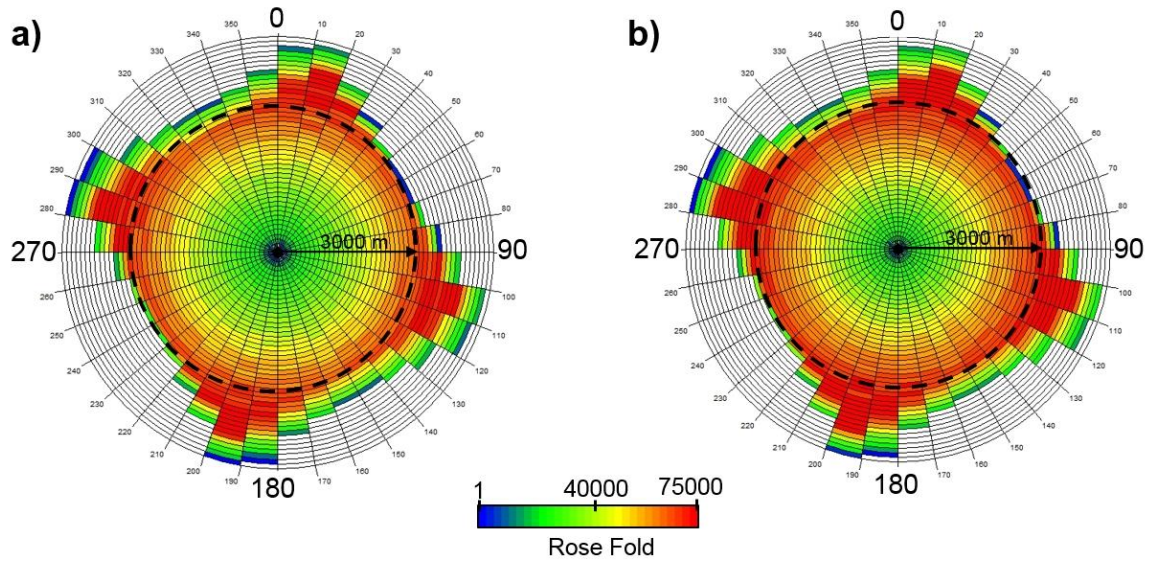


Figure 3.19. Rose plot comparison for all the offsets using different bin sizes, smaller bin sizes are achieved by the receiver-line stagger. (a) 25 m by 25 m bin size. (b) 6.25 m by 25 m bin size.

### 3.3.5 Alternative design, slanted-shot lines with receiver-line stagger

Land seismic survey designs are mostly acquired with orthogonal surveys. Orthogonal lines are geometrically and perhaps operationally more straightforward. The slanted design can be described as the modified orthogonal geometry (where shot and receiver lines are no longer  $90^\circ$  apart, but at say  $45^\circ$ ). It was suggested that the slanted geometry could provide “better distribution of the sparse offsets across the total offset range for bin, thus reducing the geometry imprint” (Vermeer, 2012).

To test the effectiveness of the slanted design, we made some modifications to the original orthogonal geometry and re-calculated the PS illumination maps. Figure 3.20 shows the

updated geometry with the some of the design parameters. One of the drawbacks with the updated geometry design was increased station spacing. We managed to keep the total number of shots somewhat similar, although the shot spacing increased from 50 m to 70 m. The increase of the shot spacing can introduce some artifacts during the migration process; however, we believe the artifacts should be minimized due to the strong fold coverage for most of the survey area.

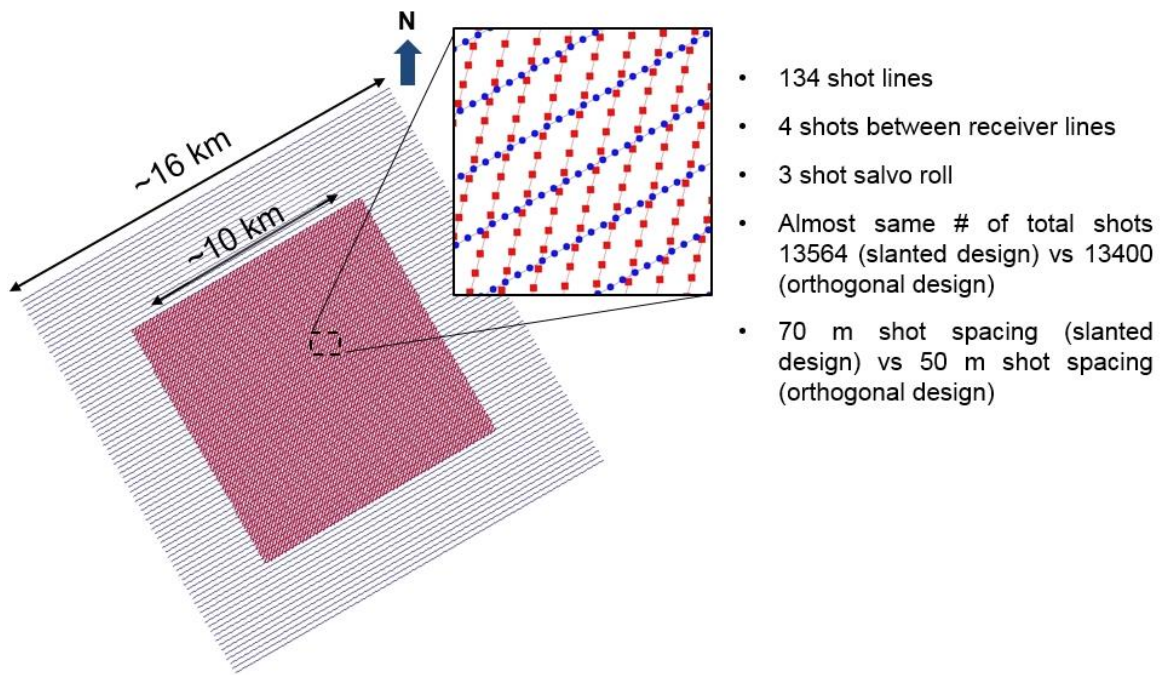


Figure 3.20. Multicomponent survey layout with slanted-shot lines ( $45^\circ$ ), blue lines represent the receivers and the red lines represent the shots.

Figure 3.21 shows the PS fold maps for both orthogonal and the slanted-shot line geometry. The PS fold map for the slanted-shot line geometry appears similar with a slightly better fold coverage, compared to the orthogonal geometry. However, the near offsets (0-500 m) contains lesser trace distribution, for the slanted shot design, due to increased shot spacing. The rose plot results indicated much smoother azimuth/offset distribution of the traces across all the offsets for the slanted shot design. We also investigated the illumination results for the offsets between 500 m to 2,500 m (Figures 3.21c and 3.21d). It appeared that the fold and trace/azimuth distribution for the selected offset yielded results without any irregularities or fold striping. Further analyses may be required by obtaining synthetic data over a simple model to examine the effects of the station spacing over the migrated sections.

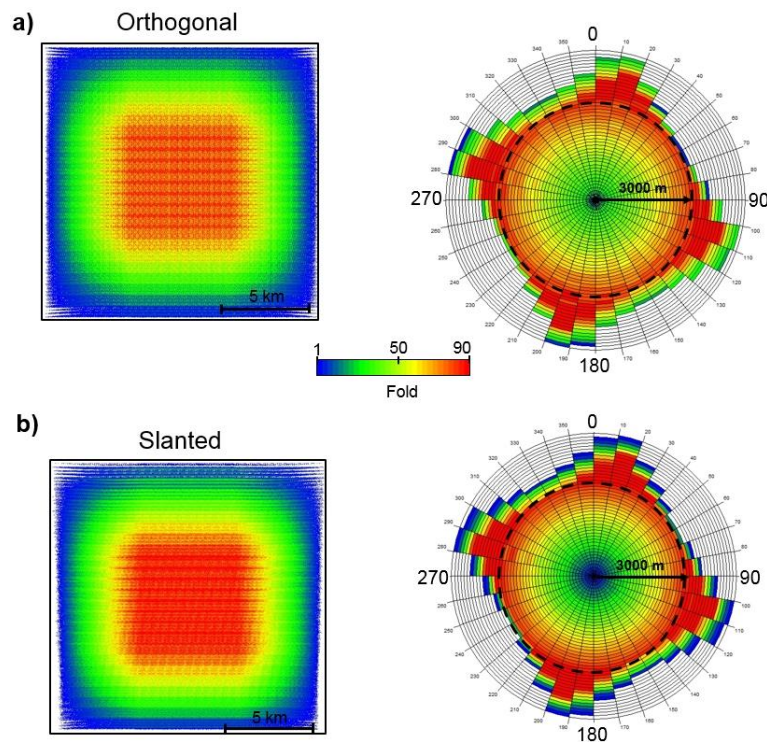


Figure 3.21.

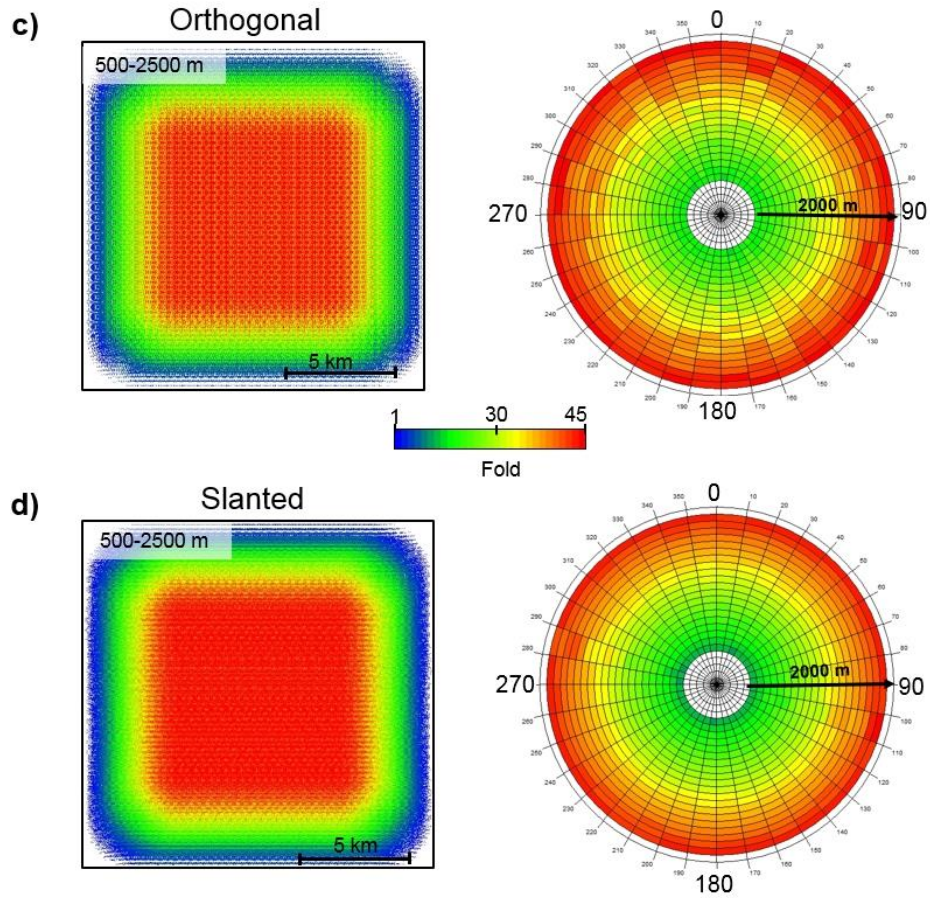


Figure 3.21.cont. PS fold map and azimuth/offset distribution (shown as rose plot) comparison between orthogonal and slanted-shot line geometry. Both surveys has receiver-line stagger to achieve 6.25 m by 25 m bin sizes. Warmer colors indicate higher data values. (a) PS fold and rose plot map for the orthogonal geometry. (b) PS fold and rose plot map for the slanted-shot line geometry. (c) PS fold and rose plot map for the orthogonal geometry between 500 m to 2,500 m offsets. (d) PS fold and rose plot map for the slanted-shot line geometry between 500 m to 2,500 m offsets.



### 3.4 Conclusions

Survey design is one of the critical aspects of 3C-3D seismic surveys. We completed design studies to better understand the requirements for multicomponent surveys. The first survey generated for the purpose of testing the design parameters and their effects over the seismic attribute distribution for both PP and PS surveys. Simple designs for the test studies included either 11 receiver lines and 24 shot lines (receiver centered on source grid) or 24 receiver lines and 11 shot lines (shots centered on receiver grid). The illumination target selected at 1,600 m depth. These test studies showed that PP illumination results do not necessarily guarantee the achievement of similar PS illumination results.

The trajectory of the common conversion point (CCP) often is the main factor for the PS illumination quality. Increased  $V_P/V_S$  values enhanced the shifting of the CCP towards the receiver lines and resulted in some unwanted imprints. However, the trajectory actually moved the CCP's away from the receivers for increased depth. Therefore deeper targets provided more concentrated illumination maps with limited fold striping.

3D test geometry favored the shot lines centered over the greater receiver grid as it provided broader coverage. However, if the subsurface target is areally limited, centered receiver lines over the shot grid may provide more beneficial solutions, as the illumination would be mostly concentrated over the area of interest rather than the full subsurface horizon. Compared to the parallel geometry, we obtained better distributed seismic attributes from

slanted and orthogonal geometries. Parallel geometry resulted in limited seismic coverage and fold striping for the both PP and PS studies.

The dip analyses over the subsurface target revealed that the illumination moved in an updip direction and higher fold were concentrated in downdip. The updip movement of the illumination increases with the amount of dipping, therefore extended offsets (additional receivers) were required to fully capture the seismic data. Additional receiver lines were mostly advantageous when they were placed towards the updip, rather than downdip.

Receiver-line stagger allowed the reduction of inline bin size from 25 m to 12.5 m hence increasing the seismic data resolution. Even though the amount of prestack traces doubled, the operational costs of the receiver-line stagger is limited and the outcomes appeared promising.

Required surface recording time is determined over the simple 2D model for various seismic velocities and dipping target layer. To fully capture the converted-wave-field, for a survey at this scale, with maximum of 30° subsurface dip, at least five seconds long seismic data is required.

A full sized 3C-3D survey design is completed over 250 km<sup>2</sup> area. The acquisition contained an orthogonal geometry with shot lines centered over the greater receiver grid.

For the operational purposes a selection was made to use three shot salvos. The effect of shot salvo was observed as east-west trending stripes in the fold map. One of the fundamental goal for the multicomponent survey was to achieve the 6.25 m by 25 m bin sizes and the smaller bin sizes were achieved by receiver-line stagger. The staggered helped to achieve seismic attribute without any evidence of fold striping and smooth distribution of traces across the all offsets/azimuths were observed. The existence of the longer offsets, due to the greater receiver grid, assured the proper illumination of a target horizon with a  $5^{\circ}$  dip towards the Southwest.

An alternative design was proposed by modifying the orthogonal geometry (shot and receiver lines that are  $45^{\circ}$  apart). The slanted geometry, for a  $5^{\circ}$  dipping target produced improved seismic attribute distributions at all offsets when compared to the original orthogonal geometry. Some of the acquisition footprints were seen over slanted geometry as well, however the footprints were mainly based on the salvo shot rolls; and the imprint can be improved by reducing the number of salvos. We believe that the illumination can be further improved by reducing the receiver line interval, without causing significant increase in survey costs.

## **Chapter 4**

# **Near-Surface Geophysical Investigation of the 2010 Haiti Earthquake Epicentral Area: Léogâne, Haiti**

### **4.1 Introduction**

On January 12, 2010, the area of Port-au-Prince, Haiti, and a zone extending some 30 km westward from Port-au-Prince was severely shaken by a magnitude 7.0 earthquake. Initial evaluations proposed that fault rupture occurred on the nearby and geomorphically conspicuous, active, left-lateral strike-slip, plate boundary fault (Mann et al., 1995) - the Enriquillo Plain Garden fault zone (EPGFZ) shown in Figure 4.1. In the aftermath of the 2010 earthquake, detailed studies (Calais et al., 2010; Hayes et al., 2010; Prentice et al., 2010; Hashimoto et al., 2011; Douilly et al., 2013) proposed that the main slip of the 2010 Haiti earthquake actually occurred on a previously unrecognized, north-dipping reverse fault, named the Léogâne fault that was a separate fault from the adjacent and steeply south-dipping EPGFZ. Aftershocks indicated that coseismic, north-dipping reverse motion on the Léogâne fault zone occurred at a depth of about 4 to 18 km beneath the surface of the Léogâne fan-delta (Douilly et al., 2013).



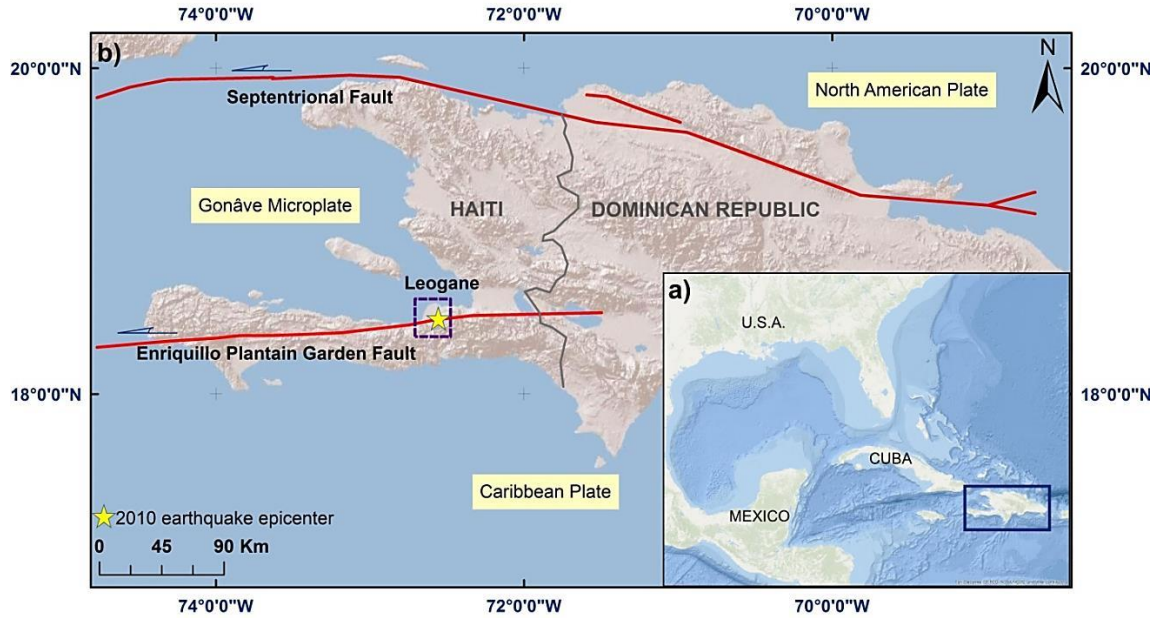


Figure 4.1. (a) Location of the island of Hispaniola (inside the blue box) in the northern Caribbean. (b) Active, left-lateral strike-slip faults shown in red in the Hispaniola region separating the Gonâve microplate from the larger North America plate to the north and Caribbean plate to the south (modified from Calais et al., 2010). The dashed square indicates the location of the study area of the Léogâne fan-delta. The yellow star indicates the epicentral location of the 2010 earthquake from Douilly et al. (2013).

While no surface rupture has been identified along either the EGPFZ or on other surface faults crossing the Léogâne fan-delta or in surrounding areas (Prentice, et al., 2010; Cowgill et al., 2012), widespread shaking and surface deformation of the Léogâne fan-delta was manifested by: 1) broad-scale destruction of buildings built on the Léogâne fan-delta, 2) coastal uplift of coral reefs deformed along an east-west axis (Hayes et al., 2010), 3) coastal submarine slumps accompanied by localized tsunamis (Hornbach et al., 2010), 4) liquefaction in coastal areas of the western fan-delta, 5) a 2 km long, east-west axis of coseismic cracking of a north-south paved highway crossing the fan (Rathje et al., 2010;

Koehler and Mann, 2011; Bilham and Fielding, 2013), and 6) an east-west axis of coseismic uplift inferred from interpretations of radar interferograms taken from satellites of the Léogâne fan-delta (Hashimoto et al., 2011; Bilham and Fielding, 2013).

To our knowledge, there has been no land reflection seismic survey in Haiti prior to this study of the Léogâne fan-delta. Various remote sensing surveys have been combined with seismic and gravity data to better understand the complex subsurface structures activated by the 2010 Haiti earthquake in the Léogâne fan-delta area.

We undertook near-surface geophysical methods to investigate the subsurface in the Léogâne fan-delta (Dowla et al., 2012; Kocel et al., 2014) in the area of maximum coastal uplift, highway damage, and aftershock clustering. Our reflection lines used north-south-oriented country lanes to collect reflection data at right angles to the east-west-trending axis of coseismic uplift and intense shaking that connected the area of maximum coastal uplift to the zone of cracking observed along the north-south highway (Bilham and Fielding, 2013).

The primary goals of this imaging were to: 1) measure near-surface sediment properties, 2) image the near-surface structure, and 3) attempt to reveal the proposed blind thrust fault (Léogâne fault) thought to lie below the Léogâne fan-delta. In this study, results from

ultrasonic laboratory measurements, surface seismic, and gravity analyses were integrated to examine the potential causes and effects of the earthquake in the Léogâne fan-delta area.

#### 4.2. Geological settings of Haiti and the 2010 Haiti earthquake epicentral area

Haiti occupies the western one-third of the island of Hispaniola and is located on the Gonâve micro-plate. This rectangular-shaped Gonâve micro-plate is bound by two major strike-slip fault zones that separate it from the North America plate to the north and the Caribbean plate to the south (Mann et al., 1995; Benford et al., 2012).

On average, Hispaniola experiences at least one major earthquake ( $> M 7.0$ ) every 50 years (NEIC, 2014). Records from previous historical earthquakes in Hispaniola date back to the European discovery and settlement 500 years ago in the 16th century. In 1701, a major historical earthquake estimated at magnitude of 6.6 shook the same region of the Léogâne fan-delta as the 2010 Haiti earthquake with similar patterns of collapsed buildings, liquefaction and coastal slumps (Bakun et al., 2012).

The Léogâne fan of southern Haiti is the largest subaerial fan-delta in the Caribbean region (Figure 4.2). The fact that the delta is exposed onland rather than in an offshore shelf setting indicates the possibility of longterm tectonic uplift related to the Léogâne fault, the EPGFZ, or both faults (Taylor et al., 2011). Hashimoto et al. (2011) used satellite radar data to

show that the surface deformation related to the 2010 earthquake does not correspond to the present topography: the Léogâne fan-delta north of the EPGFZ was uplifted whereas mountains south of the EPGFZ subsided (Figure 4.3).

Immediately after the earthquake, field observations confirmed that no primary surface ruptures along the main EPGFZ in the Léogâne area, or within the Léogâne fan-delta itself (Koehler and Mann, 2011; Bilham and Fielding, 2013). Satellite-based surface-deformation results (InSAR) combined with the location of the main shock and its aftershocks also supported the interpretation that the main 2010 earthquake was not accommodated by simple, left-lateral strike-slip displacement on the EPGFZ (Calais et al., 2010; Hayes et al., 2010; Hashimoto et al., 2011; Bilham and Fielding, 2013). Instead, these interferograms along with the field observations of the coral reef along the western coastline of the Léogâne fan-delta indicate a 14 km wide and 4 km long east-west axis of coseismic uplift extending into the Léogâne fan-delta, 2 km north of the surface trace of the EPGFZ (red dashed line in Figure 4.3). Surface deformations were also noted along a paved north-south highway crossing the epicentral area. Intense cracking of the highway aligns with the zone of maximum coastal uplift, and is consistent with a temporary, coseismic uplift of the ground surface (Bilham and Fielding, 2013).

Recorded aftershock events delineated a coherent reverse dipping towards the north at an angle of  $60^{\circ}$  to  $70^{\circ}$  and located several kilometers north of the EPGFZ. The aftershock results are in general agreement with models of the coastal uplift also predicting the presence of a blind, north-dipping reverse fault. Selected aftershock events, kindly

provided by R. Douilly, J. Haas and E. Calais, in the area of our seismic survey were used to estimate the depth of faulting beneath the survey area (as discussed later).

Figure 4.3 shows coseismic uplift by as much as 0.6 m of the coastal reef, 500 m west of our area, and proposed coseismic deformation of the north-south highway 3,000 m east of our area. A pre-earthquake aerial photo taken of the submerged reef about 100 m from the shoreline in 2005 is compared to the uplifted reef from a post-earthquake photo taken in 2010. White circles represent the aftershock locations on the southern part of the Léogâne fan. It is clear from the map in Figure 4.3 that most of the coseismic deformation was concentrated in an east-west belt ~2 km north of the EPGFZ.

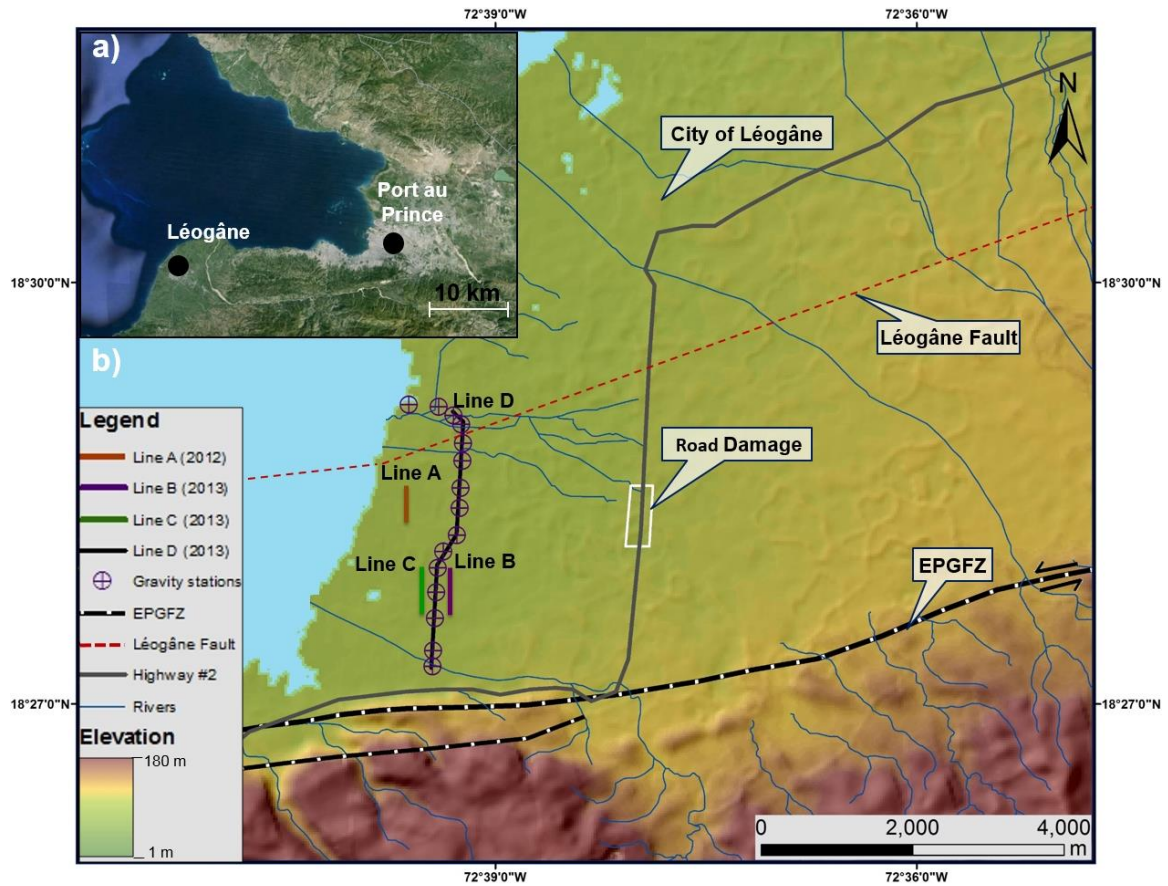


Figure 4.2. (a) Location of the Léogâne fan-delta, 30 km west of the capital city of Port-au-Prince. (b) Digital elevation map of the southwestern Léogâne fan-delta showing the locations of the seismic reflection lines described in this paper: Line A was collected in 2012 using a sledge hammer source; seismic data along Lines B, C, and D were collected in 2013 using the accelerated weight drop. Warm colors indicate higher elevations (about 180 m) and cooler colors indicate low elevations. Enriquillo Plantain Garden Fault Zone (EPGFZ) is drawn with black and white dashed line. Red dashed line represents the proposed (Douilly et al., 2015) geometry for the Léogâne fault.

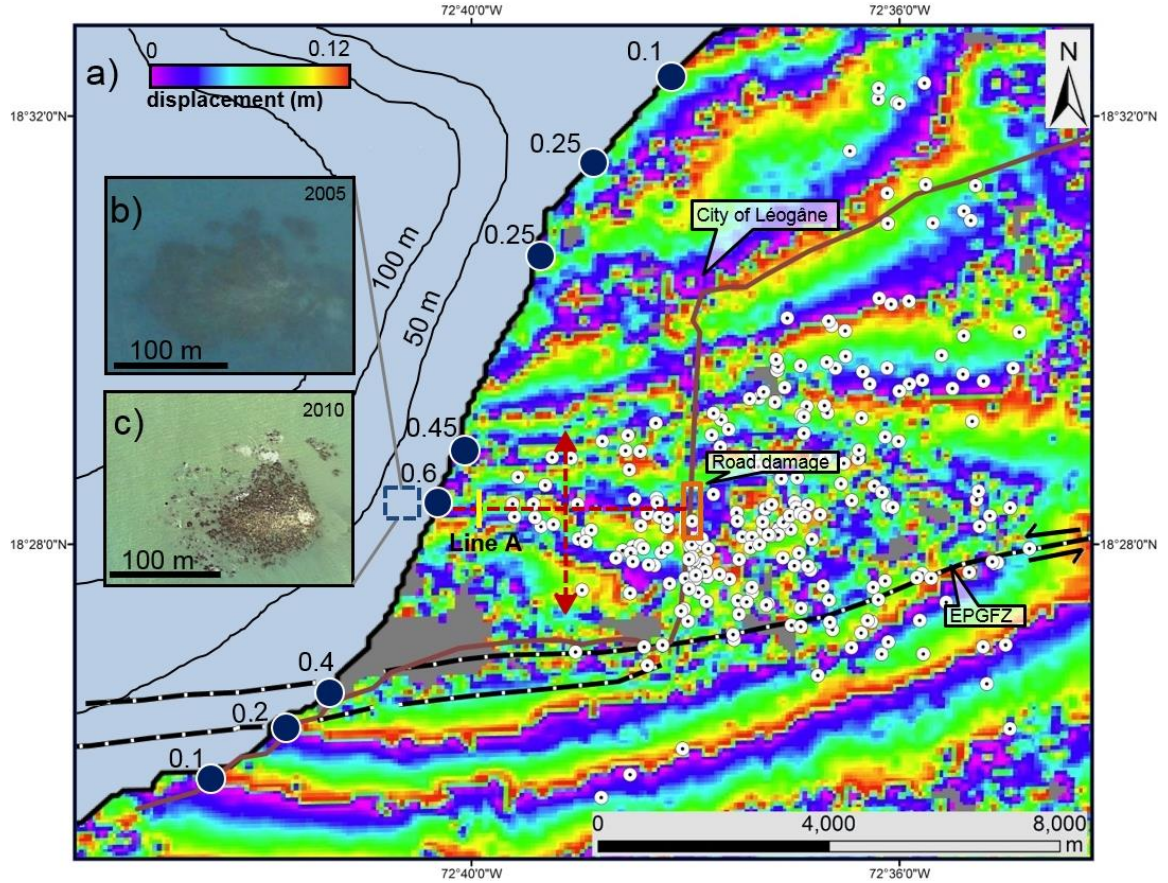


Figure 4.3. (a) The deformation observation of the Léogâne area along with the interferogram and bathymetry map (shown as contour lines). White circles show the aftershock locations (Douilly et al., 2013). The black and white dashed line in the south represents Enriquillo Plantain Garden Fault Zone (EPGFZ) and interpreted folding axis is shown with red dashed line. (b) Satellite photograph of coral reef off the coast of the Léogâne fan-delta before the earthquake (from Google Earth, 2005). (c) Satellite photograph of uplifted coral reef after the earthquake (from Google Earth, 2010). Blue dots on the coastline show the amount of coral reef uplift (in meters) during the 2010 earthquake (Hayes et al., 2010).



### 4.3 Data and methods

During our fieldwork in 2013, we acquired ultrasonic velocity and density data on a selected hand samples from several sites. Most of our efforts were concentrated on the seismic surveys and gravity measurements.

Ultrasonic transmission measurements and density measurements were performed on the hand samples to estimate the P-wave velocity ( $V_P$ ), S-wave velocity ( $V_S$ ) and density ( $\rho$ ). These measurements were carried out at the Allied Geophysical Laboratory (AGL) facilities located at the University of Houston.

All of the specifications for the seismic data acquisition are shown in Table 1. Both line B and line C are actually co-located with line D. For the display purposes (Figure 4.2), they are put on each side of line D.

	Survey Type	Year	Source Type	Source Spacing	Geophone Type	Geophone Spacing	Total Length
Line A	P-wave, cable	2012	4.5 kg hammer	5 m	Vertical, 10 Hz	5 m	400 m
Line B	P-wave, cable	2013	40 kg vertical AWD	5 m	Vertical, 10 Hz	5 m	600 m
Line C	S-wave, cable	2013	40 kg tilted AWD	5 m	Horizontal, 10 Hz	5 m	600 m
Line D	P-wave, nodal	2013	40 kg vertical AWD	10 m	Vertical, 10 Hz	10 m	3500 m

AWD: Accelerated weight drop

Table 1. Specifications of seismic lines that were acquired in the 2012 and 2013 surveys over the Léogâne fan delta. The locations of the seismic lines are annotated in Figure 4.2.



The main gravity survey line, 4,000 m long with an average station interval of 300 m was largely co-located with line D (Figure 4.2). At every station, readings were recorded for two minutes and averaged using a Scintrex CG-5 gravimeter. Additional gravity lines were conducted around the Pétionville district and from the city of Jacmel to Léogâne with approximately 1,000 m spacing, for a total of 16 stations.

#### 4.3.1 Laboratory measurements

As mentioned previously, a number of rock hand samples were collected during the 2013 surveys. The rock hand samples are shown in Figure 4.4, including metamorphosed limestone (sample A), sandstone (sample B), and basalt (sample C).  $V_P$ ,  $V_S$ , and  $\rho$  values from these samples are shown in Table 2.

Details about the measurement methodology are provided in Appendix A. The subsurface lithologies in the Léogâne area are currently unknown due to alluvial sediment cover. However, they could include these rock types (as evidenced by exposures in neighboring uplifted areas as well as the samples themselves).

Sample B was collected in an area between Léogâne and Port-au-Prince, north of the EPGFZ whereas both sample A and C were collected around the Furcy area, approximately 20 km southwest of the Léogâne. Among the collected rock samples, the location of sample B was the closest to the surveys over the Léogâne area.

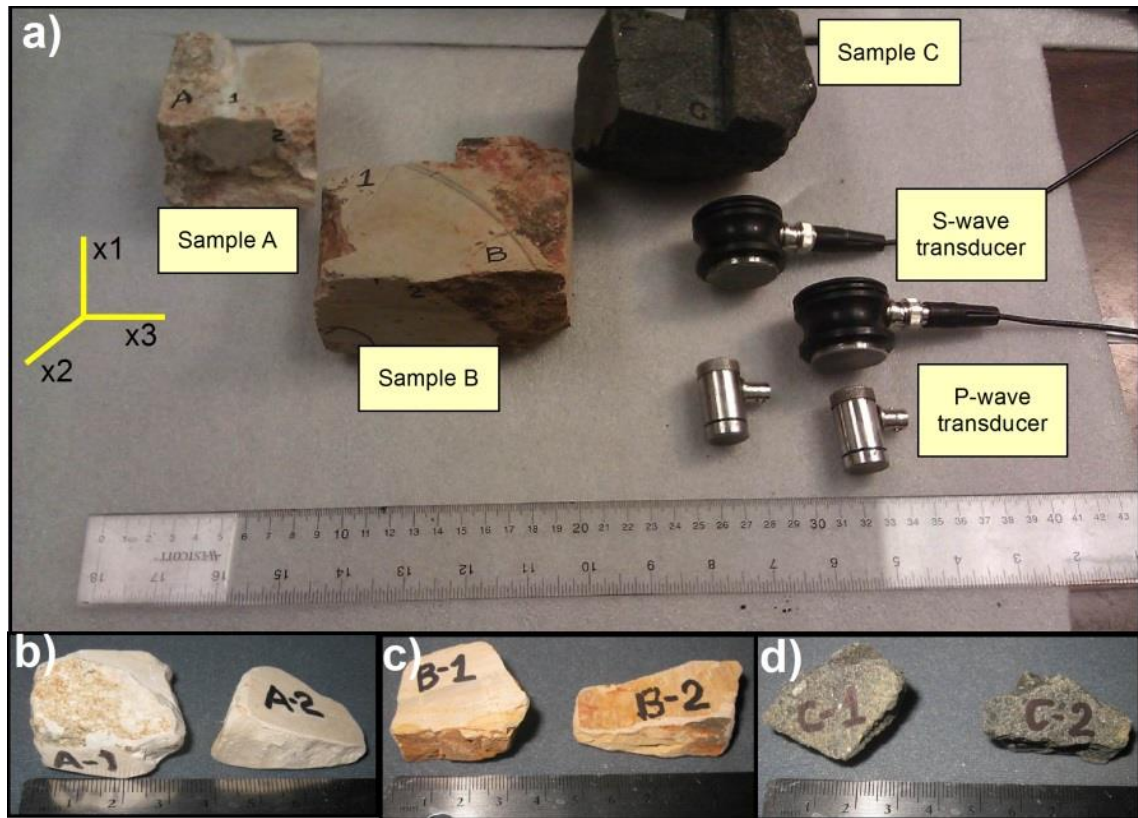
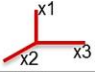


Figure 4.4. (a) Ultrasonic transducers with the rock samples that were used in velocity measurements. Orientation of the axes for the velocity measurements is drawn in yellow. (b) Parts of sample A (limestone) used for density measurements. (c) Parts of sample B (sandstone) used for density measurements. (d) Parts of sample C (basalt) used for density measurements.



	$V_P$ (m/sec)				$V_S$ (m/sec)			$\rho$ (g/cc)
	x1	x2	x3		x1	x2	x3	
Sample <b>A</b> (metamorphosed limestone)	6190	6320	6320		3150	3280	3360	2.64
Sample <b>B</b> (layered sandstone)	2350	2950	2920		1550	1800	1850	2.01
Sample <b>C</b> (fractured basalt)	3520	3400	3430		2080	2105	2110	2.36

Table 2. Summary of ranges of P-wave and S-wave velocities from ultrasonic laboratory measurements and their calculated density values for the collected hand samples.

#### 4.3.2 Seismic surveys

Sample shot gathers from different seismic surveys are shown in Figure 4.5. Analysis of the first refracting arrivals gave velocities of about 1,800 m/s. These values are in a typical velocity range for saturated, unconsolidated sediments (Barton, 2006). The air-blast velocity was around 345 m/s. Low frequency ( $< 20$  Hz), and low velocity events ( $< 250$  m/s) were interpreted as surface-waves. The frequency spectra of seismic sources, such as hammer and accelerated weight drop, indicated more energy in the weight drop (Figure 4.6). The AWD system contained a slightly broader frequency spectrum range as well.

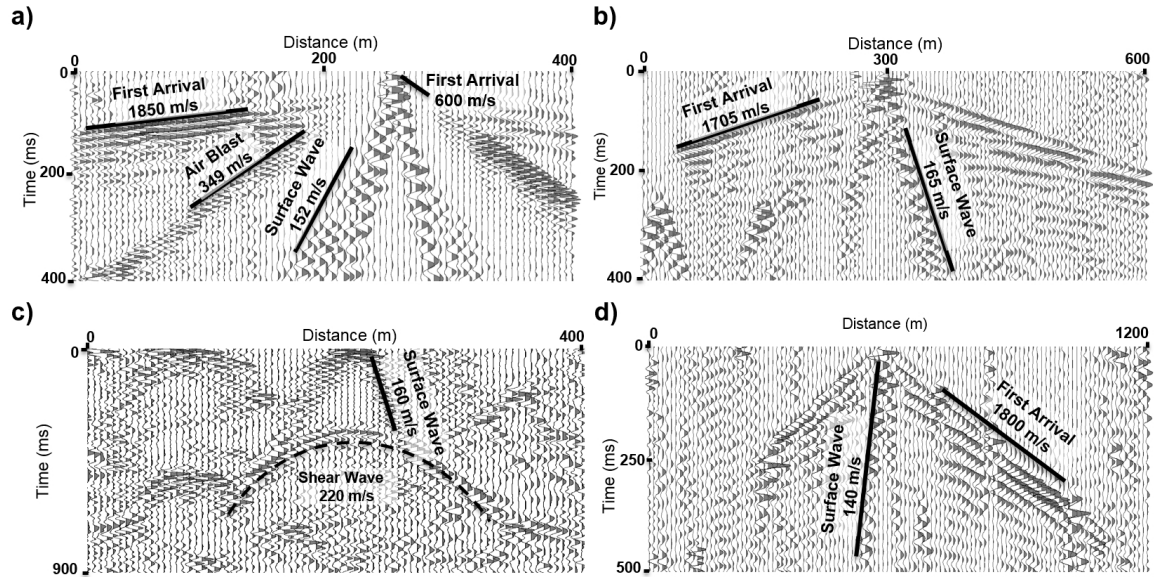


Figure 4.5. Representative seismic shot gathers (with AGC scaling) from vertical geophones. (a) Line A (4.5 kg hammer source). (b) Line B (40 kg accelerated weight drop). (c) Line C (tilted 40 kg accelerated weight drop). (d) Line D (40 kg accelerated weight drop). First arrival, surface-wave, and air-blast velocities are annotated. Dominant frequencies are approximately 50 Hz.

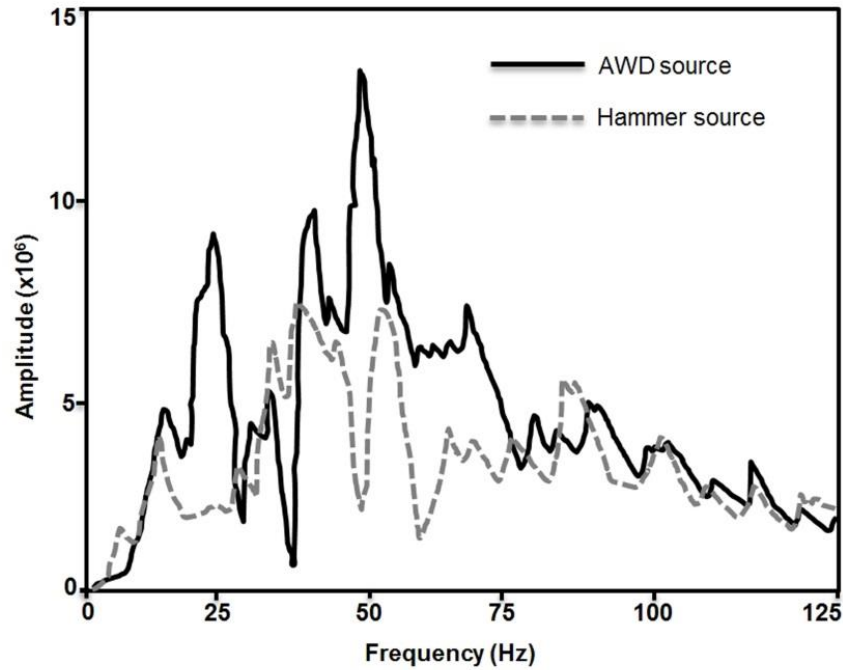


Figure 4.6. Comparison of true amplitude spectra for seismic line A (hammer line), and seismic line B (accelerated weight drop).

The 2D P-wave velocity structures for line A and B were determined by travelttime tomography using first-break picks. P-wave velocities were estimated between 500 and 2,250 m/s for an 80 m deep model (Figure 4.7). The tomography results indicate south dipping layers with a thickening of the low-velocity layers toward the southern end of the model. A similar trend was observed with the stacking velocity analysis of seismic lines (discussed in the next section). Velocity models suggested the top 20 to 50 m of the subsurface contained seismically weak layers. For the remainder of the model, the velocities were around 2,250 m/s.

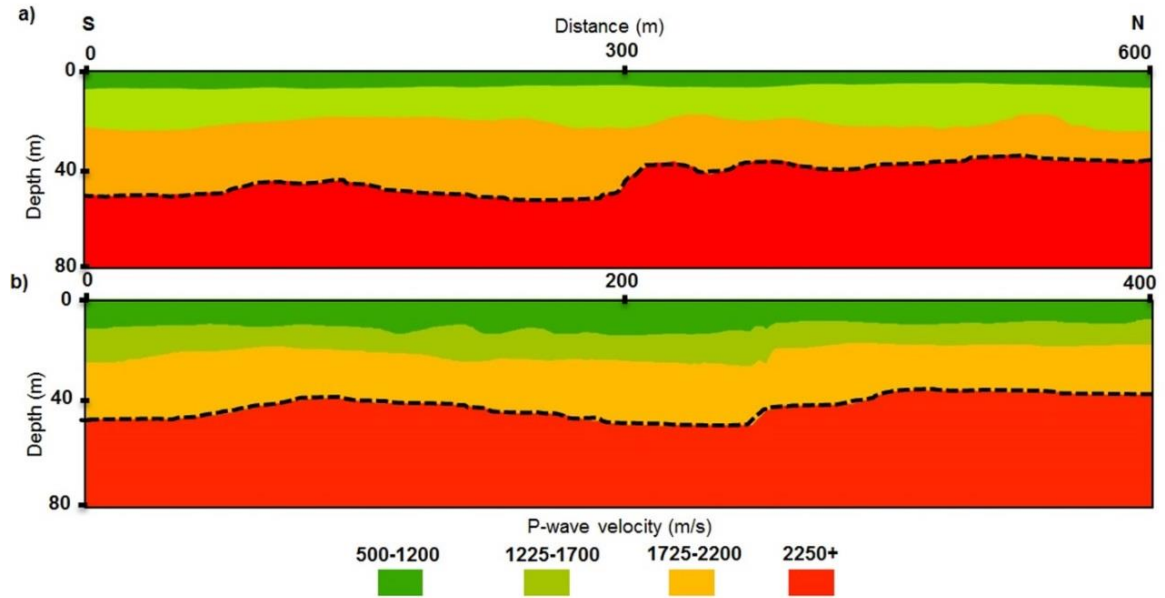


Figure 4.7. P-wave travelt ime tomography results. (a) Line A: P-wave velocity section using an 80 m deep model. (b) Line B: P-wave velocity section using an 80 m deep model. The red color represents relatively higher P-wave velocities (2,250 m/s), and the green color represents slower P-wave velocities. Strata above the black dashed line are relatively slow and interpreted as seismically weaker layers.

To estimate the near-surface shear-wave velocity structure and classify near-surface soil, the surface-wave inversion method was applied to obtain S-wave velocities, using the Multichannel Analysis of Surface-waves (MASW, Park et al., 1999; Xia et al., 1999). This method is based on the generation of phase velocity versus frequency plots, known as dispersion curves, due to the frequency dependence of the S-waves. Resulting dispersion curves are then inverted for the fundamental modes to generate shallow S-wave velocity ( $V_s$ ) structures. The selection of the appropriate receiver spread length and offset is critical for the final image. As the ground roll is dispersive, the near offsets and far offsets were carefully selected (Park, 2011; Roy and Stewart, 2012).

For each shot, the most appropriate receiver spread was found to be 15 to 150 m for line D, 10 to 70 m for line B, and 15 to 65 m for line A. The next step was to invert the dispersion curves to generate an S-wave velocity section. The final  $V_s$  images obtained from the seismic lines are shown in Figure 4.8. Line A was located ~500 m from the coast, and its resulting S-wave velocities are much lower when compared to line B and line D. The gentle folding of the shallow strata and relatively steeper and southward dipping layers were observed in parallel with the area of maximum coastal uplift and damage to the north-south paved highway. The anomalous, elevated velocity zone that was observed on line B and line D may be indicative of a channel body from a previous fan surface (coarser clasts from surrounded and eroded bedrock areas of limestone may result in relatively higher velocities).

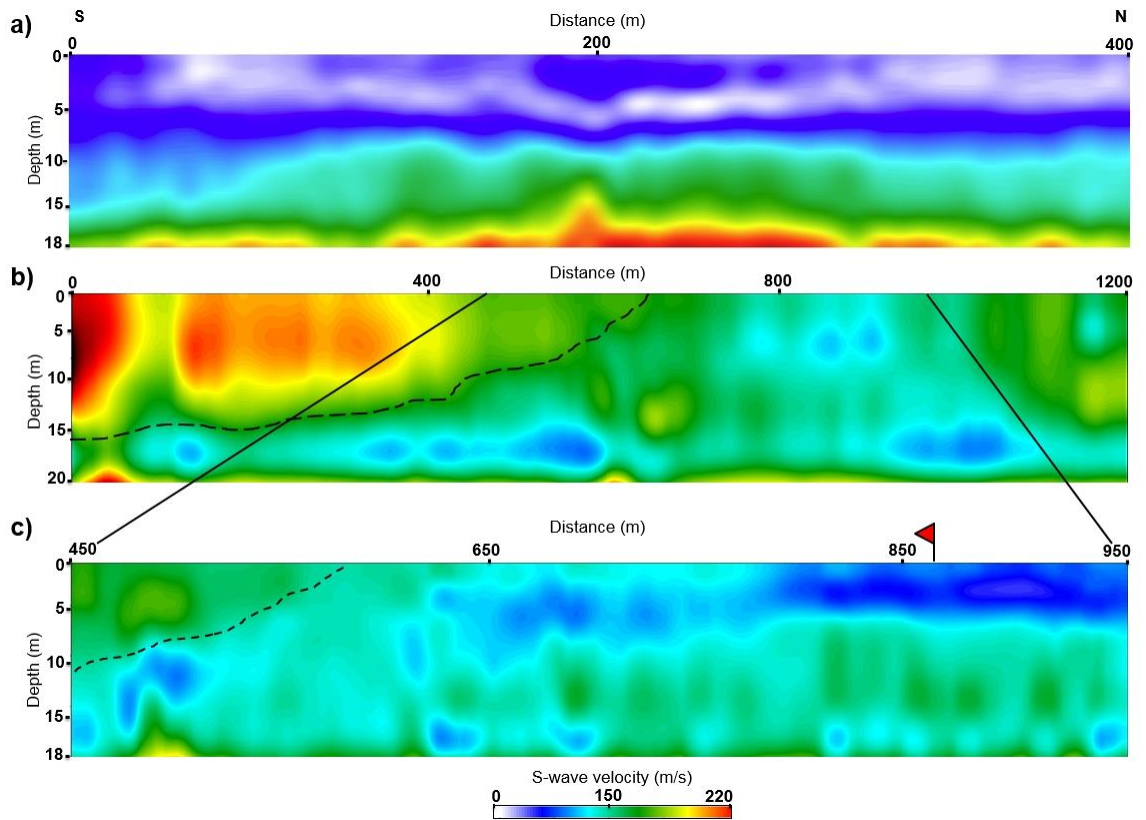


Figure 4.8. The 2-D S-wave velocity profiles determined from surface-wave inversion. (a) Velocity profile for line A. (b) Velocity profile for line D. (c) Velocity profile for line B. Red colors represent velocities around 200 m/s. Dashed lines indicate a high-velocity structure over a low-velocity region. The shot location for the S-wave reflection gather (Figure 4.9) is shown with a flag.

Most of the S-wave reflection data is very noisy. The data from a selected shot record, with interpreted S-wave reflections are shown in Figure 4.9 (location given in Figure 4.8 with a red flag). Velocity analyses over semblance indicated a range of S-wave velocities between 210 and 240 m/s, and these reflectors appear around 40 to 50 m depths. These deeper S-wave velocities were comparable to the shallower velocities obtained from the surface-wave inversion. The depth of the observed reflectors correlated with the 2,250 m/s velocity contact observed in seismic refraction models. Integrated results for the near-surface S-



wave studies are shown in Figure 4.10. The red line represents a single 1D S-wave velocity profile that was estimated and extended to a deeper depth via interval velocities from a shot gather over line C.

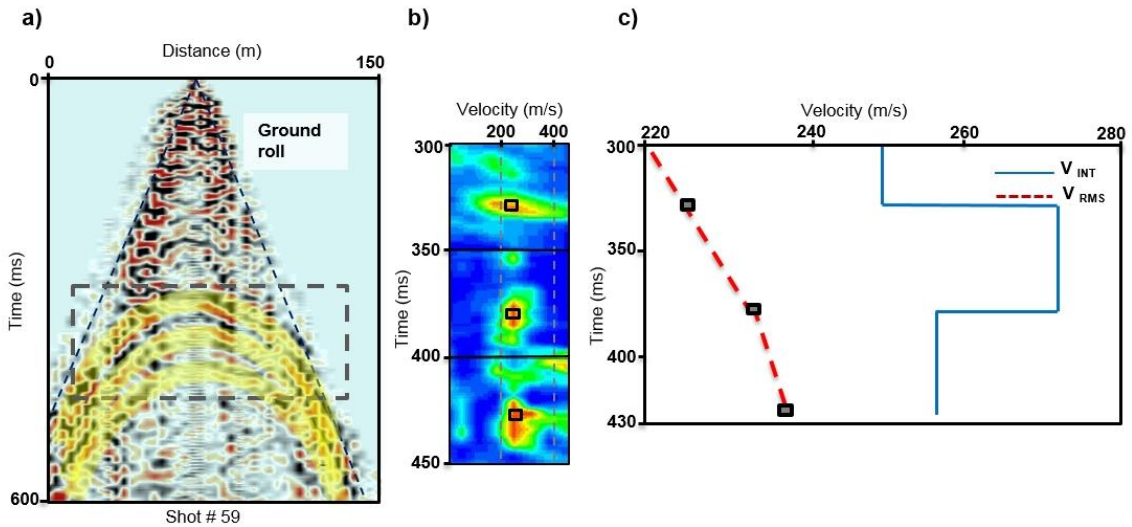


Figure 4.9. Analyses of S-wave source and horizontal receiver shot gather from line C showing S-wave reflections. (a) Selected shot gather, reflected signals highlighted in yellow. (b) Velocity semblance for the dashed box area. Black boxes indicate the picked stacking velocities. (c) Dix interval velocities calculated from the stacking (as RMS) velocities. These are interpreted as pure shear velocities.

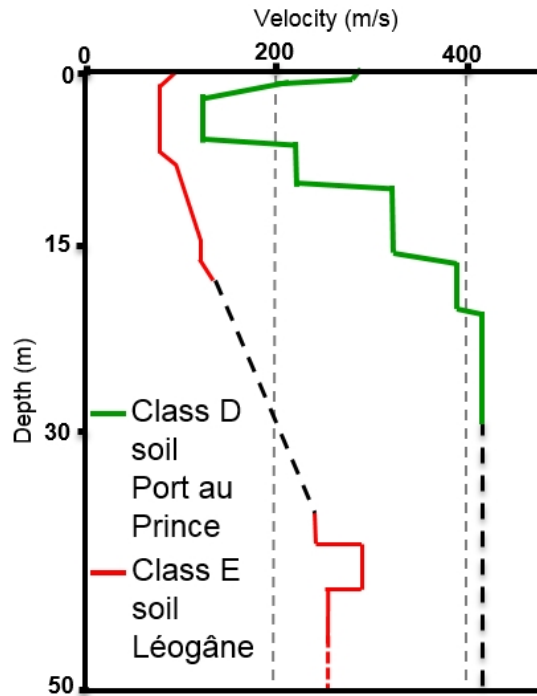


Figure 4.10. S-wave velocity profiles for Port-au-Prince (from Cox et al., 2011) and Léogâne (Surface-wave inversion results for the first 18 m combined with a shot gather from line C). Note that the Léogâne near-surface sediments have considerably lower velocities than the Port-au-Prince area near-surface sediments.

Processed results from the P-wave reflection data collected along line A are shown in Figure 4.11. The time-migrated seismic image includes spiking deconvolution and a band-pass filter (20 to 100 Hz). The migrated section, revealed some coherent reflections up to 400 ms (approximately 250 m depth). In the case of line B (Figure 4.12), the time-migrated section includes band-pass filter, 20 to 95 Hz, spiking deconvolution and noise attenuation. The final image revealed reflections up to 500 ms (approximately 350 m). A strong reflection was observed around 90 ms. The depth of the reflector (at approximately 50 m depth) correlated well with the boundary observed on P-wave refraction and S-wave reflection studies.

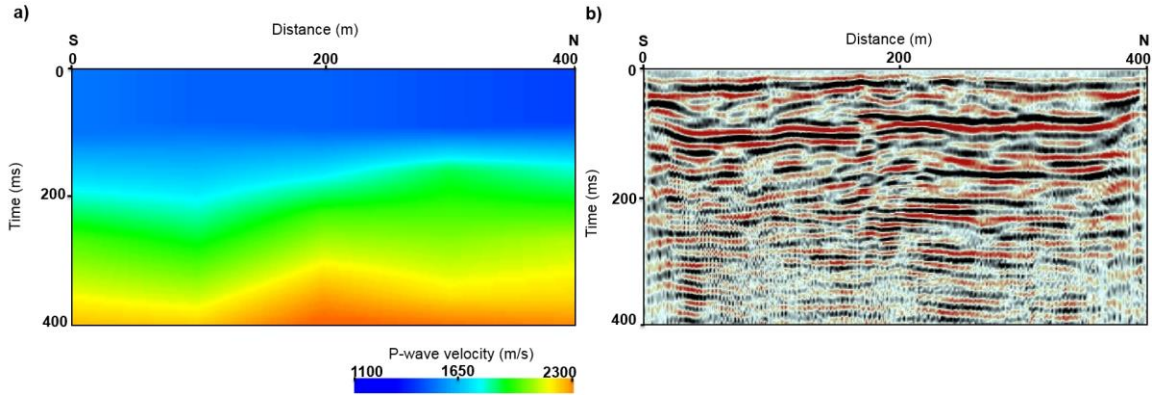


Figure 4.11. Line A seismic reflection data. (a) P-wave stacking velocity section. (b) Time-migrated seismic section.

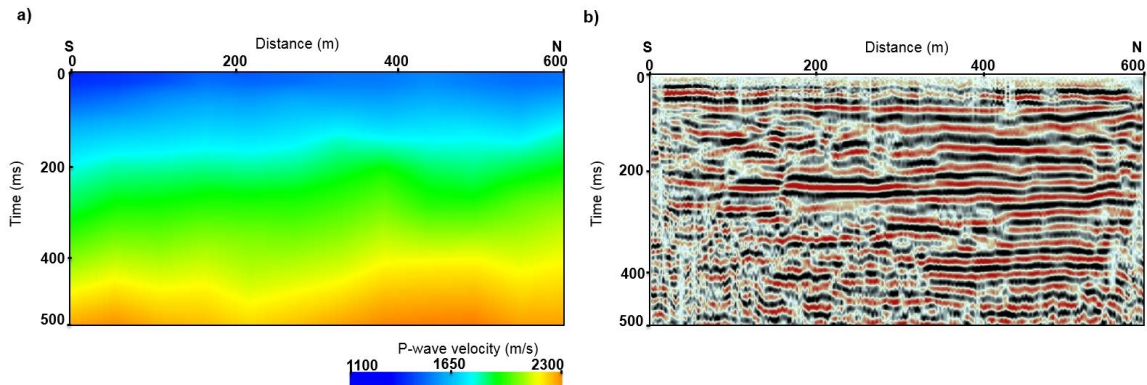


Figure 4.12. Line B seismic reflection data. (a) P-wave stacking velocity section. (b) Time-migrated seismic section.

Analysis of the sub-section from line D revealed deeper reflections with wider offset coverage. This sub-section was selected due to co-location with line B. Coherent energy is in evidence to about 600 ms (approximately 450 m). To enhance the data, noise attenuation and  $f$ - $x$  deconvolution were applied to the final section. In Figure 4.13, the time-migrated image is shown for line D, overlain with the section from line B (separated by a blue dashed

box). Some of the prominent reflections were tracked over both sections, suggesting some reliability. The tracked reflection suggests an average of a  $2^\circ$  dip of the near-surface layers towards the south.

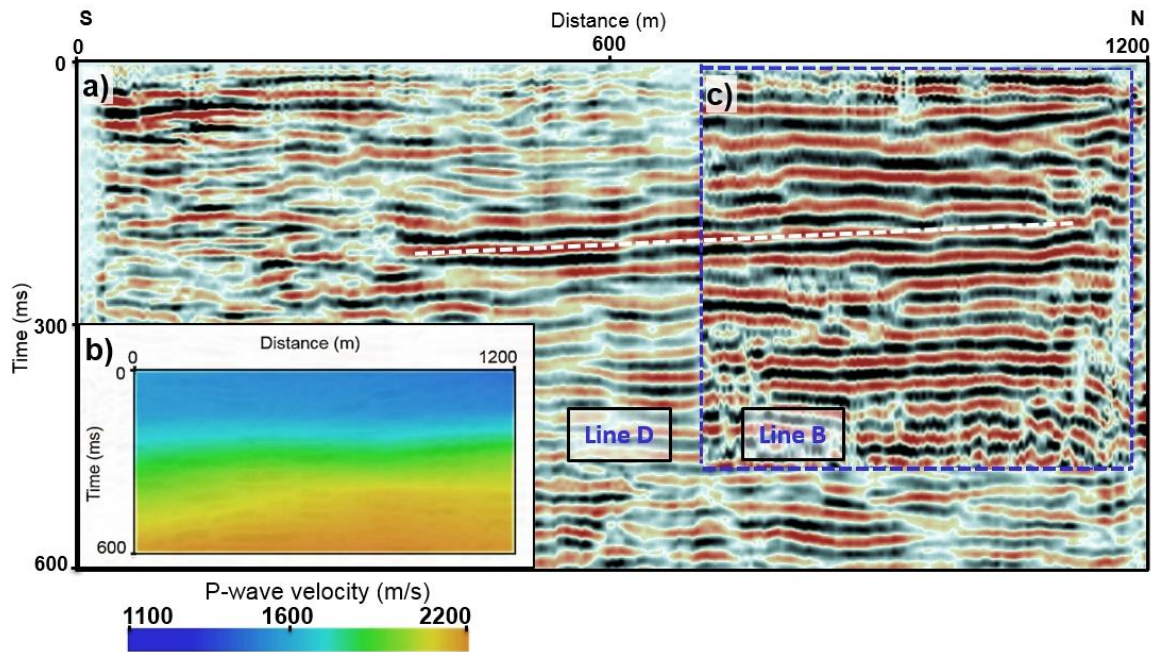


Figure 4.13. (a) Time-migrated seismic section of line D. (b) P-wave stacking velocity section for line D (c) Time-migrated seismic section of line B. AGC is applied on both seismic sections for display purposes. Note the reasonable correlation of the two seismic images. The white dashed line represents an approximate  $2^\circ$  dip of the layers toward the south.

#### 4.3.3 Gravity data

Due to the limited spread of the gravity line over the Léogâne fan (approximately 4,000 m), we expected to have a depth of investigation of less than 2,000 m. The free-air gravity anomaly over the survey area suggests a northward decrease of the gravitational field away from the EPGFZ followed by an increase of the gravitational field for the last 1,500 m at

the northernmost end of the survey (Figures 4.14a and 4.15). Localized variations of the gravity readings could be due to channeling and rapid lateral facies changes.

#### 4.4 Interpretation and discussion

Velocity models obtained from the seismic refraction and reflection studies show a regional dip of low-velocity layers southward towards EPGFZ (Figures 4.7 and 4.11). The boundary between the upper, seismically low velocity layers and underlying strata appeared to be around 50 m. A strong reflection caused by this boundary can also be seen on both S-wave reflection data as well as P-wave reflection data (Figures 4.9 and 4.11). P-wave seismic velocities of the layers, below 50 m depth, appeared to be about that of sample B which was collected close to the survey area.

S-wave velocities are widely used in geotechnical studies and can be used for soil classification. Calculated S-wave velocities do not penetrate deep enough to do comprehensive  $V_s^{30}$  analyses; therefore the results from surface-wave inversion were integrated with a shot gather from S-wave line (Figure 4.10). The S-wave studies from line B indicated an average S-wave velocity of 150 m/s for the top 18 m. For the area between 30 to 50 m, the average S-wave velocity is estimated to be 240 m/s. With an assumption of a linear velocity increased with depth, we estimated an average S-wave velocity of 180 m/s for the first 30 m (Figure 4.10). These velocity values suggest that the near-surface soil at Léogâne fan is most likely class-E type soil (NEHRP, 2014). The class-E soil is more susceptible to ground shaking during an earthquake and can result in liquefaction (NEHRP,

2014). The unconsolidated, soft, seismically low velocity soil may have been a contributing factor for the devastation in the area. Figure 4.10 also compares the S-wave results from the Léogâne area to the recent microzonation study over the Port-au-Prince and surrounding areas (Cox et al., 2011). The resulting soil classification for the specific location at Port-Au-Prince was found to be class D (Cox et al., 2011). The variation of the S-wave velocities may be due to weaker soil conditions over the Léogâne area as compared to the more lithified sedimentary rocks upon which the city of Port-au-Prince is constructed (Rathje et al., 2010).

Time-migrated seismic sections over the Léogâne area have shown disruptions and discontinuities in the subsurface. The resolution and S/N of the seismic data were too low to confidently identify the nature of the layers; however, these discontinuities may be associated with channel deposits of the Léogâne fan-delta (Figures 4.11, 4.12 and 4.13). Shallow subsurface S-wave images also indicated a change in the shallow structure and seismic velocities. Discontinuous layers are identified as 10 to 30 m thick channel bodies deposited on previous fan surfaces

Some of the results from near-surface seismic sections included south dipping layers for lines B, C and D, and a folded subsurface structure for line A and seismically weak near-surface materials. We were unable to image any substantial faulting within the coverage of the seismic data, which was consistent with the lack of surficial faults on the Léogâne fan.

Figure 4.14 integrates the remote sensing techniques with uplift observation, gravity data and the aftershock studies. Seismic results from line A indicated the folding in the subsurface and the results from line B and D showed relatively steeper, south limb of the fold of the uppermost section of the Léogâne fan delta. These results are consistent with: 1) southward-directed thrusting on the blind Léogâne reverse fault; 2) the asymmetrical shape of the coastal uplift (Figure 4.14a); and 3) the asymmetrical shape of the uplift (Figure 4.14b) inferred from satellite radar data. Figure 4.14a also integrates the gravity survey results with the coastal uplift studies. Our 4,000 m gravity line suggest a decrease in the gravitational field between southern end of the fan and line A and increase of the gravitational field from line A to the north. This anomaly may be related to the south dipping seismically low velocity and low-density subsurface layers and the possible folding structure underneath line A. We expect that the limbs of the fold steepen with depth, which may indicate that the fold may be formed by a series of similar folding events overlying the blind Léogâne thrust fault. A previous folding event might have possibly included the historical event of 1701 described by Bakun et al. (2012) as having very similar deformational effects as the 2010 event.

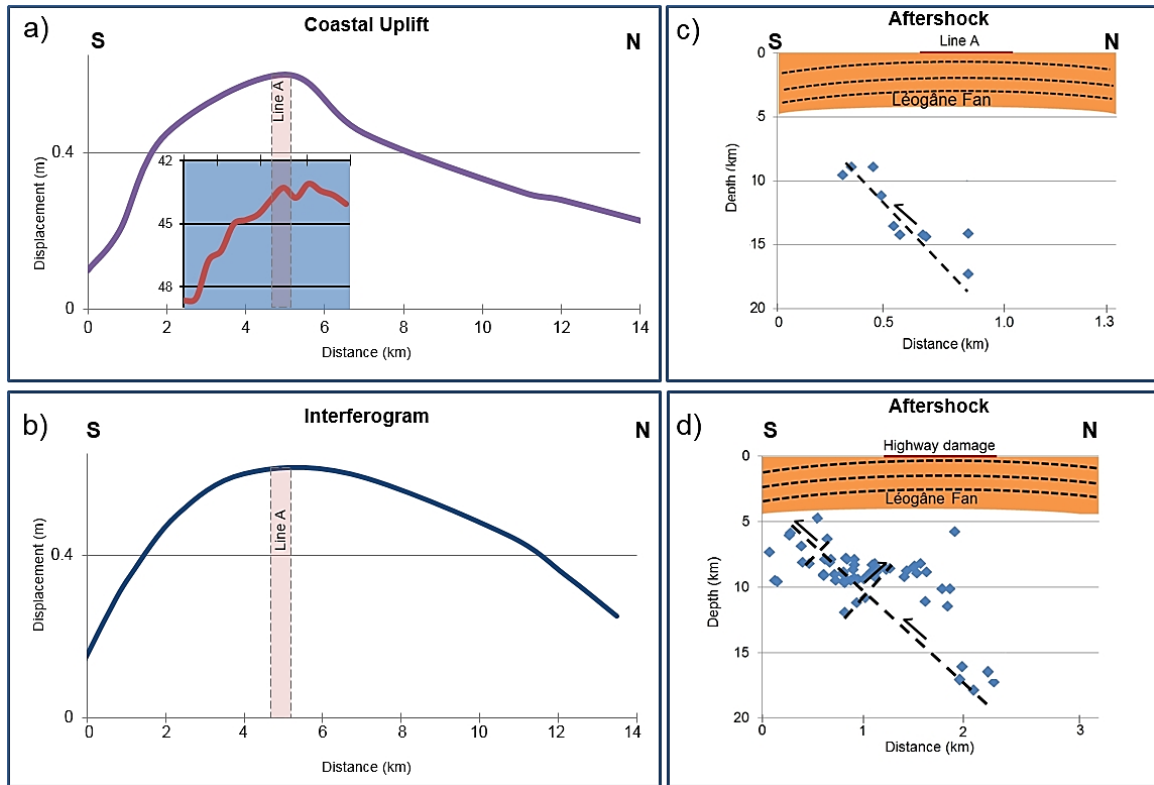


Figure 4.14. Integration of observations of coseismic folding during the 2010 Haiti earthquake. (a) Uplift of coastal coral with the gravity data inset. Line A coverage is indicated. (b) Displacement inferred from radar interferometry results between along the coast of L'èogâne with the coverage of the line A indicated. (c) Aftershock events (Douilly et al., 2015) in the vicinity of line A. (d) Aftershock events around the north-south paved highway ~3 km east of our lines with the proposed geometry for the L'èogâne fault.

Aftershock data in the vicinity of seismic line A were selected to investigate the depth of the seismically active zone beneath our survey area. These aftershock events were mostly concentrated 9 to 17 km at depth and suggest a steep northward-dipping fault plane with an estimated dip of 60° to 70° (Douilly et al., 2013). When the aftershock cross section was generated using aftershocks beneath the damaged highway area, we noted that the shallowest event occurred around 4 km.



Figures 4.14c and 4.14d show the proposed fault geometry from selected aftershock events with the main fault plane dipping towards northward. The existence of the northward-dipping thrust fault may explain the uplift observed over the featureless plain of the Léogâne fan-delta and discussed at length by Hashimoto et al. (2011). Relatively shallower and smaller, antithetic faults dipping towards the south were also inferred by Douilly et al. (2013).

Figure 4.15 compares results from our geophysical surveys conducted in 2012 and 2013 and provide a proposed geometry for the blind Léogâne reverse fault based on aftershocks (Calais et al., 2010; Hayes et al., 2010; Douilly et al., 2013). When both P-wave and S-wave analyses are combined, the top shallow layers are interpreted as seismically slow and weak soil. Our analysis for the soil type agrees with some of the previous studies over the Léogâne area, as “Quaternary alluvial material” (Mann et al., 1995). Results from refractions studies and laboratory measurements suggested a relatively seismically faster lithology (e.g., sandstone) starting from 40 m to 50 m in-depth.

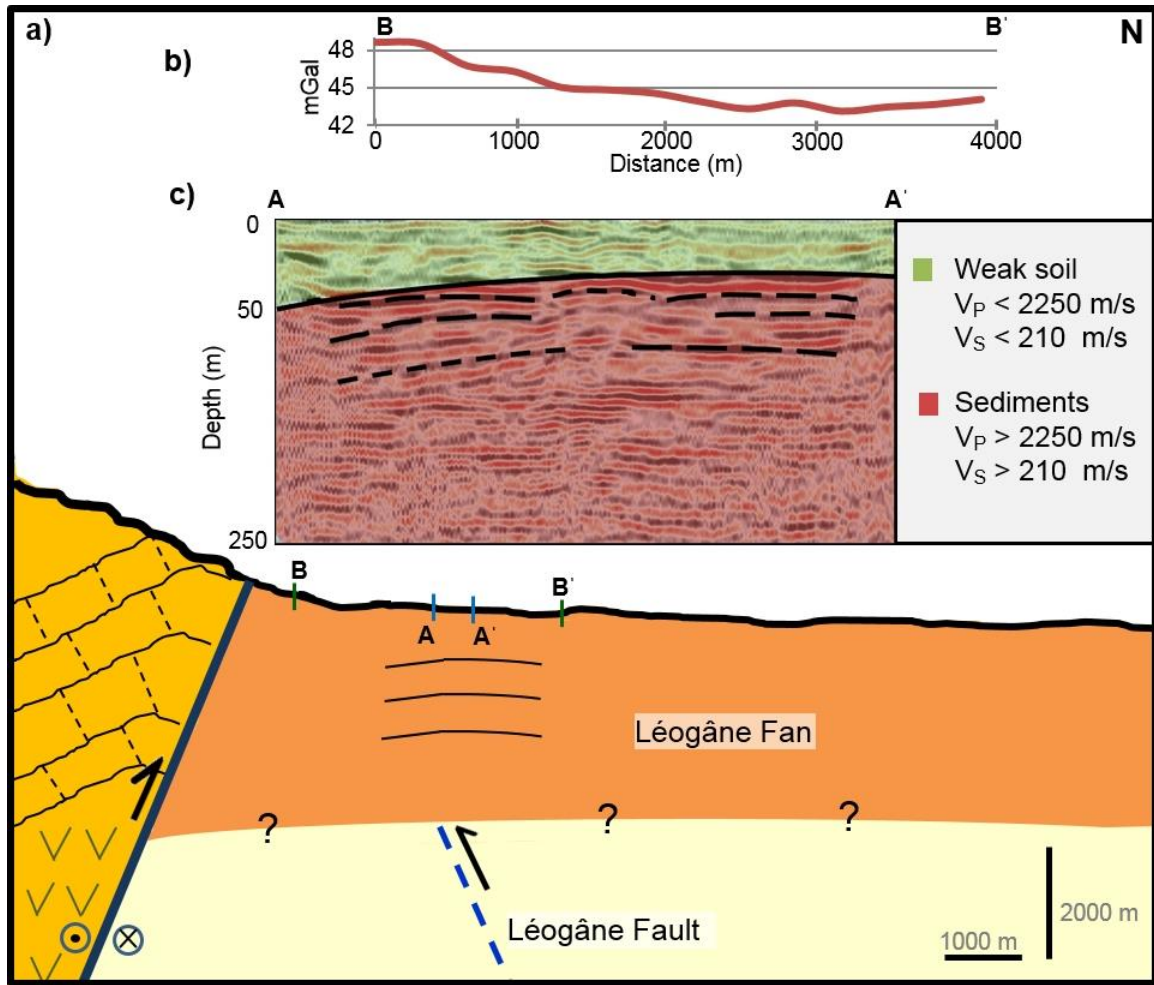


Figure 4.15. (a) Interpretive cross-section for the Léogâne fan and dashed blue line showing the proposed fault geometry for the Léogâne fault blind reverse fault (modified from Douilly et al., 2013). (b) Free-air corrected gravity results, B-B'. (c) Line A seismic section with overlain seismic velocities, A-A'.

Our integrated results over the Léogâne fan are consistent with the proposed thrust blind fault, which may have caused uplift. Previous studies on aftershock locations over this area suggested that the shallowest aftershock below our study area occurred around 4,000 m. More detailed gravity surveys along with seismic surveys using longer offsets and larger sources would be useful to further the investigation.

## 4.5 Conclusions

Two geophysical surveys were performed in 2012 and 2013 over the Léogâne fan delta. To understand the sediment properties and image the near-surface structure: (1) laboratory measurements over the rock hand samples were completed, and (2) 2D seismic data along multiple lines were acquired. Laboratory measurements of the rock samples yielded velocity and density information which may indicate the subsurface lithologies at the Léogâne fan delta. The P-wave near-surface velocity models were generated from multiple seismic lines. Seismic studies over line A, imaged the first 400 ms (approximately 250 m) using a 4.5 kg hammer. Line B was able to image up to 500 ms (approximately 350 m) using a 40 kg weight drop system. The P-wave refraction studies estimated an average velocity of 1,800 m/s for the very near surface. A near-surface S-wave velocity section was generated using a surface-wave inversion method, with an average velocity of 180 m/s for the first 30 m. Initial analysis of S-wave reflection data indicated a strong reflector with a RMS velocity of 250 m/s from 40 m to 50 m depth. S-wave studies suggested weak soil conditions over the Léogâne fan. These weak sediments are Class E soils (NEHRP, 2014). P-wave reflection and refraction studies over both line A and B showed south dipping seismically low-velocity layers.

In an attempt to reveal some of the deformational features associated with the 2010 Haiti earthquake and possibly earlier earthquake events, we integrated (1) interferometry data, (2) aftershock data, and (3) uplift observations with the geophysical data over the Léogâne area. Steeper-dipping layers along the southern end of the fan composed of seismically

weak near-surface materials were observed for the first time in our seismic sections. Folding of the fan-delta strata was noted on multiple seismic lines. The folding may be associated with coastal uplift and structural damage to the north-south paved highway; these changes appeared to have occurred over an anticlinal axis that was 14 km wide and 4 km long. The magnitude of the coseismic uplift of the anticline was 60 cm based on reef data, and 20 to 60 cm based on radar interferometry. Satellite imagery showed the anticlinal axis was temporary and may not have contributed to the longterm uplift of the fan-delta.

We see no conclusive evidence for the brittle faulting penetrating the upper 350 m of the Léogâne fan-delta. The blind reverse fault may have created a change in shape of the ground surface by folding poorly consolidated sediments of the Léogâne fan-delta. This deformation appears to be located above the proposed blind reverse fault, with inferred dipping of 60° to 70° to the north from the distribution of aftershocks (Douilly et al., 2013). Abrupt coseismic folding of the ground surface may have localized damage to a major, paved highway and the maximum area of reef uplift. For that reason, we interpret the road damage as a result of folding, or change in shape of the ground surface, likely combined with liquefaction of the low lying areas surrounding the raised berm on which the road was built. Minor disruptions and discontinuities of reflectors observed on seismic lines were supported by local gravity variations and are interpreted as lateral facies changes within the Léogâne fan-delta. The initial decrease of the gravitational field was interpreted as the thickening of south dipping low-velocity, low-density layers. An increase of the gravitational field towards the end of the survey was interpreted as the effects of possible folding structure in the subsurface. These reconnaissance geophysical measurements

provided further background information for additional geohazard work in the Léogâne area as well as parameters for designing deeper geophysical surveys to directly image the proposed blind reverse fault responsible for the 2010 Haiti earthquake.

## 4.6 Seismic survey design for the future surveys

### 4.6.1 Land surveys - Surface seismic

Some of the results obtained from the integrated studies (discussed in previous sections) included:

- Slow P-wave velocities (for the top 450 m).
- No brittle faulting within the coverage of the seismic lines.
- Fluvial channeling, which may indicate seismically weak layers at depths greater than 450 m.
- Indication of Léogâne fault. Most likely to be located around 4 km at depth and approximately 2 km away from the EPGFZ with a 60° to 70° dip towards the north.
- The folding of strata between the proposed fault and the surface. The southern side of the folding appears to be relatively steeper and the crest of the folding appears to be directly above the proposed location of the Léogâne fault.

During the fieldwork in 2012 and 2013 we were unable to image the proposed Léogâne fault. Stronger seismic sources (possibly a Vibroseis) with extended offsets will be needed to image subsurface structures up to 4 to 5 km in-depth. To understand the minimum requirements for future surveys which may help to seismically image the Léogâne fault; we have completed survey design analyses.

Surface conditions were one of the limiting factors for future surveys which would require extended offsets and stronger sources. Unfortunately, most parts of the potential survey location, an area between the city of Léogâne and the EPGFZ, is occupied with farm lands and small villages. The current condition of the land makes it difficult to achieve 3D seismic acquisition; therefore, we are proposing multiple 2D seismic lines. During the 2012 and 2013 surveys, S-wave data provided useful results for the soil classifications. We believe that relatively deeper converted-waves can also complement the P-wave data and provide useful results; therefore, multicomponent data should also be requirement for future surveys.

Analysis of the satellite imagery indicated that approximately 6 km long lines may be a possibility for future seismic surveys. To obtain seismic data with multi-azimuthal coverage, we propose a geometry which resembles a star-shape and consists of three 2D seismic lines. These lines are 6 km in length and each line contains 400 receiver points with 15 m spacing. These are the acquisition details for the proposed 2D seismic line:

- Line Length: 6 km
- Total number of lines: 3
- Source: Vibroseis
- Source spacing: 15 m
- Receiver spacing: 15 m
- Receiver type: 3C-Land nodal system

The proposed geometry with both PP and PS fold maps for a target at 4 km can be seen in Figure 4.16 and 4.17.

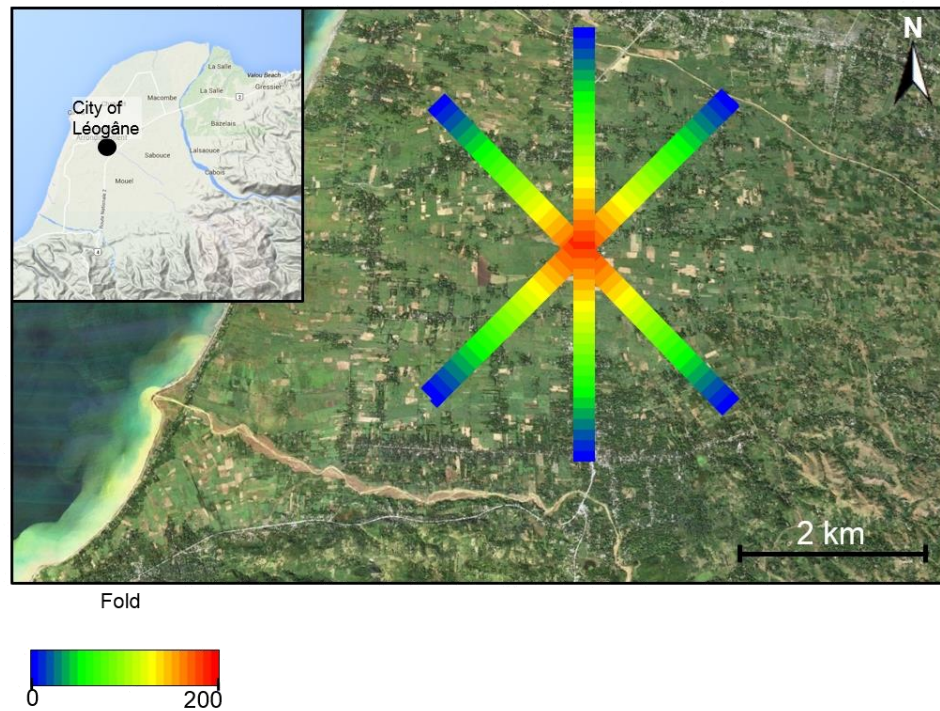


Figure 4.16. Proposed geometry for future seismic surveys in the Léogâne area. The 2D lines are 6 km long and colored by PP fold. Warmer colors represent the higher fold values.

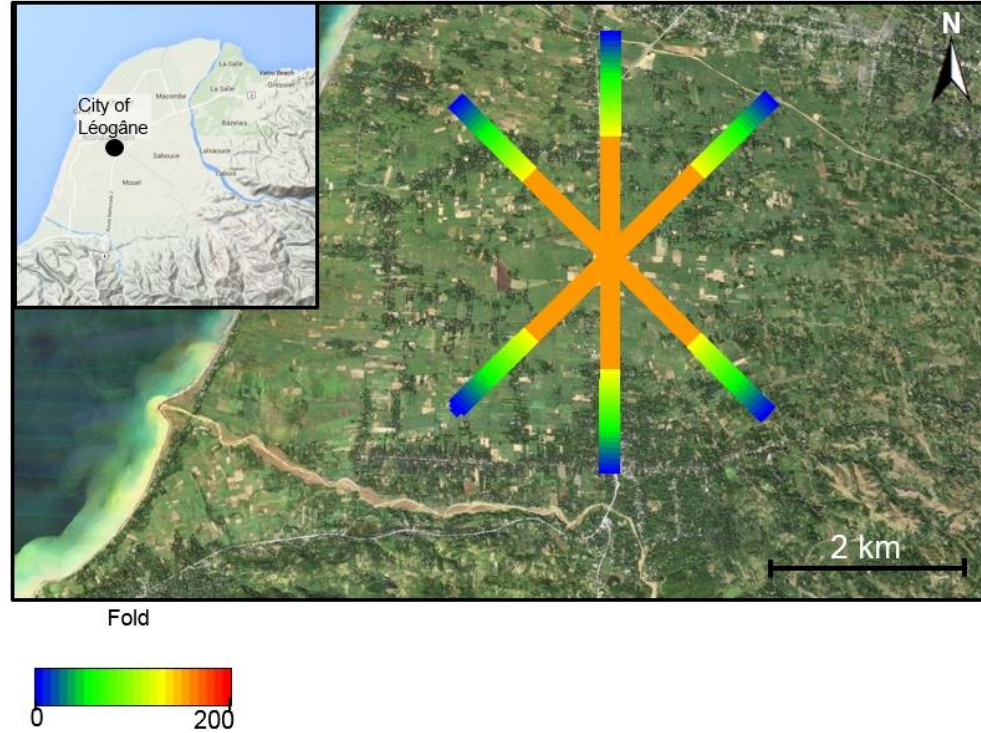


Figure 4.17. Proposed geometry for future seismic surveys in the Léogâne area. The 2D lines are 6 km long and colored by PS fold. Warmer colors represent the higher fold values.

Another important factor to consider, regarding seismic survey design, is the determination of optimal offsets. To obtain the optimal offset information, we generated a simple 2D model that is based on the results obtained by integrated geophysical analyses. The model is 4.5 km in-depth and 10 km in length, consisting of four layers. Seismic velocities of the layers can be seen in Figure 4.18. We positioned the proposed blind fault, with  $60^{\circ}$  -  $70^{\circ}$  dip towards the north, about 2 km away from the southern end of the model and approximately 4 km at depth.



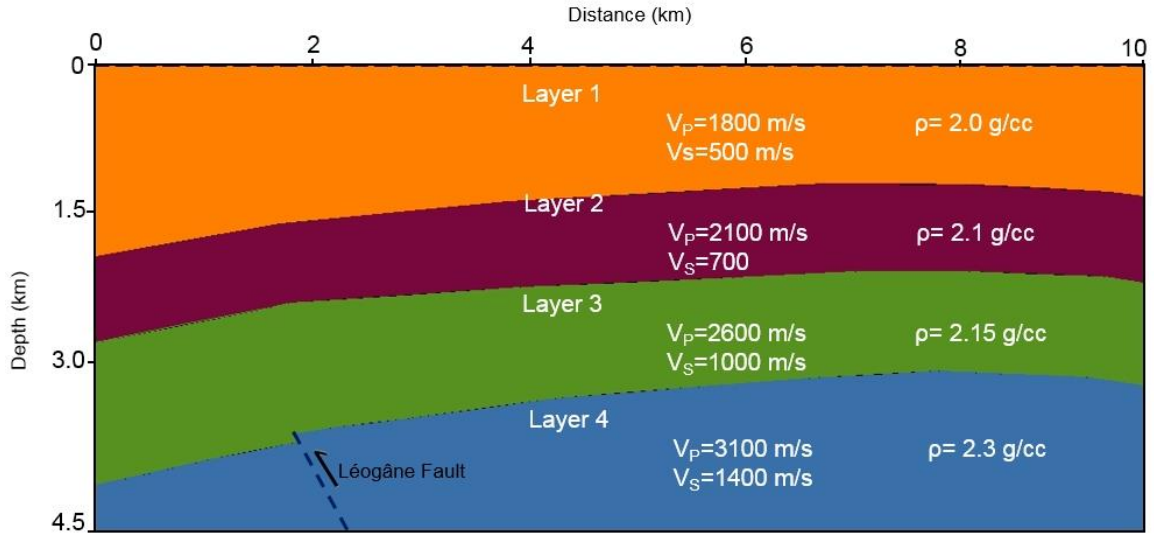


Figure 4.18. 2D simple earth model that contains four layers with corresponding velocities and densities. The location and geometry of the proposed Léogâne fault is shown with the blue dashed line.

For a single shot located at 100 m away from the southern end of the model, reflecting and refracting rays can be seen in Figures 4.19 and 4.20 (source rays are not shown for display purposes). These analyses have helped us to determine the critical offsets, where the refractions begin to dominate the reflection data. In addition, a refraction survey on its own could be useful to obtain the depth to higher velocity layers. For PP-waves, approximately at 4 km offset refracting waves began arriving. It appeared that the refractions started to dominate the data at around 6 to 7 km offset. In the case of PS-waves, the refracting waves dominated the data after about a 4 km offset. We plan to use converted data to support the P-wave results; therefore, an optimal offset of 6 km was chosen to be used in the seismic survey designs. A simple earth model also enabled us to determine the required recording

time for the seismic data acquisition (Figures 4.19 and 4.20). For the reflection data, 5 second was needed to record the PP-waves, and 10 seconds of data was required for PS-waves.

For the next part of the analysis, we calculated the vertical and horizontal resolution of the seismic data in the horizon of interest ( $\sim 4$  km at depth). Using the interval velocities and a frequency of 35 Hz, we determined that the vertical resolution of the seismic data was between 20 to 30 m, whereas the horizontal resolution was approximately 50 to 55 m. Hayes et al. (2010), proposed that the slippage up to 3.5 m over the Léogâne fault is to be expected due to 2010 earthquake. Considering the long history of the earthquakes at this region, it may be reasonable to assume accumulation of slippage to reach tens of meters over several hundred years. Therefore, resolution of proposed seismic survey should be adequate to seismically image the possible fault slippage.

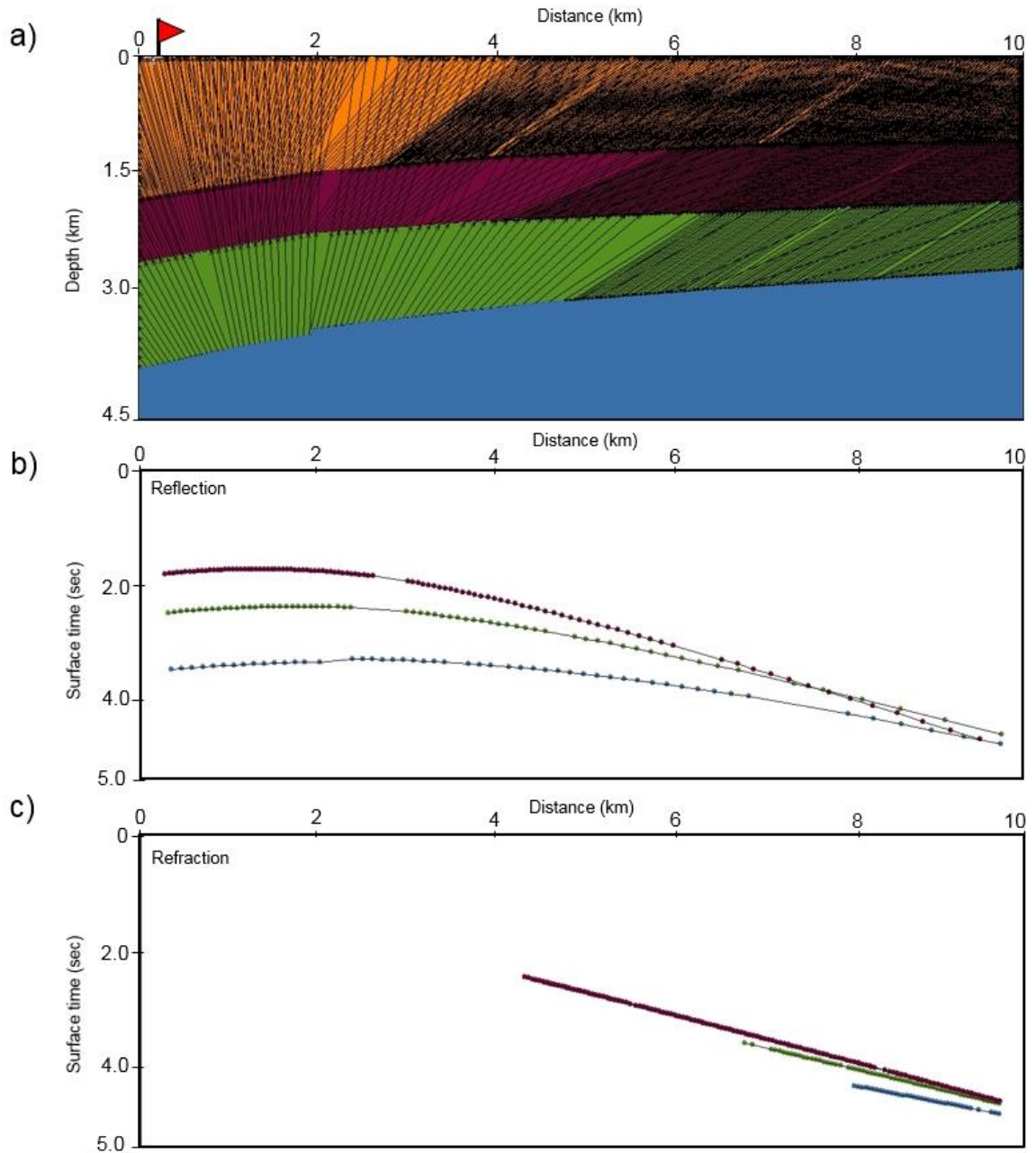


Figure 4.19. (a) Reflection and refraction event for PP rays over the four layer simple earth model, source rays are not shown for display purposes. Shot location is marked with a red flag. (b) Surface recording time, in seconds, for reflecting rays. (c) Surface recording time, in seconds, for refracting rays.

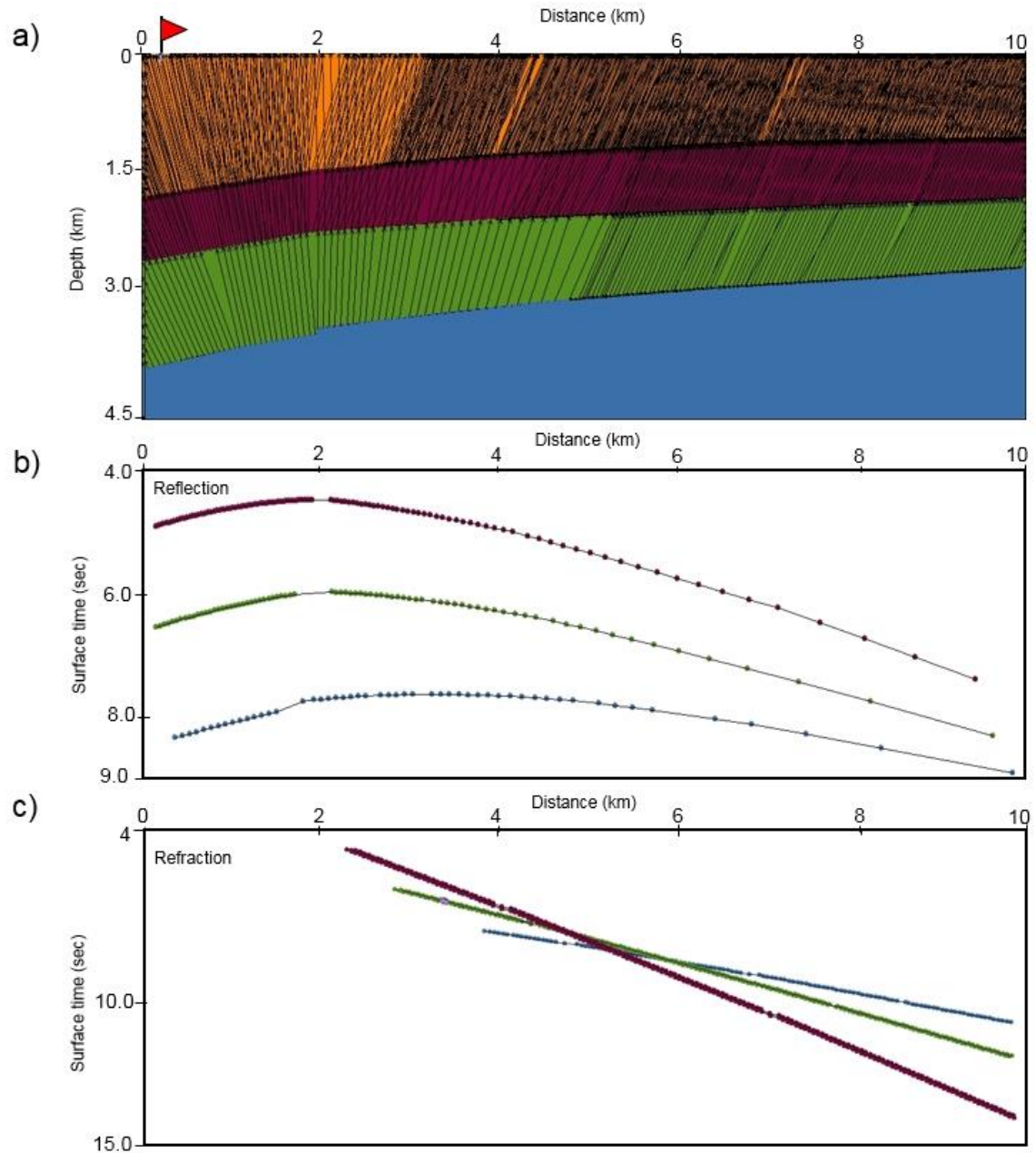


Figure 4.20. (a) Reflection and refraction event for P-P-S rays over the four layer simple earth model, source rays are not shown for display purposes. Shot location is marked with a red flag. (b) Surface recording time, in seconds, for reflecting rays. (c) Surface recording time, in seconds, for refracting rays.

#### 4.6.2 Land surveys - Vertical seismic profiling

An additional recommendation for the future land surveys is the Vertical Seismic Profiling (VSP). To our knowledge there has been no land reflection seismic data undertaken in Haiti. Unfortunately there are also no real time seismometer beneath the seismically slow fan delta sediments, for geohazard studies, at the Léogâne area. We are proposing permanently sealed downhole seismometers, up to 3 km in depth. Constant recording from these receivers would allow researchers for both the earthquake studies and the reflection seismology studies.

Deeper subsurface structure and seismic velocities still remains somewhat ambiguous. A VSP survey can help us to determine the seismic velocities with a higher resolution. The proposed well location for the Léogâne area is located at the central part of the future 2D surveys. Therefore the results from the surface seismic studies can directly be tied with the VSP results. We are proposing a slightly deviated well that penetrates up to 3 km in-depth (Figure 4.21). The total number of 250 surface shots were fired for a VSP tool that containing forty 3C channels with 25 m spacing. The fold map for PP-waves can be seen in Figure 4.20.

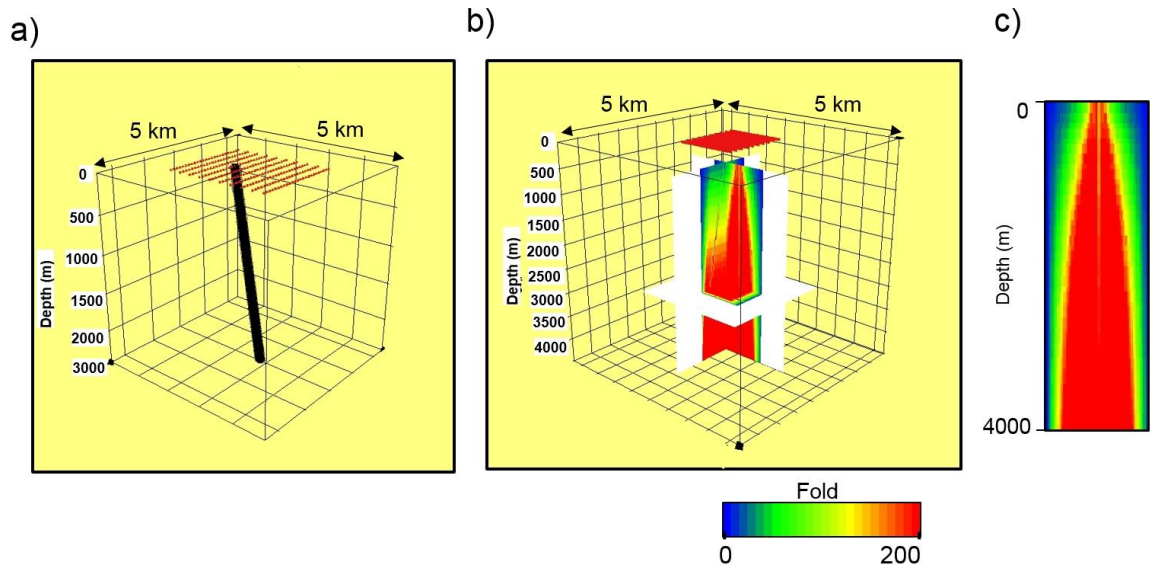


Figure 4.21. (a) The VSP geometry; red lines at the surface indicate the shot locations and black line in the subsurface represent the receiver locations (the trajectory of the well). (b) Resulting PP fold map; warmer colors indicate the higher fold values. (c) The cross line view of the PP fold map.

#### 4.6.3 Marine Surveys

Recent studies suggest that the Enriquillo fault may extend from the Léogâne area to Grand Goave region (Hayes et al., 2010), meaning that the fault may be imaged by marine seismic surveys as well. Marine surveys can also be helpful to image the EPGFZ, some of the smaller deformational faults, and slides and uplift of the reefs as suggested by previous studies (Calais et al., 2010; Hayes et al., 2010; Hornbach et al., 2010; Prentice et al., 2010). Unfortunately, there are some limitations for such a survey due to shallow water depth and the proximity to land which prohibits the possibility of large vessels. However, a simple marine survey with a small boat and limited receivers can be useful in this particular setting.

To assess the location and geometry of the faults, and imaging the deformation associated with these faults, we designed a marine survey using a single boat with a small source and single streamer (24 hydrophones with 4 m spacing). Proposed sail lines for such a survey can be seen in Figure 4.22. The design contained 140 lines and covered approximately a 28 km<sup>2</sup> area. This survey was mainly designed to acquire offshore seismic data for an area between Léogâne and Grand Goave, using limited seismic resources.

The proposed geometry for the Léogâne fault is marked with red dashed line in Figure 4.22. The orientation of the fault changes around the coast lines and the sail lines were oriented in a slightly oblique geometry extending from NW to SE in an effort to keep them perpendicular to the proposed geometry of the Léogâne fault (Hayes et al., 2010; Douilly et al, 2015). Due to the limited number of receivers, a small boat can assist in reducing the downtime between sail line turns. A survey of this size with a 10 % downtime approximation should take about 7 days, using a boat with 3 knots speed.

Due to the limited streamers and single source the resulting fold for the entire survey consisted of 140 2D lines with a constant fold of 24.

Another possibility for the future surveys would be the usage of land nodal systems with the small marine source (i.e., bubble-pulser). With the current equipment capability, we would be able to deploy about 200 multicomponent nodal receivers along the coast line



with 20 to 50 m spacing. The vessel with bubble-pulser source can efficiently acquire the data within matter of days across the coast line.

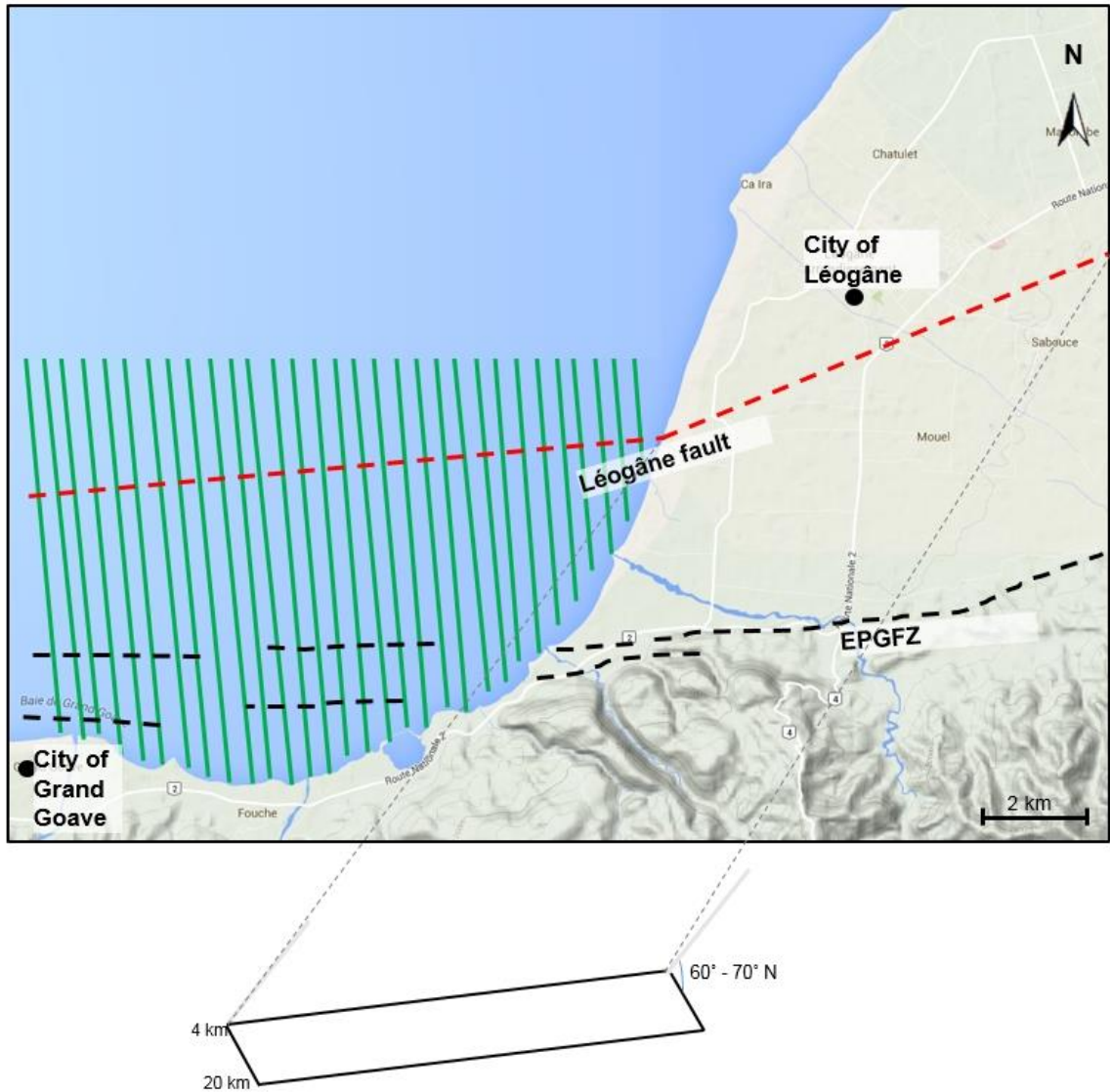


Figure 4.22. Area of the proposed marine survey between Léogâne and Grand Goave; the 3D proposed geometry for the Léogâne fault (modified from Hayes et al., 2010; Douilly et al., 2015). Green lines represent sail lines, the black dashed line represents the extension of the EPGFZ and the red dashed line indicates the Léogâne fault.



## **Chapter 5**

### **Summary and Recommendations**

A detailed study has been undertaken in this dissertation for survey design studies in different geological conditions. Using the target-oriented nature of the survey design studies as an objective this thesis is divided into three chapters. These were: 1) marine seismic survey designs for a subsalt target at Gulf of Mexico, 2) multicomponent on-land seismic survey designs for an unconventional resource, and 3) integrated geophysical data analyses and survey design for a blind fault imaging at the 2010 Haiti earthquake epicentral area.

Two marine seismic survey geometries, dual-coil shooting and wide-azimuth shooting (WAZ), are investigated using multi-vessel geometries to cover more than 2,000 km<sup>2</sup> area of ultra-deep water in the northern Gulf of Mexico. The surveys were first tested for the fold distribution and azimuth/offset coverage over a flat layer lying at 10.5 km depth. The dual-coil yielded rich and smoother fold maps with full-azimuthal coverage (FAZ), whereas the WAZ survey contained some acquisition footprints due to straight-line geometry with relatively limited-azimuthal coverage. Even though the WAZ results provided slightly lesser fold, the illumination area was 15 % larger than the dual-coil geometry. The continuous data acquisition, without line changes, of the dual-coil geometry lessen the acquisition time ~ 40 % when compared to WAZ geometry. We then completed

illumination analyses, using the two survey geometries, over a subsurface geological model. The illumination efforts were mainly concentrated for a subsalt prospect lying at a depth of approximately 10.5 km. Conventional 3D ray-based imaging showed that the coil survey provided less illumination holes and better sampling of a subsalt prospect. Some of the steep structural dips were not resolved for the WAZ survey.

We then introduced a target-oriented, ray-method based, survey design to optimize the both surveys (dual-coil and WAZ). The optimal survey design was introduced as a methodology for designing acquisition of new seismic data that will optimally complement the existing data. The selected subsalt target area contained steep dips over an approximately 145 km<sup>2</sup> area. The optimal survey design carefully identified the contribution, for the illumination of the selected target area, using the individual-coils for the coil survey and the sail lines for the wide-azimuth surveys. This method also enabled us to quantitatively compare the success of illumination, which indicated only one third of the total number of coils were required to illuminate the selected target area. For the overall illumination intensity, we found that the WAZ survey had 20 % less intensity than the coil survey for the selected target area.

To overcome the simplicity of ray tracing over complex lithologies, we employed wave-equation-based illumination. The target-oriented nature of this method provided significant reduction in processing and modeling time, by enabling us to complete an illumination analyses with only 4,000 modeled shots as opposed to the original 160,000 shots. This

method also calculated the energy distribution of the shots according to their contribution for the illumination of the target area. The wave-equation illumination results showed more detailed energy distribution for both subsurface and surface illumination maps.

For the surveys that are areally limited, a suggestion was made which was based on the ellipse geometry. Alternative marine seismic design geometries have shown the possible advantages, under certain conditions, of the ellipse design when compared to the coil and the WAZ geometries. The ellipse design required 25 % less acquisition time than the coil design. However, some compromises over the seismic attributes included the: 1) loss of full azimuth coverage, and 2) domination of medium offsets (limited far offsets).

Next, we evaluated seismic attribute distributions for various PS survey designs. 3C-3D test surveys over an area of  $10.5\text{km}^2$  was generated to better understand the effects of individual design parameters (e.g.,  $V_P/V_S$  values, target depth, target dip, acquisition geometry, and bin size) over both PP and PS illumination maps.  $V_P/V_S$  values of 2, 4, and 6 were tested for the PS fold maps and common conversion points (CCP) are shifted towards the receivers for larger  $V_P/V_S$  values. This shifting helped us to obtain PS illumination over larger area; however, it also caused some illumination imprints which appeared as fold striping. Illumination results of a target layer at different depths (800, 1,600 and 3,200 m) showed that the deeper targets have helped to obtain more concentrated fold and trace distribution over the central part of the survey area. We also tested the effect of survey geometry over the illumination maps using orthogonal, parallel, and slanted

designs. Both the orthogonal and slanted designs provided better results than the parallel geometry; the slanted design showed improved illumination results for the PS studies. The effect of target layer dip,  $15^\circ$  and  $30^\circ$ , caused updip movement of the CCP, which required longer offsets to fully capture the seismic data. The further movement of the CCP's appeared to be linear with the amount of target layer inclination. Receiver-line stagger helped us to achieve 12.5 m by 25 m bin sizes (an improvement over the original 25 m by 25 m bin size). The re-arrangement of the receiver line geometry enabled us to obtain smaller bin sizes with almost no additional acquisition cost. As a result of these tests surveys, we have determined that the centered shot lines over a larger receiver grid yields the most beneficial illumination results while also yielding a full fold coverage.

A full scaled and more detailed, 3C-3D seismic survey was designed for an unconventional play. Both the orthogonal and slanted geometries were tested with different parameters to illuminate a layer with  $5^\circ$  dip, laying between 1,500 m to 2,500 m at depth. These geometries contained centered shot lines over a larger receiver grid. The effect of dip was very limited due to the existence of far offsets and gentle inclination of the target layer. East-west trending geometry imprints over fold maps were introduced due to three shot salvo. We applied receiver-line stagger, which enabled us to achieve 6.25 m by 25 m bin sizes without causing fold striping. Overall, a full fold coverage with smooth offset and azimuth distribution was obtained for all offsets. The slanted line, when compared to the orthogonal design, produced better seismic attribute distributions.

Lastly, we completed a case study which included: data acquisition, processing, integration, and interpretation of the data that was collected during 2012 and 2013 surveys at Léogâne fan, Haiti. Our research team from the University of Houston and Haiti Bureau of Mines and Energy collected shallow seismic and gravity data in the fan-delta where previous studies of earthquake aftershocks, coastal uplift of coral reefs, and radar interferometry all indicated the maximum amount of coseismic uplift. Our objective was to acquire geophysical information on the subsurface stratigraphy, structure, and material properties of the fan. S-wave studies revealed an average velocity of 180 m/s for the first 30 m. These velocity values suggest that the near-surface sediments at Léogâne are class E (National earthquake hazard reduction program). Interpretation of the various seismic methods indicates prolonged sedimentary environments of fluvial channeling and channel migration to a depth of 350 m, as expected in this fan delta setting. There is no clear evidence on our reflection lines for substantial faulting in the seismically weak, fan-delta sediments. Integrated geophysical data analyses indicated the folding of strata between the proposed fault and the surface. The southern side of the folding appears to be relatively steeper and the crest of the folding appears to be directly above the proposed location of the Léogâne fault. Integrated results from our studies, aftershock studies, and the uplift observations indicated the proposed Léogâne fault most likely to be located around 4 km at depth and approximately 2 km north of the EPGFZ with a 60° to 70° dip towards the north.

We then completed survey design studies for the future seismic surveys to properly image the proposed blind fault while providing deeper penetrating seismic images. Our suggestions include both land and marine surveys around the Léogâne area. Multiple 2D on-land seismic lines with 6 km offsets and different orientation (north-south, northeast-southwest, and northwest-southeast) in the Léogâne fan would help to obtain multi-azimuth seismic data. A VSP survey, located at the central location of the proposed seismic lines (~2 km north of the EPGFZ) and up to 3 km at depth in the Léogâne fan would provide seismic velocities with higher resolution. A small marine survey in an area between Léogâne and Grand Goave with the sail lines in northeast-southwest direction to image extension of the proposed the Léogâne fault. Both the land survey and marine survey would also be helpful to clearly image extend of the folding of the subsurface layers, which was concluded from this study.

## Appendix

The velocities were measured using spherical 500 kHz cylindrical transducers at the AGL facility. Transit time measurements were made over the samples of a measured length to give velocity on three orthogonal axes. For each axis, three separate measurements were done to take the average of the readings (to minimize the measuring error, with an average error of 2 %).

We identified sample A as a metamorphosed limestone, sample B as layered sandstone, and sample C as highly degraded (fractured and weathered) igneous rock (most likely basalt). The variations of the velocities along the different axes for sample B were quite high (~20 %). The variations of both  $V_P$  and  $V_S$  values indicated the layered structure of this rock sample. As expected, the velocities were highest along the axis of bedding (x2) and slowest perpendicular to the bedding (x1). Resulting values provided a general idea of the expected velocities around the survey area.

Density measurements of the samples provided useful information for the interpretations. Densities were calculated by the wax clod method. To carry out the measurements, paraffin material was used to cover pieces of the rock samples, which were used during density calculations. For each sample, density calculations completed over two smaller pieces and the resulting values were averaged to density measurements (Table 2).

The velocities were measured using spherical 500 kHz cylindrical transducers at the AGL facility. Transit time measurements were made over the samples of a measured length to give velocity on three orthogonal axes. For each axis, three separate measurements were done to take the average of the readings (to minimize the measuring error, with an average error of 2 %).

We identified sample A as a metamorphosed limestone, sample B as layered sandstone, and sample C as highly degraded (fractured and weathered) igneous rock (most likely basalt). The variations of the velocities along the different axes for sample B were quite high (~20 %). The variations of both  $V_P$  and  $V_S$  values indicated the layered structure of this rock sample. As expected, the velocities were highest along the axis of bedding (x2) and slowest perpendicular to the bedding (x1). Resulting values provided a general idea of the expected velocities around the survey area.

Density measurements of the samples provided useful information for the interpretations. Densities were calculated by the wax clod method. To carry out the measurements, paraffin material was used to cover pieces of the rock samples, which were used during density calculations. For each sample, density calculations completed over two smaller pieces and the resulting values were averaged to density measurements (Table 2).



## References

Bakun, W. H., C. H. Flores, and U. T. Brink, 2012, Significant earthquakes on the Enriquillo fault system, Hispaniola, 1500-2010: Implications for earthquake hazard: Bulletin of the Seismological Society of America, 102:1, 18-30, doi: 10.1785/0120110077.

Barton, N., 2006, Rock quality, seismic velocity, attenuation and anisotropy: Taylor & Francis.

Benford, B., C. DeMets, and E. Calais, 2012, GPS estimates of microplate motions, northern Caribbean: evidence for a Hispaniola microplate and implications for earthquake hazard: Geophysical Journal International, 191:2, 481-490, doi: 10.1111/j.1365-246x.2012.05662.

Bilham, R., and E. Fielding, 2013, Remote sensing and the search for surface rupture, Haiti 2010: Natural Hazards, 68:1, 213-217, doi: 10.1007/s11069-013-0550-0.

Brice, T., 2011, Designing, acquiring and processing a multivessel coil survey in the Gulf of Mexico: 81<sup>th</sup> Annual International Meeting, SEG, Expanded Abstracts, 92-96, doi: 10.1190/1.3628225.

Buia, M., P. E. Flores, D. Hill, E. Palmer, R. Ross, R. Walker, M. Houbiers, M. Thompson, S. Laura, C. Menlikli, N. Moldoveanu, and E. Snyder, 2008, Shooting Seismic Surveys in Circles: *Oilfield Review*, 20, 3, 18-31.

Calais, E., A. Freed, G. Mattioli, F. Amelung, S. Jonsson, P. Jansma, S. H. Hong, T. H. Dixon, C. Prepetit, and R. Momplaisir, 2010, Transpressional rupture of an unmapped fault during the 2010 Haiti earthquake: *Nature Geoscience*, 3, 794-799, doi: 10.1038/ngeo992.

Coles D., M. Prange, H. Djikpesse, 2014, Optimal survey design for big geodata: 84<sup>th</sup> Annual International Meeting, SEG, Expanded Abstracts, 127-131, doi: 10.1190/segam2014-0224.1.

Cordsen A., and D. C. Lawton, 1996, Designing 3-component 3-D seismic surveys: 66<sup>th</sup> Annual International Meeting, SEG, Expanded abstracts, 81-83, doi: 10.1190/1.1826779.

Cowgill, E., T. S. Bernardin, M. E. Oskin, C. Bowles, M. B. Yikilmaz, O. Kresylos, A. J. Elliot, S. Bishop, R. D. Gold, A. Morelan, G. W. Bawden, B. Hamann, and L. Kellogg, 2012, Interactive terrain visualization enables virtual field work during rapid scientific response to the 2010 Haiti earthquake: *Geosphere*, 8:4,787-804, doi:10.1130/ges00687.1.

Cox, B. R., J. Bachhuber, E. Rathje, C. M. Wood, R. Dulberg, A. Kottke, R. A. Green, and S. M. Olson, 2011, Shear wave velocity and geology-based seismic microzonation of Port-au-Prince, Haiti: *Earthquake Spectra*, 27:S1, 67-92, doi: 10.1193/1.3630226.

Diagon, F. L., J. Soldo, E. C. Mundim, C. E. Lemos, D. C. Garcia, A. Z. N. Barros, N. Moldoveanu, A. Fenwick, T. Bunting, A. Cooke, and R. M. Conteno, 2011, First full-azimuth towed-streamer survey offshore Brazil - An acquisition and survey design case study: 12th International Congress of the Brazilian Geophysical Society, 110-115.

Douilly, R., J. S. Haase, W. L. Ellsworth, M. P. Bouin, E. Calais, S. J. Symithe, J. G. Armbruster, B. M. Lepinay, A. Deschamps, S. L. Mildor, M. E. Meremonte, and S. E. Hough, 2013, Crustal Structure and Fault Geometry of the 2010 Haiti earthquake from temporary seismometer deployments: *Bulletin of the Seismological Society of America*, 103:4, 2305-2325, doi: 10.1785/0120120303.

Douilly, R., H. Aochi, E. Calais, and A. M. Freed, 2015, Three-dimensional dynamic rupture simulations across interacting faults: The Mw7.0, 2010, Haiti earthquake: *Journal of Geophysical Research, Solid Earth*, 120:2, 1109-1128, doi: 10.1002/2014jb011595.

Dowla, N., P. Mann, R. R. Stewart, and L. Chang, 2012, Shallow seismic profiling of onland Léogâne fan-delta, Haiti, for imaging fan stratigraphy and buried faults associated with the January 12, 2010, earthquake: 2012 Annual Fall Meeting, American Geophysical Union, Abstract, T41A-2571.

EIA, 2013, U.S. Energy Information Administration, accessed 2 February 2015 at [http://www.eia.gov/analysis/studies/worldshalegas/images/fig1map\\_large.jpg](http://www.eia.gov/analysis/studies/worldshalegas/images/fig1map_large.jpg).

French, W., 1984, Circular seismic acquisition system: U. S. Patent 4 486 863, accessed 10 September, 2014 at <http://www.google.com/patents/US4486863>.

Galloway, W. E., 2011, Pre-Holocene geological evolution of the northern Gulf of Mexico Basin: Gulf of Mexico origin, waters, and biota: *Geology*, 3, 33-45.

Harrison, P. M., 1990, Dip moveout for converted-wave (P-SV) data: *Crewes Research Report*, 89-111.

Hashimoto, M., Y. Fukushima, and Y. Fukahata, 2011, Fan-delta uplift and mountain subsidence during the Haiti 2010 earthquake: *Nature Geoscience*, 4, 255-259, doi: 10.1038/ngeo1115.

Hayes, G. P., R. W. Briggs, A. Sladen, E. J. Fielding, C. Prentice, K. Hudnut, P. Mann, F. W. Taylor, A. J. Crone, R. Gold, T. Ito, and M. Simons, 2010, Complex rupture during the 12 January 2010 Haiti earthquake: *Nature Geoscience*, 3, 800-805, doi: 10.1038/ngeo977.

Hornbach M. J., N. Braudy, R. W. Briggs, M. Cormier, M. B. Davis, J. B. Diebold, N. Dieudonne, R. Douilly, C. Frohlich, S. P. S. Gulick, H. E. Johnson, P. Mann, C. McHugh, K. Ryan-Mishkin, C. S. Prentice, L. Seeber, C. C. Sorlien, M. S. Steckler, S. J. Symithe, F. W. Taylor, and J. Templeton, 2010, High tsunami frequency as a result of combined strike-slip faulting and coastal landslides: *Nature Geoscience*, 3, 783–788, doi: 10.1038/ngeo975.

Kocel, E., R. R. Stewart, P. Mann, L. Chang, and J. Wang, 2014, Searching for blind faults: The Haiti subsurface imaging project: *The Leading Edge*, 33, 12, 1372-1377, doi: 10.1190/tle33121372.1.

Koehler, R., and P. Mann, 2011, Field observations from the January 12, 2010, Haiti earthquake: Implications for seismic hazards and future post-earthquake reconnaissance investigations in Alaska: State of Alaska, Department of Natural Resources, Division of Geological & Geophysical Surveys, Report of Investigations, 2011:2, 24.

Lapilli, C., A. Gonzalez, D. Nichols, and J. Perdomo, 2010, Resolution analysis for targeted illumination using two-way wave equations: 80<sup>th</sup> Annual International Meeting, SEG, Expanded Abstracts, 41-45, doi: 10.1190/1.3513742.

Lawton, D. C., and P. W. Cary, 2003, Considerations in 3D depth-specific P-S survey design: Crewes Research Report, 15, 1-22.

Liner, C., 2004, Elements of 3D Seismology (Second Edition): PenWell publication.

Mandraux, F., B. S. Ong, C. O. Ting, S. Mothi, T. Huang, and Y. Li, 2013, Broadband, long-offset, full-azimuth, staggered marine acquisition in the Gulf of Mexico: First Break, 31, 6, 125-132.

Mann, P., F. W. Taylor, R. L. Edwards, and T. L. Ku, 1995, Actively evolving microplate formation by oblique collision and sideways motion along strike-slip faults: An example from the northeastern Caribbean plate margin: Tectonophysics, 246, no.1-3, 1-69, doi: 10.1016/0040-1951(94)00268-e.

Moldoveanu, N., and J. Kapoor, 2009, What is the next step after WAZ for exploration in Gulf of Mexico: 79<sup>th</sup> Annual International Meeting, SEG, Expanded Abstracts, 41-45, doi: 10.1190/1.3255750.

Moldoveanu, N, 2010, Random Sampling: A New Strategy for Marine Acquisition: 80<sup>th</sup> Annual International Meeting, SEG, Expanded Abstracts, 51-55, doi: 10.1190/1.3513834.

Moldoveanu, N., R. Fletcher , A. Lichnewsky, D. Coles, and H. Djikpesse, 2013, New aspects in seismic survey design: 83<sup>th</sup> Annual International Meeting, SEG, Expanded Abstracts, 186-190, doi: 10.1190/segam2013-0668.1.

Monk, D., 2014, How technology changes seismic acquisition: A look backwards and forwards in time: Annual Dobrin Lecture at University of Houston.

NEHRP, 2014, National Earthquake Hazard Reduction Program: Soil type and shaking hazard, accessed 15 February 2014 at <http://www.nehrp.gov/>.

NEIC, 2014, National Earthquake Information Center, US Geological Survey, accessed 15 February 2014 at <http://earthquake.usgs.gov/regional/neic/>.

Park, C. B., R. D. Miller, and J. Xia, 1999, Multichannel analysis of surface-waves: *Geophysics*, 64, 800–808, doi: 10.1190/1.1444590.

Park, C. B., 2011, Imaging dispersion of MASW data – full vs. selective offset scheme: *Journal of Environmental and Engineering Geophysics*, 16, no.1, 13–23, doi: 10.2113/jeeg16.1.13.

Prentice, C. S., P. Mann, A. J. Crone, R. D. Gold, K. W. Hudnut, R. W. Briggs, R. D. Koehler, and P. Jean, 2010, Seismic hazard of the Enriquillo–Plantain Garden fault in Haiti inferred from palaeoseismology: *Nature Geoscience*, 3, 789-793, doi: 10.1038/ngeo991.

Rathje, E., J. Bachhuber, B. Cox, J. French, R. Green, S. Olson, G. Rix, D. Wells, O. Suncar, E. Harp, P. Mann, and R. Koehler, 2010, Geotechnical reconnaissance of the 2010 Haiti earthquake: GEER (Geotechnical Extreme Events Reconnaissance), accessed 10 October 2014 at <http://www.geerassociation.org/>.

Roy, S., and R. R. Stewart, 2012, Near-surface seismic investigation of Barringer (Meteor) Crater, Arizona: *Journal of Environmental and Engineering Geophysics*, 17, no.3, 117-127, doi: 10.2113/jeege17.3.117.

Salvador, A., 1991, Origin and development of the Gulf of Mexico basin: in, Salvador, A., (ed.), *The Gulf of Mexico Basin: The Geology of North America*, J, 389- 444.

Sawyer, D. S., R. T. Buffler, and R. H. Pilger, 1991, The crust under the Gulf of Mexico basin, In Salvador, A., (ed.), *The Gulf of Mexico Basin: Boulder, Colorado, Geological Society of America, Geology of North America*, J, 53–72.

Sheriff, R. E., 2002, *Encyclopedic Dictionary of Applied Geophysics (Fourth Edition)*: Society of Exploration Geophysicist (SEG) publishing.



Stewart, R. R., J. E. Gaiser, R. J. Brown, and D. C. Lawton, 2003, Converted-wave seismic exploration: applications: *Geophysics*, 68, 1, 40-57, doi: 10.1190/1.1543193.

Stewart, R. R., 2009, The measure of full-wave motion: An overview of multicomponent seismic exploration and its value: *Canadian Society of Exploration Geophysicist Recorder*, 34, 10, 34-38.

Tang, Y. J., Y. F. Chang, and T. S. Liou, 2010, Asymptotic Conversion Point Equations for Converted Waves: *Terrestrial Atmospheric and Oceanic Sciences*, 21, 4, 639-644, doi: 10.3319/tao.2009.07.24.01.

Taylor F., P. Mann, R. Briggs, C. Prentice, P. Jean, C. Shen, H. Chiang, and X. Jiang, 2011, Late Holocene paleo-uplift events at the Tapion restraining bend in Haiti: Implications for earthquake recurrence in the vicinity of the 2010 rupture zone: 2011 Annual Fall Meeting, American Geophysical Union, Abstract T33G-2491.

Vermeer, G. J. O., 2012, 3D seismic survey design (Second Edition): Society of Exploration Geophysicist Books.

Watkins, J. S., G. MacRae, and G. R. Simmons, 1995, Bipolar simple shear rifting responsible for distribution of mega-salt basins in Gulf of Mexico: 16<sup>th</sup> Annual Gulf Coast Section of Society of Sedimentary Geology Foundation Bob F. Perkins Research Conference Proceedings, 297-305.

Worrall, D. M., and S. Snelson, 1989, Evolution of the northern Gulf of Mexico, with emphasis on Cenozoic growth faulting and the role of salt: *The Geology of North America*, A, 97– 138.

Xia, J., R. D. Miller, and C. B. Park, 1999, Estimation of near-surface shear-wave velocity by inversion of Rayleigh wave: *Geophysics*, 64, 691–700, doi: 10.1190/1.1444578.

Xie, B. X., S. Jin, and R. S. Wu, 2003, Three-dimensional illumination analysis using wave equation based propagator: 73<sup>rd</sup> Annual International Meeting, SEG, Expanded Abstracts, 989-992, doi: 10.1190/1.1818114.

Zuleta, L. M., D. C. Lawton, 2011, P – S survey design: 81<sup>st</sup> Annual International Meeting, SEG, Expanded Abstracts, 127-131, doi: 10.1190/1.3627437.